UNIVERSITÀ
DEGLI STUDI
FIRENZE

DOTTORATO DI RICERCA IN
SCIENZE CHIMICHE

CICLO XXVII

COORDINATORE Prof. ANDREA GOTI

ENGINEERING GOLD NANORODS FOR CANCER TREATMENT: BIOLOGICAL PROFILE, PROTEIN INTERACTIONS AND DRUG DELIVERY

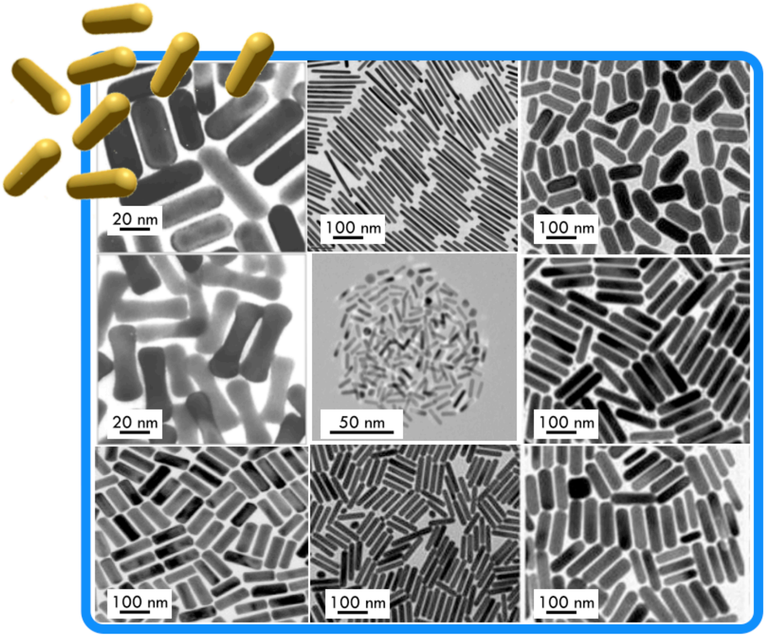

Dottorando
Dott. Federica Scaletti

Tutore
Prof. Luigi Messori

UNIVERSITÀ
DEGLI STUDI
FIRENZE

DOTTORATO DI RICERCA IN SCIENZE CHIMICHE

CICLO XXVII

COORDINATORE Prof. ANDREA GOTI

ENGINEERING GOLD NANORODS FOR CANCER TREATMENT: BIOLOGICAL PROFILE, PROTEIN INTERACTIONS AND DRUG DELIVERY

Settore Scientifico Disciplinare CHIM/03

Dottorando
Dott. Federica Scaletti

Tutore
Prof. Luigi Messori

Coordinatore
Prof. Andrea Goti

Anni 2012/2015

The most exciting phrase to hear in Science, the one that heralds new discoveries, is not "Eureka!" but "That's funny ..."

— Isaac Asimov

Table of contents

Preface

Engineering Gold Nanorods for Cancer Treatment: Biological Profile, Protein Interactions and Drug Delivery

Preface – Engineering Gold Nanorods for Cancer Treatment: Biological Profile, Protein Interactions and Drug Delivery

Rod-shaped gold nanoparticles, namely gold nanorods (GNRs) have recently attracted a widespread attention due to their unique optical properties and facile synthesis. In fact, GNRs exhibit two distinct localized surface plasmon resonances (SPRs): the transversal mode in the visible region (TSPR) and the longitudinal one in the upper visible or near-infrared part of the spectrum (LSPR) that correspond to the oscillations perpendicular or parallel to the rod length direction, respectively. In particular, the LSPR can be tailored to a particular wavelength: there is a linear relationship between the absorption maximum of the LSPR band and the mean aspect ratio (AR, ratio between the length and the width of the rod) of GNRs, which can be tuned during the synthesis. Other factors of impact on the frequencies of both TSPR and LSPR bands are the refractive index of the environment and the degree of particle aggregation. In addition, the surface of GNRs can be functionalized with a variety of molecules, providing stability and biocompatibility. All these features make GNRs ideal platforms for several applications and, in particular, for biomedical applications such as sensing, photo-acoustic imaging, photothermal treatment of cancer and drug delivery.

However, several problems are connected to the synthesis and purification of GNRs, as well as to their use for biomedical applications. All these issues are addressed within the present PhD thesis, with special attention for GNRs which are well suitable for protein sensing, the photothermal treatment of cancer, and the realization of nanocapsules as drug delivery systems.

Specifically, in the **Introduction**, a brief history of gold nanoparticles and gold nanorods, together with the synthetic procedure with an insight into the growth mechanism of GNRs, their optical properties and their biomedical applications, are addressed.

In **Chapter 1** the issues connected to the most common synthesis of GNRs (e.g. the difficulty to obtain relatively small GNRs and the precise control of the LSPR) are illustrated. Therefore a simple and reproducible method for the synthesis of small-sized GNRs with a good control over the LSPR is reported.

A modified method for the purification of small GNRs from reaction by-products (i.e. spherical and cubic nanoparticles or aggregates) is accurately described in **Chapter 2** with particular attention to the quantification of the separation.

Chapter 3 is focused on the realization and characterization of functionalized GNRs for therapeutic applications. Although the available literature is inconclusive, particle size may modulate critical parameters such as: the cellular penetration, the intracellular localization, the biodistribution, features that depend on specific surface area, including the rate of interaction with proteins, residual toxicity of contaminants, the ratio between absorption and scattering of the particles and the efficiency and stability of photothermal conversion. Specifically, this chapter offers an extensive survey on the size-related biological effects of functionalized GNRs (i.e. PEGylated GNRs), with special attention for the cytotoxicity and cellular uptake of GNRs on a panel of cellular models.

In **Chapter 4**, the possibility to tune the interactions between GNRs with proteins is illustrated by direct monitoring the LSPR of GNRs, which is highly sensitive to changes in the refractive index. In particular, the effect of the insertion of charged groups in PEGylated GNRs on their protein interactions is reported, providing useful hints for protein sensing applications.

Finally, in **Chapter 5** is focused on the generation of nanosized capsules through self assembling of GNRs to be used for the delivery of hydrophobic anticancer drugs. These GNR-stabilized nanocapsules could provide highly localized release of anticancer therapeutics, maximizing the therapeutic efficacy and minimizing off-target effects. These studies could provide the basis for future pre-clinical animal studies that could lead to an important new therapeutic strategy for tumors.

Introduction

Gold Nanoparticles: from Spherical to Rod-Shaped Gold Nanoparticles

Gold Nanoparticles: from Spherical to Rod-Shaped Gold Nanoparticles

"The fascination with gold is a story which spans millennia and this metal has played a role in almost every human existence. It has been a way of expressing wealth, it has been the cause of battles and wars, it has been related to religious devotion, and has been linked with our most intimate feelings as a way of expressing love."[1]

1. Gold Nanoparticles from the Past to the Nanotechnology Era

Although nanogold represents one of the most remarkable areas of modern nanoscience and nanotechnology, spherical gold nanoparticles (GNPs) have been known for millenia. The history of GNPs begins in remote times with red ruby glass and reach a peak at the end of the seventeenth century.

The Lycurgus cup

The first milestone in the history of gold ruby glass is a Roman opaque glass cup dated to the fourth century, the Lycurgus cup, which is exhibited at the British Museum in London (Figure 1). This cup shows a green jade color due to the diffusion of light when it is illuminated from outside and a deep ruby red one in transmission when it is illuminated from inside.

Figure 1. The Lycurgus cup illuminated from outside (left), illuminated from inside (right).

A detailed analysis of the Lycurgus cup revealed the presence of a small amount of gold and silver in the glass. [1] In fact, further analysis by Barber and Freestone in 1980, attested the presence of silver-gold alloy of 50-100nm size. [2] Thereafter, Hornyak et al. confirmed through a theoretical study that deep red color of the Lycurgus cup due to light absorption around 515 nm was consistent with the presence of silver-gold alloy particles. [3] However, since there is no evidence that Roman were able to produce *aqua regia* to prepare gold chloride at that period, the hypothesis that the Roman glassmakers may have used silver slags without knowing that they also contained gold, thus without knowing that gold was the actual colorant of glass, has been proposed. [4]

From the Medieval period to the nineteenth century

The alchemist of the Middle Ages knew how to produce red-colored glass with gold, although samples of such glass have yet to be found. [5] The treatise “Secrets of Secrets” [6] of a Persian scholar philosopher and alchemist, Al Razi, reports the earliest known written account of a gold ruby glass with the instructions for its preparation by heating a very finely powder batch of different elements including gold powder, in a closed furnace. However, the philosopher thought he had fulfilled the objective of transmutation of “impure” base metals into gold.

In the fifteenth century, technical informations on gold coloration were discussed in “Trattato di Architettura” by Antonio Averlino, also called Filarete, who wrotes “It is also said that gold makes colour”.[7] However, according to most of the textbook, the production of the red ruby glass did not take place until the end of the seventeenth century. The discovery is attributed to Andreas Cassius of Leyden (1685), who produced the so-called *Purple of Cassius*, which is a precipitate obtained from the dissolution of gold metal in *aqua regia* followed by the precipitation of the metallic gold by a mixture of stannous and stannic chloride.[8] Alchemists strongly believed that the color of metals indicated their essence and that if the color could be extracted it could perform alchemical transmutation. Great scientist such as Rober Boyle (1627-1691) and Isaac Newton (1642-1727) firmly believed in this principle.

Johann Kunckel was the first important maker of gold ruby glass in a large scale. Thereafter, the art of making gold ruby glass was lost on Kunckel’s death, as illustrated in the movie “Hearth of Glass” (Werner Herzog, 1976), and rediscovered in the nineteenth century when the interest for glass artefacts swept across Europe and United States.

Several English companies exhibited pieces of ruby glass in a variety of less saturated colors, close to pale pink, that were obtained by decreasing the gold concentration in glass. In the US, gold was also used to produce new types of glass, burmese and rose amber glasses, obtained from uranium oxide and gold.[1]

Scientific elucidation of the gold red ruby color

In nineteenth century, J. C. Fischer of Munich was able to draw up lists of six distinguished chemists who held that the gold was in metallic form against twelve who believed that it was present as an oxide. [9] As an example, in 1857 Michael Faraday delivered his Bakerian Lecture to the Royal Society, 'Experimental Relations of Gold (and other Metals) to Light', and said that:

"I believe the Purple of Cassius to be essentially finely divided gold associated with more or less of oxide of tin." [10]

However, the closest to the truth was Henri Debray, lecturer on chemistry at the Ecole Polytechnique, who suggested in a paper to the Académie des Sciences that *Purple of Cassius* consisted of finely divided gold that had been absorbed by stannic acid. [11] Not until the turn of the century was the true nature of *Purple of Cassius* elucidated. Richard Zsigmondy, a Viennese chemist who had spent some years studying gold colors at the Schott Glassworks in Jena, in 1905 published his researches on colloidal golds.[12] Thanks to the development of a slit ultramicroscope, based on light scattering, he was able to observe finely divided gold particles on colloidal stannic acid, and confirmed the presence of colloidal particles in the ruby glass. For these investigation he was awarded of the Nobel Prize in Chemistry in 1925. [12]

In 1908 Gustav Mie predicted the optical properties of homogeneous spherical particles [13]: for a spherical nanoparticle much smaller than the wavelength of light, an electromagnetic field at a certain frequency induces a resonant, coherent oscillation of the metal free electrons across the nanoparticle. This oscillation is known as the localized surface plasmon resonance. [14-15] The plasmon oscillation of the free electrons of the metal particles Au, Ag and Cu, results in a strong enhancement of absorption and scattering of electromagnetic radiation in the visible range (i. e. around 520 nm for gold) in resonance with the plasmon frequency, giving them intense colors and interesting optical properties, with the ratio between scattering and absorption related to the particle volume. This is more intensively discussed in the next section of the present chapter.

Therefore, the dichroism of the Lycurgus cup, can be explained as follows. When the cup is illuminated from outside, the green color is due to the non-negligible contribution of the scattering of the 50-100 nm nanoparticles contained in the cup, while the red color when the cup is illuminated from inside results form the absorption contribution.

In Carbert's paper [16] the chemical approach to the formation of the *Purple of Cassius* is reported. Two distinct stages are involved, first the formation of a gold sol and then its stabilization. The first stage is a redox reaction in which the addition of a stannous chloride solution to an auric chloride solution results in the formation of metallic gold:

$$2Au^{3+} + 3Sn^{2+} \rightarrow 2Au^{0} + 3Sn^{4+}$$

It is most important that particle growth should be controlled during this reaction, which proceeds very rapidly. Transmission electron microscopy of enamels colored by good quality *Purple of Cassius* indicates that the gold particle's optimum size was 10-15 nm (Figure 2).

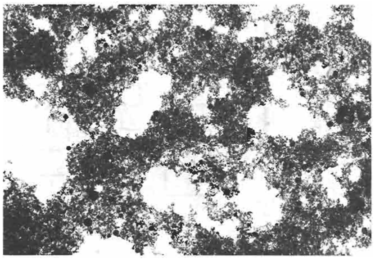

Figure 2. Examination of *Purple of Cassius* by transmission electron microscopy shows the black particles of finely dispersed gold on the surface of colloidal stannic acid. (Magnification: x 100000).

However a large number of factor can cause variations in the particle's size and therefore in the hue and strength of the color.

A simplified scheme of the principle of gold ruby glass formation is reported by Weyl.[17] The preparation of gold ruby glass consists of three steps: 1) the addition of gold (hundreds of ppm) as gold chloride or as *Purple of Cassius*, in melt glass; 2) a step of rapid quenching to room temperature; 3) a step of annealing at 500-650°C, during which red color appears. Specifically, during the cooling step, there is oversaturation of the "atomic" gold solution and the formation of gold nuclei. At this point, two distinct cases can be distinguished depending on the composition of the glass: 1) glass such as sodium silicate or borax glass lead to the growth of the nuclei and the formation of large gold nanoparticles (100 nm) and a brownish color; 2) the presence of tin or bismuth ions in glass enhances gold solubility, and when nuclei are produced, a substantial amount of gold still remains in atomic dispersion. Then, reheating causes the nuclei to grow and nanoparticles with size 5-50 nm are formed, giving rise to the red color.

Gold nanoparticles today

The history of GNPs, that has paralleled that of gold ruby glass for centuries, is now expanding with the advent of Nanosciences and Nanotechnologies.

The "golden timeline" (Figure 3) summarizes the most relevant recent advances in chemistry, physics and microscopy, which have led to better control of GNPs size and shape distribution and a deeper understanding of how GNPs interact with light, other than more details on their atomic structure.

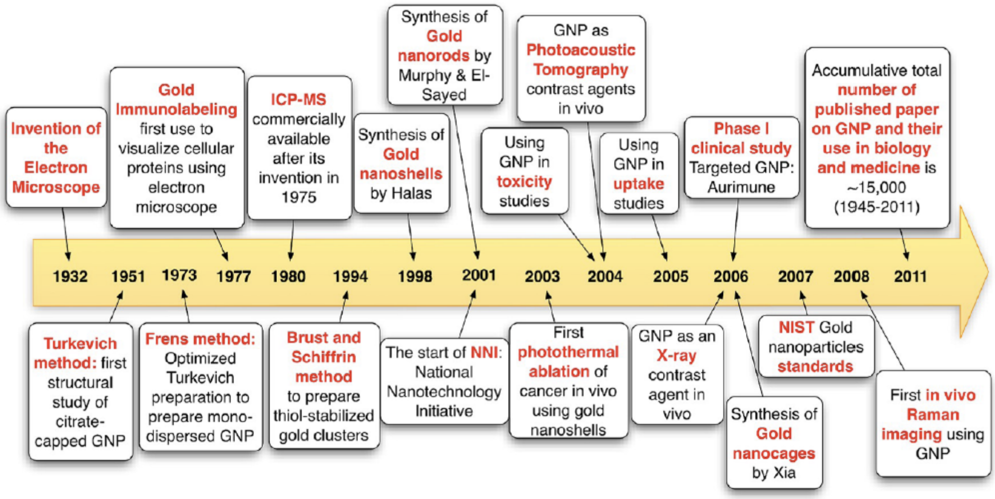

Figure 3. The golden timeline: major events and discoveries from the invention of the electron microscope until recent days. [18]

Nowadays researches on synthesis and the discovery of anisotropic GNPs, as well as on their properties and applications, involve many fields in chemistry, biology and physics.

More details on these topics will be discussed in the next sections, with a special consideration for rod-shaped gold nanoparticles, namely gold nanorods (GNRs), their unique optical properties, their preparation and their biomedical applications.

2. Optical properties of spherical and rod-shaped gold nanoparticles

Among the remarkable properties of GNPs, the collective behavior of their conduction electrons that give rise to the plasmon resonance is a dramatic one. The intriguing optical properties of GNPs, as reflected by their intense color, are attributed to their unique interaction with incident light. In fact, in the presence of the oscillating electromagnetic field of light, the conduction band electrons of a GNP undergo a collective coherent oscillation in resonance with the frequency of light, which is called Localized Surface Plasmon Resonance (localized SPR). [13,19-21] The oscillation induces a charge separation between free electrons and the ionic metal core, creating a field inside the GNPs, the so-called restoring field, but also out of the nanoparticles. Due to the large charge accumulation at the surface of GNP, intense fields are generated in a region larger than the nanoparticle size.

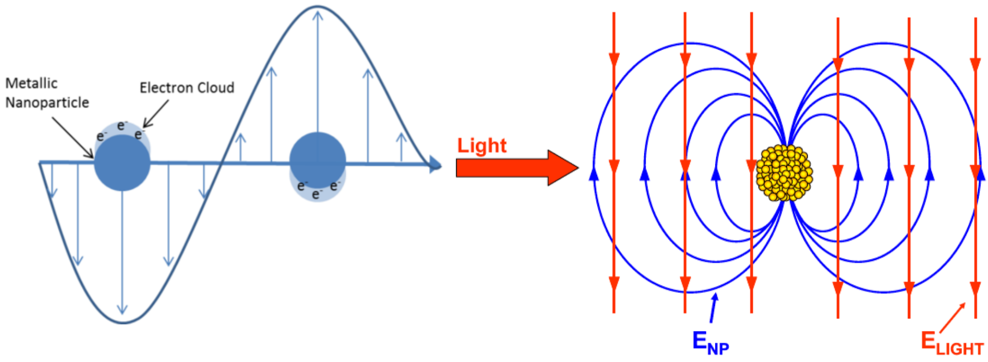

Figure 4. Illustration of the electric field of the light inducing the movement of conduction electrons which accumulate at the GNP surface (left) and the electric fields of incident light and that created by the electron oscillations near the GNP (right). [22]

As illustrated in Figure 4, there are wide regions where the electric field created by the nanoparticle is opposite to that of the light, so the interference is destructive, leading to light absorption beyond the NP volume [23], as seen in the UV-vis spectrum, which is the origin for the observed color of GNPs (Figure 5).

For other regions, the result of the interference between both electric fields is a net field with a different propagating direction, hence inducing light scattering. Therefore, the interaction of light with matter containing GNPs invariably involves scattering and absorption, both of which cause attenuation in the intensity of beam passing through the medium. [22]

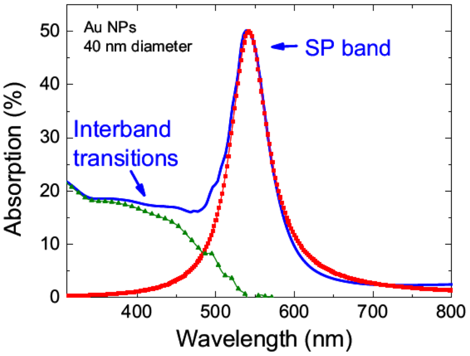

Figure 5. Extinction spectrum of GNPs with 40 nm size. For GNPs, the contribution to the extinction of interband transitions and localized SPR are resolved. [22]

Moreover, the localized SPR condition is dependent on the particle size, shape, structure, dielectric properties of the surrounding medium, and the plasmon coupling between particles, as these factors affect the electron charge density on the particle surface. [13,19-21,24-26]

Effect of the shape: GNRs

While spherical GNPs show a strong localized SPR band in the visible region, anisotropic GNPs, also exhibit a red-shifted localized SPR band compared to their spherical analogs. [27-28] The most clear example of these shape effects are the GNRs (Figure 6). [29-30]

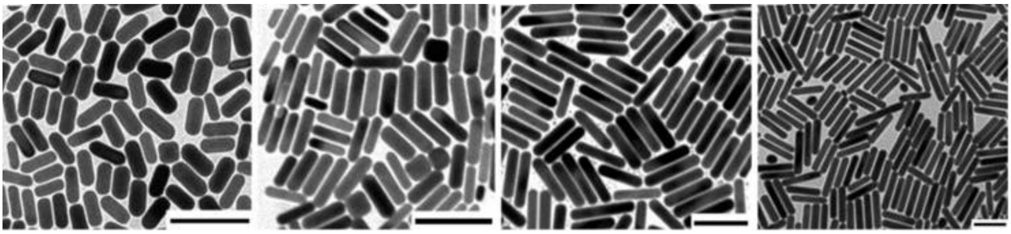

Figure 6. Transmission electron microscopy (TEM) images of different GNRs. Scale bars: 100nm. [31]

Gold nanorods with cylindrical symmetry usually exhibit two plasmon modes, a longitudinal (localized) SPR (LSPR) mode associated with the electron oscillations along the length direction and a transverse (localized) SPR (TSPR) mode arising from the transverse electron oscillations. Due to the longer path of the electron movements, the longitudinal mode is located at the red side of the transverse one (Figure 7). In fact, the charge accumulation will be the maximum for the transversal plasmons and the minimum for electron displacement along the rod axis. The restoring force is proportional to this charge accumulation, therefore, for electron oscillating along the rod axis, smaller forces and, consequently smaller resonance frequencies (i.e. larger resonant wavelengths) should be expected.

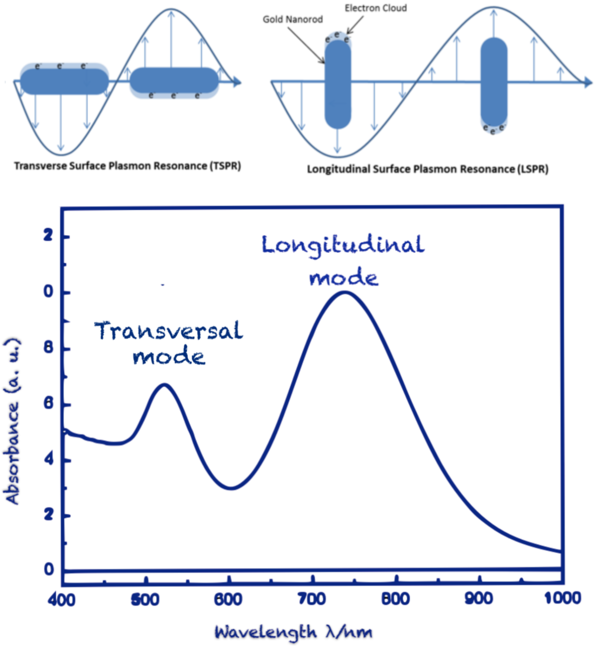

Figure 7. Illustration of the electric field of the light inducing the movement of transverse and longitudinal conduction electrons which accumulate at the GNR surface (left) and a representative extinction spectrum of GNRs (right). [31]

Therefore, for GNRs, the resonant frequency of the TSPR falls about the same position as for spherical GNPs while the resonance of LSPR shifts toward larger wavelengths when the nanorod aspect ratio (AR), the ratio between the length (l) and the width (w) of the rod, increases (Figure 8).

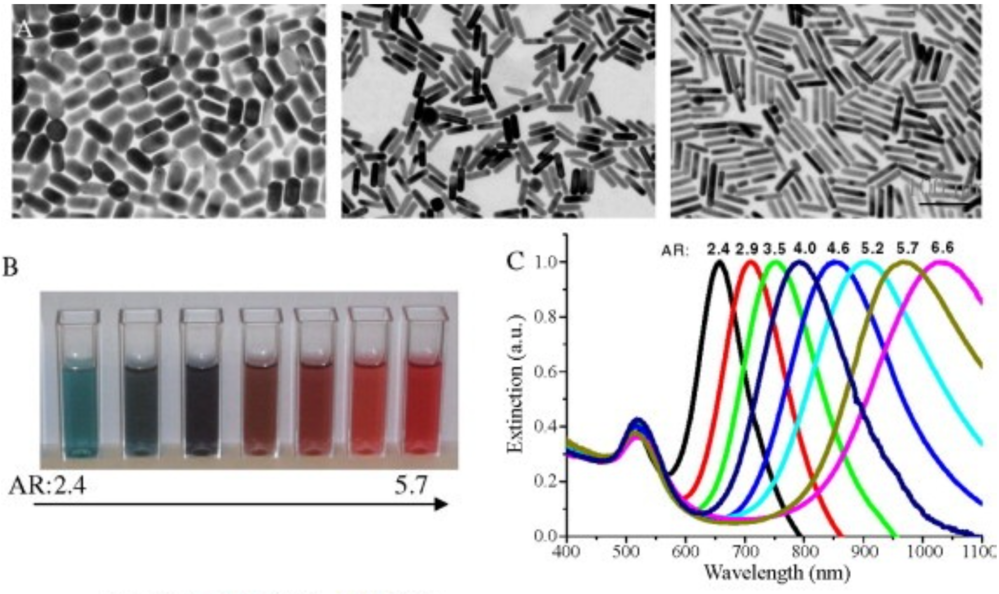

Figure 8. Tunable optical properties of GNRs by changing the ARs. Gold nanorods of different ARs exhibit different dimensions as seen by TEM (A), in different color (B) and different SPR wavelengths (C). [32]

This optical behavior can be well understood according to Gans theory [33] which was developed for the explanation of optical properties of ellipsoid particles based on the dipole approximation. In aqueous solution, the SPR absorption maximum (λ_{max}) is linearly proportional to the AR of the rod by the following relationship:

$$\lambda_{max} = (95AR+420)\ \text{nm}$$ [34-37]

This provides the possibility of optical tuning GNRs by simply varying the AR of the rod, which is different from spheres for which the SPR only slightly red-shifts with increasing particle size. [22] The AR of GNRs can be easily tuned by varying the ratio between reagents used for the synthesis; a more detailed explanation is reported in the next section.

Gans theory also enables the determination of the statistical distribution of ARs of a GNRs solution with a convolution of homogeneously broadened spectra of GNRs, each with a specific AR and population contributions. [38] Such a method provides a relative convenient alternative to conventional TEM.

Effect of the surrounding medium

As mentioned above, the SPR and, in particular, the LSPR of GNRs, is also significantly dependent on the surrounding medium because the dielectric function of the surrounding medium (ε_m) determines the light wavelength at the vicinity of the GNR, altering the geometry of the electric field at the surface of the particle. However, the most important effect is related to the polarization of the medium. In fact, during the SPR excitation, the charge accumulation creates an electric field in the vicinity of the GNRs, in addition to that of the incident light. This field induces the polarization of the dielectric medium, resulting in a charge accumulation at the interface between the dielectric and the GNRs) that will partially compensate the charge accumulation due to the movement of conduction electrons in the GNR. This reduction of charge will depend on the ε_m; the larger ε_m, the larger the polarization charge, and hence, the larger the effect on the SP. Reducing the net charge at the NP surface implies a reduction in the restoring force. For an oscillator, it is well known that reducing the restoring force leads to smaller resonant frequency. [22] Thus, increasing the dielectric constant of the surrounding media will shift the SPR band towards larger wavelengths (Figure 9), according to the following equation:

$$\lambda_{max} = (33.34\ \varepsilon_m \mathrm{AR} - 46.31\ \varepsilon_m + 472.31)\ \mathrm{nm} \quad [34]$$

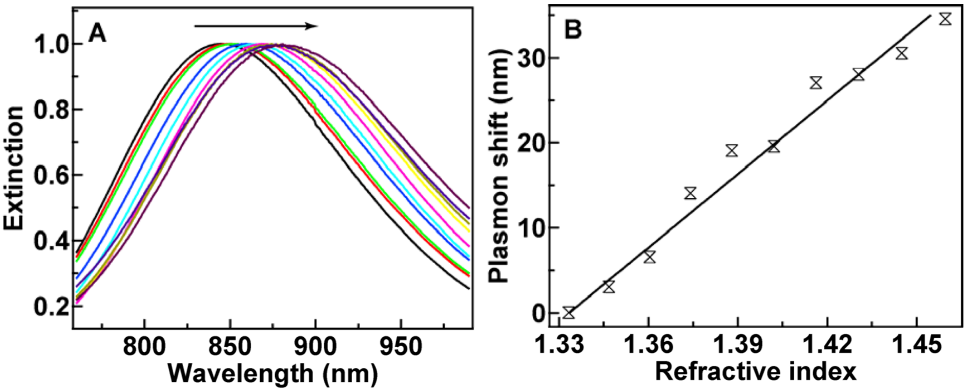

Figure 9. Example of the effect of the medium on the LSPR of GNRs. [39] (A) Normalized extinction spectra of GNR with an aspect ratio of 4.6 in water-glycerol mixtures of varying compositions. The arrow indicates the direction of increasing volume percentage of glycerol in the liquid mixture. (B) Dependence of the longitudinal plasmon shift on the refractive index of the liquid mixture.

Effect of the plasmon coupling

GNRs display unique and strongly enhanced optical properties due to the TSPR and LSPR. When two GNRs are placed in a close proximity to, but not in contact with each other, the plasmon resonances carried by the two nanorods will interact (i.e. near-field interaction) to form different collective plasmon modes (coupled plasmon resonance modes), according to the plasmon hybridization model. [40]

Due to the geometrical anisotropy and the synthetically tailorable longitudinal plasmon energy of GNRs, coupled GNRs exhibit extremely rich spectral responses. The plasmon coupling of GNRs also provides much larger electric field enhancements than individual GNRs. These unique properties brought by coupled plasmonic GNRs offer great potential in a variety of applications, such as highly sensitive biological and chemical sensors [41], optical switches [42], plasmon enhanced spectroscopies (e.g Surface-Enhanced Raman Spectroscopy, SERS) [43], and metamaterials for manipulating light at the nanoscale.[44]

Both theoretical and experimental results have revealed that the plasmonic interactions between two GNRs depend strongly on their relative configurations.[45-48] Under the excitation of light polarized along the length axis of GNRs, linearly, end-to-end assembled GNRs homodimers have been experimentally found to support a largely red-shifted coupled plasmon mode (Figure 10), while side-by-side assembled homodimers support a slightly blue-shifted coupled plasmon mode (Figure 11).[49]

Moreover, as illustrated in Figure 10 and 11, there is a relationship between the internanorod distance and the plasmon coupling. A universal scaling behavior of the distance-dependent decay of the plasmon coupling, which is expressed by the fractional wavelength shift after coupling, is applicable for GNR homodimers aligned along the length axis when the gap distance is not very small. The universal scaling behavior can be described by the following equation:

$$\frac{\Delta\lambda}{\lambda} \approx Ae^{-(s/D)^{1/3}/\tau}$$

where, l is the plasmon wavelength of the uncoupled GNR, Δλ is the plasmon wavelength shift caused by the plasmon coupling, s is the gap distance, D is the length of GNR, t is the decay constant, and A is the maximal fractional plasmon wavelength shift. [50]

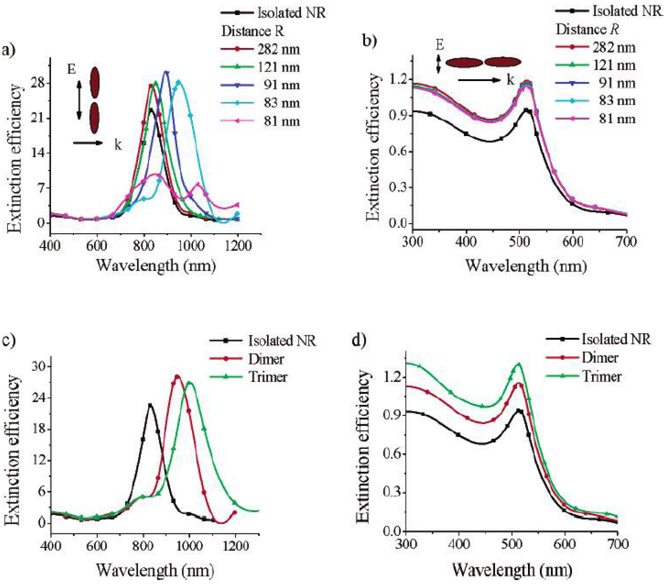

Figure 10. DDA-simulated extinction efficiency spectra of GNR (80x20 nm) assembled in an end-to-end orientation: (a)LSPR excitation and (b) TSPR excitation of a pair of nanorods as a function of the internanorod center-to-center distance (R= 282, 121, 91, 83 nm and 81 nm where GNRs touch each other). (c) LSPR excitation and (d) TSPR of a nanorod assembly as a function of the number of GNRs with R fixed at 83 nm.[45]

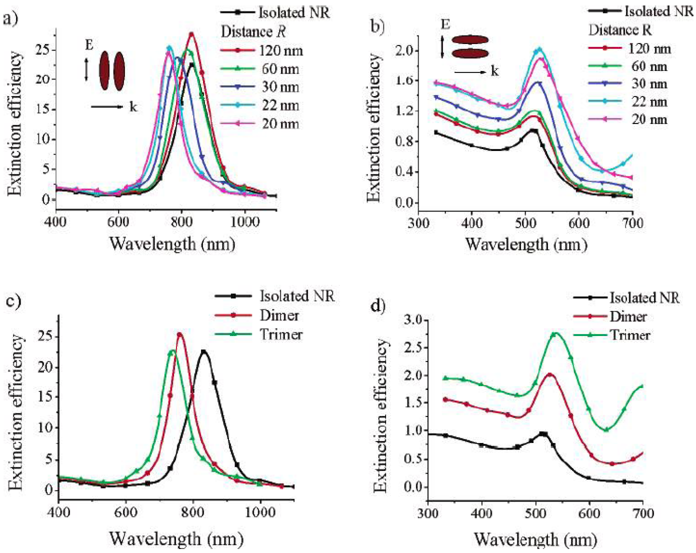

Figure 11. DDA-simulated extinction efficiency spectra of GNRs (80x20 nm) assembled in a side-by-side orientation: (a) LSPR excitation and (b) TSPR excitation of a pair of GNRs as a function of R=120, 60, 30, 22 nm and 20 nm where GNRs touch each other. (c) LSPR excitation and (d) TSPR of a nanorod assembly as a function of the number of GNRs with R fixed at 22 nm.[45]

3. Synthesis and mechanism of GNRs formation

Shape-controlled synthesis has received widespread interest due to the importance of anisotropic GNPs in their structural, optical, electronic and catalytic properties, as well as their potential applications (a more detailed description on the applications is given in section 5). Although the modern synthesis of spherical GNPs is dated back to 1857 by Faraday [51] fabrication of colloidal GNRs emerged only in 2000s [52] and great advancement has been achieved for obtaining GNRs with high yield, quality, and uniformity. [53,54]

The most common synthesis of GNRs involves nucleation and growth steps (i.e. seed-mediated growth method). Modern concepts of seed-mediated synthesis were established by the Murphy research group in 2001. [51] They reported the synthesis of GNRs by the addition of citrate-capped GNPs to an Au(I) growth solution generated by the reduction of Au(III) (i.e. tetrachloro auric acid, $HAuCl_4$) with ascorbic acid (AA) in the presence of hexadecyltrimethylammonium bromide, also called cetyltrimethylammonium bromide (CTAB) and Ag(I) (from silver nitrate, $AgNO_3$) . The seeded-growth method has become established as the most efficient and popular one to synthesize specific shapes in high yields.[52,53] In 2003, Nikoobakht and E-Sayed [53] made two modifications to this method: replacing sodium citrate with a stronger stabilizer (i.e. CTAB) in the seed formation process and utilizing silver ions to control the AR of GNRs. This protocol includes two steps (Figure 12): 1) synthesis of seed solution by the reduction of $HAuCl_4$ in the presence of CTAB with ice-cold sodium borohydride ($NaBH_4$) and 2) the addition of the seed solution to the Au^+ stock solution in the presence of CTAB and $AgNO_3$ which is obtained by reduction of $HAuCl_4$ with AA. $AgNO_3$ is introduced to the gold solution before seed addition to facilitate the rod formation and to tune the AR as well. This method produces high yield GNRs (>95%) with AR ranging from 1.5 to 5.

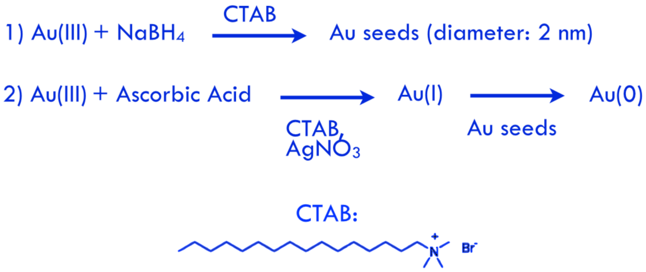

Figure 12. Scheme of the seed-mediated synthesis by Nikoobakht and E-Sayed [53] and chemical structure of CTAB.

One of the key points in the seeded growth method is the use of a weak reducing agent, such as AA, so that gold reduction takes place only on existing nuclei in solution, which also act as catalysts. Upon addition of AA to a growth solution containing a mixture of $HAuCl_4$ and CTAB, the reduction of Au(III) to Au(I) takes place, indicated by the solution turning colorless (the ligand-to-metal charge-transfer band disappears for a d^{10} metal center as Au(I)). It is crucial that the reducing agent cannot complete the reduction of Au(I) into Au(0), that is, secondary nucleation during the growth step is prevented. In fact, the seeds act as catalysts for the final reduction step, thereby inducing reduction of the Au(I) precursor on their surface only. The proposed mechanism consists in an *in situ* reduction of Au(I) catalyzed by the Au(0) surface of seeds, which drains electrons from the reductant. [55] It should be noted that AA features a pH-dependent reduction potential, being lower under acidic conditions and higher at more basic pH values, [56] which has been applied to modulate Au nanorod growth. In fact, if the pH is above 9, ascorbic acid will be able to reduce Au(I) into Au(0), even in the absence of seeds, thus compromising the seeded growth mechanism.

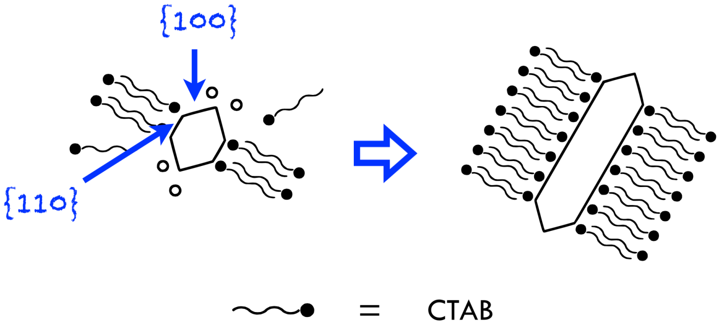

Figure 13. Schematic representation of crystallographic faces of gold seeds and the CTAB bilayer on GNRs surface during the growth mechanism.

The proposed mechanism to explain the growth process of GNRs consists in a surfactant-preferential-binding-direct growth (Figure 13) [57], in which CTAB adsorbs onto GNRs in a bilayer fashion, with the CTA^+ headgroups of the first monolayed facing the gold surface, and preferentially binds to the {110} crystallographic faces of gold existing along the sides of GNR, as compared to the {100} faces at the tips. Consequently, the crystal growth on the side of GNRs is retarded and gold is deposited to the end facet leading to rod growth. [57-58]

Moreover, the effect of $AgNO_3$ is crucial for GNRs growth. In fact, the role of silver ions in controlling the AR can be explained as adsorption of the Ag-Br pair to the different facets of GNRs which restricts particle growth. [52] Ag-Br pairs decrease the charge density of bromide ions and thus decrease the repulsion of neighbouring CTA^+ headgroups. [53] Liu and Guyot-Sionnest [58] have systematically studied the effect of silver ions on CTAB-capped seeds, showing that these seed lead to single crystalline GNRs with {110} faces on the side and {100} faces at the flat end. The deposition of gold atoms on the seed surface does not create a stacking default and, therefore, preserves the initial seed structures. Although Ag(I) in the CTAB solution cannot be reduced to bulk silver atoms by AA in acidic pH [59], it can be reduced to Ag(0) onto a gold substrate in the form of a metal monolayer at a potential lower than that one required for a bulk reduction, known as underpotential deposition (UPD). [60] The reduction potential for silver deposition on {110} gold faces is lower than that on {100}. [60] Therefore the silver deposition on the {110} side of the rod is faster than on the {100} ends due to the UPD effects and thus the seeds grow into nanorods. In fact, an increase in silver ions results in an increase of the AR (Figure 14) [61]. However, an increase in silver ions over a threshold concentration could not further increase the AR due to the blocking of the end facet on the nanorods by silver metal deposition. [53]

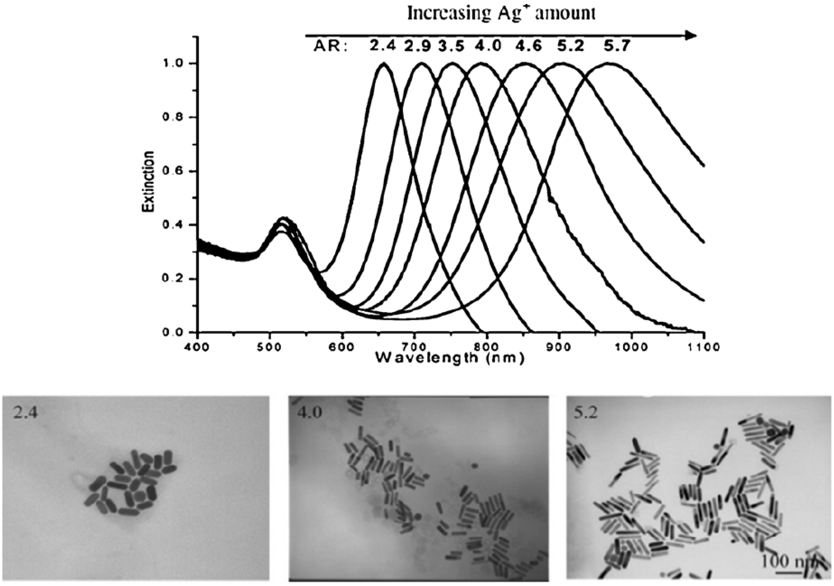

Figure 14. Increasing the amount of silver ions leads to GNRs of higher aspect ratios, which is consistent with the red-shifting LSPR. For GNRs with AR over than 5, the use of binary surfactant is required. [61]

The synthesis of Au nanorods relies on the ratios between all reagents involved. For this reason, the allowed range for each component is quite narrow and multiple parameters must be take into account [62], as briefly summarized below:

– [Ag(0)]: A higher concentration increases the aspect ratio. [63]
– [ascorbic acid]: A higher concentration decreases the aspect ratio. [63]
– [seed]: A lower amount of seeds results in the production of larger nanorods, in general with a smaller AR. [64]
– [pH]: Lower pH values slow down the growth kinetics, leading to higher ARs. [65]

4. Functionalization of GNRs

The production of GNRs requires the use of CTAB, which acts as a stabilizing agent for GNRs [66] and is evidently present after synthesis, both in the supernatant and on the surface of GNRs. In fact, the capping CTAB molecules form a partially-interdigitated bilayer on the surface of GNRs, similar to the structure of a vesicle (Figure 16). The gold surface is believed to carry negative charges due to the adsorption of bromide ions. The positively charged ammonium headgroup of CTA^+ binds tightly to the gold surface through electrostatic interaction, leading to the formation of the inner layer. Since the hydrophobic carbon-chain does not like to stay in water, another layer of CTAB molecules is formed, with the hydrophobic tails pointing inside and interacting with dose of the inner layer and the ammonium groups pointing outside. [67] The CTAB bilayer makes GNRs positively charged and therefore stabilized in aqueous solutions. However the bilayer can be disrupted when the CTAB concentration is lower than its critical micelle concentration (cmc= 1 mM at 25°C) [68], organic solvents (able to dissolve CTAB) are added, the salt concentration in the solution is high, or some external stimuli are applied to the GNRs solution. [50] Moreover, CTAB is a cationic surfactant that is also known to be a detergent suitable for the degradation of biomembranes and peptides. Therefore, free CTAB is certainly cytotoxic to human cell. (Figure 15). [69]

In order to make GNR biocompatible and stable under different conditions and arm them with added functionalities for particular applications, CTAB-capped GNRs should be functionalized with appropriate organic or inorganic species. [70] Different methods have been developed for functionalizing CTAB-capped GNRs end almost completely remove CTAB from GNR surface.

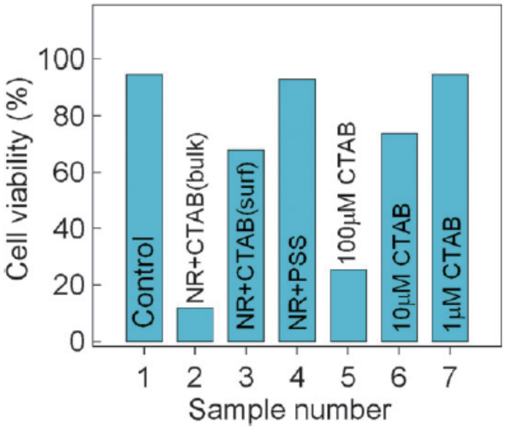

Figure 15. Viability of cells incubated with CTAB-capped GNRs and PSS-coated GNRs, compared to free CTAB at different concentrations. [69]

Gold-thiol bonding chemistry is commonly used for completely or partially functionalizing the surface of GNRs. Small molecules are not preferred because the steric effect introduced by small molecules cannot overcome the large attractive force among GNRs. Therefore, the bonding of small thiol molecules often leads to poor dispersibility and irreversible aggregation of GNRs. Thiol-terminated polymers with high molecular weight, such as (5000 MW)-polyethylene glycol (PEG) is perceived as the coating of choice because of its biocompatibility, ability to avoid the detection from macrophages, readiness of biochemical modification, such as with antibodies, and steric hindrance against particle aggregation. [71-73]

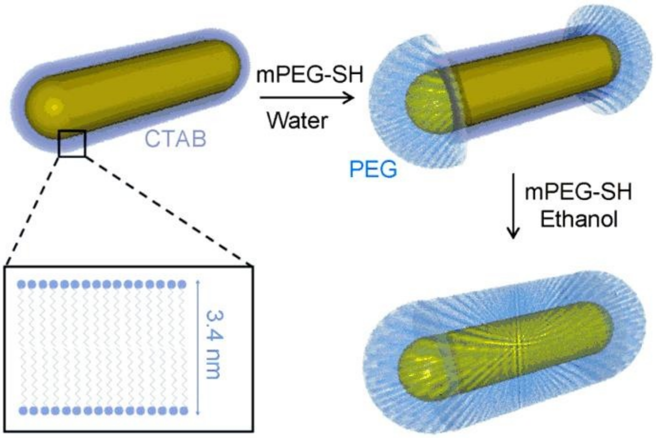

Figure 16. Illustration of the CTAB bilayer on GNRs surface and the two-step procedure for the complete detoxification of GNRs from CTAB. [68]

Moreover, thiol molecules have been found to preferentially bind to the two ends of GNRs at low concentrations, which has been attributed to the smaller packing density of CTAB at the highly curved ends. [74-75] Kinnear et al. [68] reported a protocol for the complete detoxification of GNRs from CTAB with a two-step procedure, achieved with a primary functionalization with thiol-PEG in water, during which PEG is preferentially bound to the two ends of the rod, and, thereafter, a second functionalization step in ethanol, in which CTAB is highly soluble (Figure 16).

Other coatings have been proposed as an alternative to PEG, such as other polymers [69], hydrophobic thiol-molecules [76] or coating with silica. [77] However PEG remains the most common choice of functionalization.

5. Biomedical applications of GNRs

As mentioned above, GNRs provide exceptional optical properties, which make GNRs a new type of nanostructure suitable for a wide range of biological and biomedical applications including biosensing, biomedical imaging, gene and drug delivery, disease detection, diagnosis and therapy. In the next paragraphs an introduction to some of the most important applications of GNRs is given.

Photothermal treatment of cancer

The photothermal treatment of cancer that relies on the plasmonic photothermal conversion of GNRs, promotes the selective destruction of cancer cells without using any conjugated drugs by inducing local heating (up to 47°C) of targeted sites. [78] In this frame, GNRs exhibit an intense and tunable absorption in the near IR region (LSPR) of the spectrum (650-1000 nm), where light penetration in tissues is optimal due to minimal absorption by water and hemoglobin in the tissue. Therefore, GNRs are able to efficiently convert light (from laser irradiation) in localized heat. [79] In addition, the conjugation of targeting molecules, such as folate, or antibodies to GNRs may allow a pin-point targeting of heating. As an example, Huff et al. [80] and Tong et al. [81] have characterized the mechanisms of cell injury due to the photothermal effect of folate-conjugated GNRs (F-GNRs) on KB cells at the single-cell level, using a scanning laser microscope. KB cells with membrane-bound F-GNRs, showed the loss of membrane integrity after laser irradiation (Figure 17).

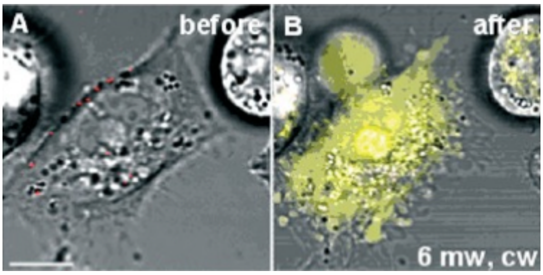

Figure 17. Site-dependent photothermolysis mediated by folate-coniugated GNRs(red). KB cells with membrane-bound F-NRs before (A) and after (B) laser irradiation. The loss of membrane integrity was indicated by ethidium bromide (EB) nuclear staining (yellow). [81]

Molecular imaging

Molecular imaging is defined as " a tecnique which directly or indirectly monitors and records the spatiotemporal distribution of molecular and cellularprocesses for biochemical, biologic, diagnostic, or therapeutic applications". [82] It visualize molecular or genetic phenomena in live cells, tissue, organs, and whole organisms. [83]

Plasmonic nanoparticles such as GNRs, are efficient contrast agents in optical imaging based on their unique light-particle interaction process (i.e. the excitation of localized SPR by light). This SPR enhances all linear and nonlinear optical properties and thus offers multiple imaging modalities including light scattering, [84] optical coherent tomography, [85] extinction, [86] photothermal, [87] two-photon luminescence, [88] multiphoton imaging, [89] and photoacoustic imaging. [90] Some examples of *in vitro* and *in vivo* imaging are illustrated in Figure 18 and 19.

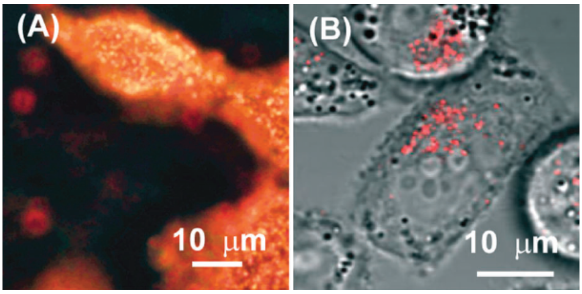

Figure 18. Dark-field scattering image of cancerous hematopoietic stem cells with anti-EGFR-conjugated GNRs located on cytoplasm membranes (A).[78] Two-photon-excited photoluminescence imaging of KB cancer cells with internalized folate-conjugated GNRs (B). [91]

Dark field microscopy is a particularly suitable method for imaging biological samples: although the extinction cross section of GNRs is dominated by absorption, the amount of scattering produced is more than sufficient for single-particle detection against a dark background. By using dark-field scattering imaging, antibody-labelled GNRs have been demonstrated for cancer diagnosis by their selective binding to cancer cells through recognition of the over-expressed EGFR on the cell surface (Figure 18A). [78] Moreover two-photon-excited photoluminescence of GNRs can well differentiate their targeting of cancer biomarkers on cytoplasm membranes (Figure 18B). [91]

Photoacoustic tomography (PAT) is a noninvasive imaging technique based on NIR-induced photoacoustic effects. [92] NIR-absorbing GNRs have recently been employed as contrast agents for PAT, which would otherwise rely on the intrinsic differences in optical absorption within tissue for contrast. PAT images of nude mice were significantly enhanced by the injection of GNRs, which could enhance differences in signal intensity with concentration gradients as low as pM concentrations (Figure 19). [93]

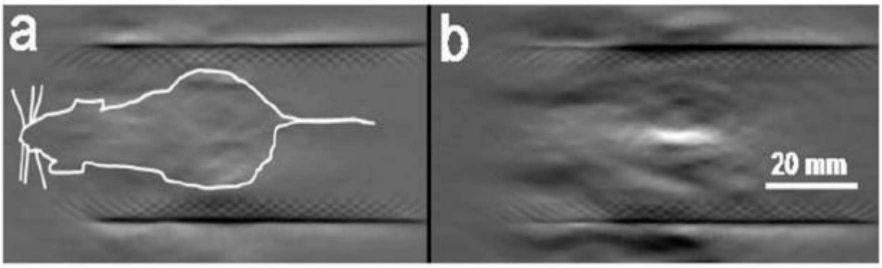

Figure 19. GNRs as contrast agents for photoacoustic tomography. PAT image of a nude mouse (white outline) before (A) and after (B) injection of GNRs. [93]

Biosensing

As described previously, the LSPR frequency of GNRs depends on the dielectric constant of the surrounding medium: an increase of this constant leads to a red-shift of the LSPR wavelength. Therefore, the LSPR wavelength, either by absorption or scattering, provides great opportunity to monitor the changes of the local environment of GNRs and thus can be used for sensing. [94] In particular the sensitivity, defined as the plasmon shift per refractive index unit change depends on the shape of the nanoparticles: anisotropic nanoparticles such as GNRs give higher sensitivity than spherical one. Several examples with antibody-conjugated GNRs have been reported.

Chilkoti et al. successfully detected the binding of streptavidin to an individual bioting-conjugated GNRs with a detection limit down to 1 nM, by measuring the plasmon shift of the LSPR of GNRs. [95] An alternative strategy for plasmonic sensing is to make use of the aggregation or assembly of GNRs. It is based on the spectral shift due to the plasmon coupling by bringing different GNRs close to each other. As an example GNRs have been utilized for environmental toxin sensing by employing their side-by-side and end-to-end assemblies. [96] In this study, GNRs were first functionalized with microcystin-LR antibodies and microcystin-LR-OVA antigens to induce the side-by-side or end-to-end assembly (Figure 20A). An increase of the toxin MC-LR concentration in the solution broke the conjugation between the MC-LR antibodies and antigens, leading to the disassembly of the nanorods. By monitoring the spectral change of the GNRs solution, the presence of the toxin as well as its concentration can be measured (Figure 20B). The sensitivity of the end-to-end assembly modality reaches up to 0.03 ng mL^{-1}.

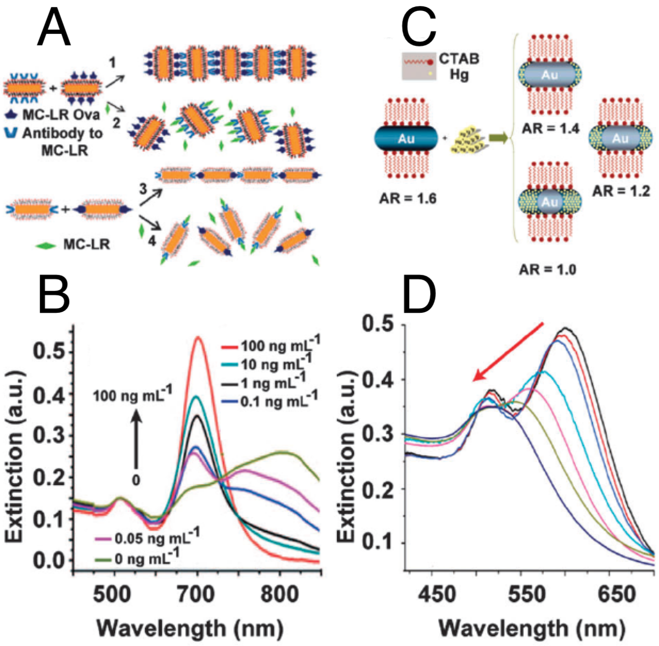

Figure 20. Schematic showing the toxin detection method with side-by-side and end-to end Au nanorod assemblies.[96] (F) Evolution of the extinction spectra of GNRs as the concentration of microcystin-LR (MC-LR) is increased for the end-to-end assemblies. [96] (G) Schematic showing the detection of Hg^{2+} with GNRs.[97] (H) Spectral evolution of GNRs as a function of the Hg^{2+} concentration. The red arrow indicates the spectral change with the increase in the Hg^{2+} concentration. [97]

The plasmonic sensing principle can also be extended for nonbiological species such as Hg^{2+} ions in tap water by taking advantage of the amalgamation of mercury with gold. [97] The adsorbed Hg^{2+} ions amalgamate with GNRs, leading to the reduction of the AR (Figure 20C). Therefore, the concentration of Hg^{2+} ions can be determined from the blue shift of the longitudinal plasmon resonance of the nanorods (Figure 16D).

References

[1] R. H. Brill, Proc. 7th Internat. Cong. Glass, Bruxelles, Section B Paper 223 (1965) 1.
[2] D. J. Barber, I. C. Freestone, Archaeometry 32 (1990) 33.
[3] G. L. Hornyak, C. J. Patrissi, E. B. Oberhouser, C. R. Martin, J. C. Valmalette, L. Lemaire, J. Dutta, H. Hofmann, NanoStruct. Mater. 9 (1997) 571.
[4] M. Verità, P. Santopadre, J. Glass Studies 52 (2010) 11.
[5] I. Freestone, N. Meeks, M. Sax and C. Higgitt, Gold Bull. 40 (2007) 270.
[6] H. A. Sheybany, Glastechnische Berichte 40 (1967) 481.
[7] P. Zecchin, J. Glass Studies 52 (2010) 25.
[8] L. B. Hunt, Gold Bull. 9 (1976) 134.
[9] J. C. Fischer, Dinglers Polytech. J. 182 (1866) 31.
[10] M. Faraday, Philos. Trans. R. Soc. 147 (1857) 17.
[11] A. J. Debray, C. R. Acad. Sri. 76 (1872) 1025.
[12] R. Zsigmondy, Annalen, 1898, 301, 361; Zur Kenntis der Kolloide', Jena, 1905; 'Colloids and the Ultramicroscope', translation Alexander, New York, 1909, 65; E. Farber, `Nobel Prize Winners in Chemistry', New York, 1953, 95.
[13] G. Mie, Ann. Phys. 25 (1908) 377.
[14] K. L. Kelly, E. Coronado, L. L. Zhao, G. C. Schatz, J. Phys. Chem. B 107 (2003) 668.
[15] P. K. Jain, I. H. El-Sayed, Nanotoday 2 (2007) 18.
[16] J. Carbert, Gold Bull. 40 (1980) 144.
[17] W. A. Weyl, The Society of Glass Technology (1951).
[18] A. M. Alkilany, S. E. Lohse, C. J. Murphy, Acc. Chem. Res. 46 (2013) 650.
[19] M. Kerker, Academic Press, New York 1969.
[20] G. C. Papavasiliou, Prog. Solid State Chem. 12 (1980) 185.
[21] C. F. Bohren, D. R. Huffman, Absorption and Scattering of Light by Small Particles, Wiley, New York (1983).
[22] M. A. Garcia, J. Phys D: App. Phys. 44 (2011) 283001.
[23] R. A. Dynich, A. N. Ponyavina, J. Appl. Spectrosc. 75 (2008) 832.
[24] S. Link, M. A. El-Sayed, J. Phys. Chem. B 103 (1999) 8410.
[25] L. M. Liz-Marzan, Mater Today 7 (2004) 26.
[26] P. K. Jain, X. Huang, I. H. El-Sayed, M. A. El-Sayed, Plasmonics 2 (2007) 107.
[27] Y. Sun, B. Mayers, Y. Xia, Nano Lett. 3 (2003) 675.

[28] E. Hao, R. C. Bailey, G. C. Schatz, J. T. Hupp, S. Li, Nano Lett. 4 (2004) 327.
[29] M. Hu, J. Chen, Z. Y. Li, L. Au, G. V. Hartland, X. Li, M. Marquez, Y. Xia, Chem. Soc. Rev. 35 (2006) 1084.
[30] S. Eustis, M. A. El-Sayed, Chem. Rev. Soc. 35 (2006) 209.
[31] www.nanohybrids.net
[32] X. Huang, M. A. El-Sayed, J. Adv. Res. 1(2010) 13.
[33] R. Gans, Ann. Phys. 47 (1915) 270.
[34] S. Link, M. B. Mohamed, M. A. El-Sayed, J. Phys. Chem. B 103 (1999) 3073.
[35] S. Link, M. A. El-Sayed, J. Phys. Chem. B 109 (2005) 10531.
[36] A. Brioude, X. C. Jiang, M. P. Pileni, J. Phys. Chem. B 109 (2005) 13138.
[37] B. Yan, Y. Yang, Y. Wang, J. Phys. Chem. B 107 (2003) 9159.
[38] S. Eustis, M. A. El-Sayed, J. Appl. Phys. 100 (2006) 044324.
[39] H. Chen, X. Kou, Z. Yang, W. Ni, J. Wang, Langmuir 24 (2008) 5233.
[40] E. Prodan, C. Radloff, N. J. Halas, P. Nordlander, Science 302 (2003) 419.
[41] W. C. Law, K. T. Yong, A. Baev, P. N. Prasadan, ACS Nano 5 (2011) 4858.
[42] M. Liu, P. Guyot-Sionnest, J. Mater. Chem. 16 (2006) 3942.
[43] B. Saute, R. Premasiri, L. Ziegler, R. Narayanan, Analyst. 137 (2007) 5082.
[44] G. A. Wurtz, R. Pollard, W. Hendren, G. P. Wiederrecht, D. J. Gosztola, V. A. Podolskiy, A. V. Zayats.
[45] P. K. Jain, S. Eustis, M. A. El-Sayed, J. Phys. Chem. B 110 (2006)18243.
[46] L. Shao, K. C. Woo, H. J. Chen, Z. Jin, J. F. Wang, H.-Q. Lin, ACS Nano 4 (2010) 3053.
[47] B. Willingham, D. W. Brandl, P. Nordlander, Appl. Phys. B: Lasers Opt. 93 (2008) 209.
[48] C. Tabor, D. Van Haute, M. A. El-Sayed, ACS Nano 3 (2009) 3670.
[49] N. J. Halas, S. Lal, W.-S. Chang, S. Link, P. Nordlander, Chem. Rev. 111 (2011) 3913.
[50] H. Chen, L. Shao, Q. Li, J. Wang, Chem. Soc. Rev. 42 (2013) 2679.
[51] M. Faraday, Philos. Trans. 147 (1857) 145.
[52] N. R. Jana, L. Gearheart, C. J. Murphy, Adv. Mater. 13 (2001) 1389.
[53] B. Nikoobakht, M. A. El-Sayed, Chem. Mater. 15 (2003) 1957.
[54] X. Ye, L. Jin, H. Caglayan, J. Chen, G. Xing, C. Zheng, V. Doan-Nguyen, Y. Kang, N. Engheta, C. R. Kagan, C. B. Murray, ACS Nano 6 (2012) 2804.
[55] J. Peŕez-Juste,L. M. Liz-Marzań, S. Carnie, D. Y. C. Chan, P. Mulvaney, Adv. Funct. Mater. 14 (2004) 571.
[56] G. Gramlich, J. Zhang, W. M. Nau, J. Am. Chem. Soc. 124 (2002) 11252.
[57] C. J. Murphy, T. K. Sau, A. M. Gole, C. J. Orendorff, J. Gao, L. Gou, S. E. Hunyadi, T. Li, J. Phys. Chem. B 109 (2005) 13857.
[58] M. Liu, P. Guyot-Syonnest, J. Phys. Chem. B 109 (2005) 22192.
[59] C. J. Orendorff, C. J. Murphy, J. Phys. Chem. B 110 (2006) 3990.
[60] E. Herrero, L. J. Buller, H. D. Abruna, Chem. Rev. 101 (2001) 1897.
[61] X. Huang, S. Neretina, M. A. El-Sayed, Adv. Mater. 21 (2009) 4880.
[62] J. Peŕez-Juste, I. Pastoriza-Santos, L. M. Liz-Marzań , P. Mulvaney, Coord. Chem. Rev. 249 (2005) 1870.
[63] L. Scarabelli, A. Sańchez-Iglesias, J. Peŕez-Juste, L. M. Liz-Marzań, J. Phys. Chem. Lett. 6 (2015) 4270.
[64] C. J. Ward, R. Tronndorf, A. S. Eustes, M. L. Auad, E. W. Davis, J. Nanomater. 2014 (2014) 765618.
[65] Q. Wei, J. Ji, J. Shen, J. Nanosci. Nanotechnol. 8 (2008) 5708.
[66] N. Niidome, T. Niidome, Gold annorods: application to bioscience and medicine. In Nano

Biophotonics ed. H. Masuhara, S. Kawata, F. Tunaka, Oxford: Elsevier (2006) 297.

[67] S. Gomez-Grana, F. Hubert, F. Testard, A. Guerrero-Martinez, I. Grillo, L. M. Liz-Marzań, O. Spalla, Langmuir 28 (2012) 1453.

[68] C. Kinnear, H. Dietsch, M. J. D. Clift, C. Endes, B. Rothen-Rutishauser, A. Petri-Fink, Angew. Chem. Int. Ed. 52 (2013) 1934.

[70] L. Vigderman, B. P. Khanal, E. R. Zubarev, Adv. Mater. 24 (2012) 4811.

[71] A. Kopwitthaya, K.T. Yong, R. Hu, I. Roy, H. Ding, L.A. Vathy, E.J. Bergey and P.N. Prasad, Nanotechnology, 21 (2010) 315101.

[72] R.G. Rayavarapu, W. Petersen, L. Hartsuiker, P. Chin, H. Janssen, F.W. van Leeuwen, C. Otto, S. Manohar and T.G. van Leeuwen, Nanotechnol. 21 (2010) 145101.

[73] C. Grabinski, N. Schaeublin, A. Wijaya, H. D'Couto, S.H. Baxamusa, J. Hamad-Schifferli and S.M. Hussain, ACS Nano, 5 (2011) 2870.

[74] X. S. Kou, S. Z. Zhang, C.-K. Tsung, G. D. Stucky, L. D.Sun, J. F. Wang, C. H. Yan, J. A. Chem. Soc. 129 (2007) 6402.

[75] X. S. Kou, Z. H. Sun, Z. Yang, H. J. Chen, J. F. Wang, Langmuir 25 (2009)1692.

[76] A. Wijaya, K. Hamad-Schifferli, Langmuir 24 (2008) 9966.

[77] J. Perez—Juste, M. A. Correa-Duarte, L. M. Liz-Marzań, Appl. Surf. Sci. 226 (2004) 137.

[78] X. H. Huang, I. H. El-Sayed, W. Qian, M. A. El-Sayed, J. Am. Chem. Soc. 128 (2006) 2115.

[79] E.B. Dickerson, E.C. Dreaden, X. Huang, I.H. El-Sayed, H. Chu, S. Pushpanketh, J.F. McDonald, M.A. El-Sayed, Cancer Lett. 269 (2008) 57.

[80] T. B. Huff, L. Tong, Y. Zhao, M.N. Hansen, J. X. Cheng, A. Wei, Nanomed. 2 (2007) 125.

[81] L. Tong, Y. Zhao, T.B. Huff, M. N. Hansen, A. Wei, J. X. Cheng, Adv. Mater. 19 (2007) 3136.

[82] M. Thakur, B. C. Lentle, Radiology 236 (2005) 753.

[83] N. R. Jagannathan, Curr. Sci. 92 (2007)1061.

[84] I. H. El-Sayed, X. Huang, M. A. El-Sayed, Nano Lett. 5 (2005) 829.

[85] S. A. Boppart, A. L. Oldenburg, C. Xu, D. L. Marks, J. Biomed. Opt. 10 (2005) 041208.

[86] A. G. Tkachenko, H. Xie, D. Coleman, W. Glomm, J. Ryan, M. F. Anderson, S. Franzen, D. L. Feldheim, J. Am. Chem. Soc. 125 (2003) 4700.

[87] V. P. Zharov, D. O. Lapotko, IEE J. Sel. Top. Quantum Electron. 11 (2005) 733.

[88] T. B. Huff, M. N. Hansen, L. Tong, Y. Zhao, H. Wang, D. A. Zweifel, J. X. Cheng, A. Wei, Proc. SPIE- Int. Soc. Opt. Eng. 6448 (2007) 64480D.

[89] D. Yelin, D. Oron, S. Thiberge, E. Moses, Y. Silberg, Opt. Express 11 (2003)1385.

[90] P. C. Li, C. W. Wei, C. K. Liao, C. D. Chen, K. C. Pao, C. R. C. Wang, Y. N. Wu, D. B. Shieh, IEEE, Trans Ultrason, Ferroelect. Freq. Control 54 (2007)1642.

[91] L. Tong, Y. Zhao, T. B. Huff, M. N. Hansen, A. Wei, J.-X. Cheng, Adv. Mater. 19 (2007) 3136.

[92]T. Sun, G. J. Diebold, Nature 355 (1992) 806.

[93] M. Eghtedari, A. Oraevsky, J. A. Copland, N. A. Kotov, A. Conjusteau, M. Motamedi, Nano Lett. 7 (2007)1914.

[94] K. Aslan, J. R. Lakowicz, C. D. Geddes, Curr. Opin. Chem. Biol 9 (2005) 538.

[95] G. J. Nusz, S. M. Marinakos, A. C. Curry, A. Dahlin, F. Hook, A. Wax, A. Chilkoti, Anal. Chem. 80 (2008) 984.

[96] L. B. Wang, Y. Y. Zhu, L. G. Xu, W. Chen, H. Kuang, L. Q. Liu, A. Agarwal, C. L. Xu, N. A. Kotov, Angew. Chem., Int. Ed. 49 (2010) 5472.

[97] M. Rex, F. E. Hernandez, A. D. Campiglia, Anal. Chem. 78 (2006) 445.

Chapter 1

Synthesis of Small Gold Nanorods with Tunable Aspect Ratio

Synthesis of Small Gold Nanorods with Tunable Aspect Ratio*

* *Unpublished results from a work in collaboration with Dr. Chang Soo Kim and Prof. V. M. Rotello (University of Massachusetts, Amherst)*

Graphical abstract

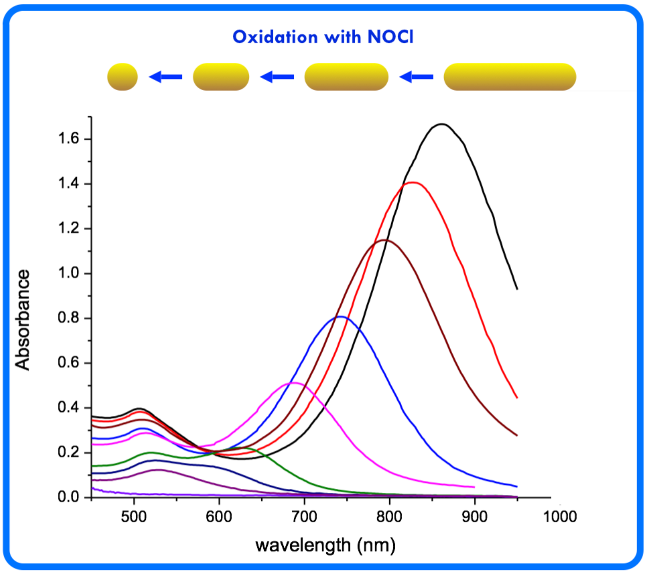

1. Introduction

Rod-shaped gold nanoparticles, namely gold nanorods (GNRs) have received a great attention in recent years due to their unique plasmonic properties. In fact, GNRs exhibit two distinct localized surface plasmon resonance (SPR): the transversal mode in the visible region (TSPR) and the longitudinal one in the upper visible or near-infrared part of the spectrum (LSPR) that correspond to the oscillations perpendicular or parallel to the rod length direction, respectively. [1] The LSPR can be tailored to a particular wavelength [2]. There is a linear relationship between the absorption maximum of the LSPR band and the mean aspect ratio (AR, ratio between the length and the width of the rod) of GNRs, which can be tuned during the synthesis [3].

The size and AR are the primary factors that determine the optical properties of GNRs (including the technological relevant phototermal aspects), and their surface reactivity.[4] In the synthesis of GNRs, control over the size and AR has been one of the most important and challenging tasks. [5] In particular, several modifications of the seed-mediated growth method by Nikoobakht et al. [3,6,7] have been reported to synthesize GNRs of different AR and with a width greater than 8 nm and length depending on the silver ion content [8]. However, with these methods it is difficult to synthesize small sized GNRs while there is an increasing demand of small sized GNRs for medical applications because of their high-payload-to carrier ratio (e.g. drug delivery) [9] and their clearance in in-vivo studies [10]. More recently, a seedless growth technique has been published by M. A. El-Sayed et al. [11], describing a one-step synthesis of GNRs with low dimensions and AR by direct reduction of Au(III) ions with $NaBH_4$. The key factor of this synthesis to obtain different size of GNRs is the concentration of $NaBH_4$ used in the growth solution. However, since the critical step of this synthesis is the concentration of $NaBH_4$ which is added to the unstirred solution, only few millilitres (10-15 ml) of GNRs can be synthesized. In fact, when $NaBH_4$ is added to a higher volume of the solution, a gradient of concentration occurs and the growth of GNRs is not homogeneous.

Moreover, the common issue of all the synthetic procedures is the reproducibility of the synthesis. Specifically, since the LSPR of GNRs is highly sensitive to small changes of the AR it is difficult to synthesize two batches of GNRs with the same wavelength of the LSPR with a good control.

Therefore, several methods have been proposed to decrease the length of GNRs after synthesis, through a selective oxididation of the ends of GNRs by addition of oxidizing agents such as $FeCl_3$ [12], H_2O_2 [13] or through the combination of a lower pH and a higher temperature [14]. However, in all these cases small sized GNRs have never been obtained.

In the present chapter a method for the selective shortening of GNRs to produce small-sized nanorods with a good control over the LSPR is illustrated.

2. Results

Synthesis of small GNRs with tunable AR

The synthesis of small gold nanorods with tunable length (and AR) was performed following the seeded growth method according to Nikoobakht et al. [3] and Ratto et al. [6] with slight modifications. Shortly, the idea was to synthesize GNRs with a higher AR and, thereafter, selectively oxidize GNRs in situ to obtain GNRs with tunable length.

Firstly, the synthesis was modified increasing the amount of seeds injected in the GNRs' growth solution as well as the amount of silver nitrate (AgNO3). In fact, it is well known that an increase of AgNO3, as well as the amount of seeds results in an increase of the AR (and a smaller width). [15] Figure 1 reports the extinction spectra and TEM images of GNRs obtained by adding 9 times more seeds than the normal synthesis [6] and different concentrations of $AgNO_3$.

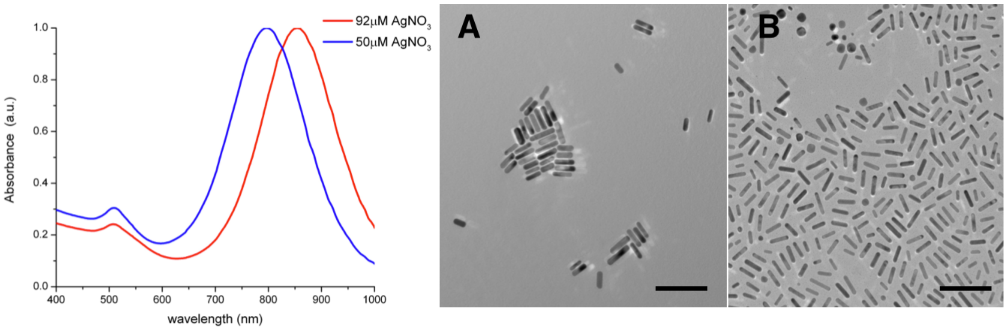

Figure 1. Extinction spectra and TEM images of GNRs obtained with $AgNO_3$ 50 μM (A) or 92 μM (B).

GNRs synthesized with a lower amount of silver nitrate showed AR of 3.9 ± 0.8, with a width of 7.5 ± 1.0 nm and length of 28.6 ± 3.5 nm (LSPR at 789 nm), while the AR of GNRs obtained with a higher content of $AgNO_3$ was 4.8 ± 0.5, the width 6.3 ± 0.9 and length 30.1 ± 4.8 (LSPR at 860 nm). It is evident that an increase of silver nitrate results in GNRs with a higher AR but similar length and thinner width, as reported in literature [3]. Therefore a selective shortening through oxidation of GNRs with AR 4.8 would results in GNR with a lower AR and length but similar width.

To perform the selective oxidation of GNRs a 250 ml glass bottle used for GNRs' synthesis was treated with freshly prepared aqua regia (details are reported in the

Experimental Section), then washed 10 times with milli-Q water and used immediately for GNRs synthesis and successive oxidation. GNRs synthesized and stored in this treated glass bottle showed a considerable change in the extinction spectra.

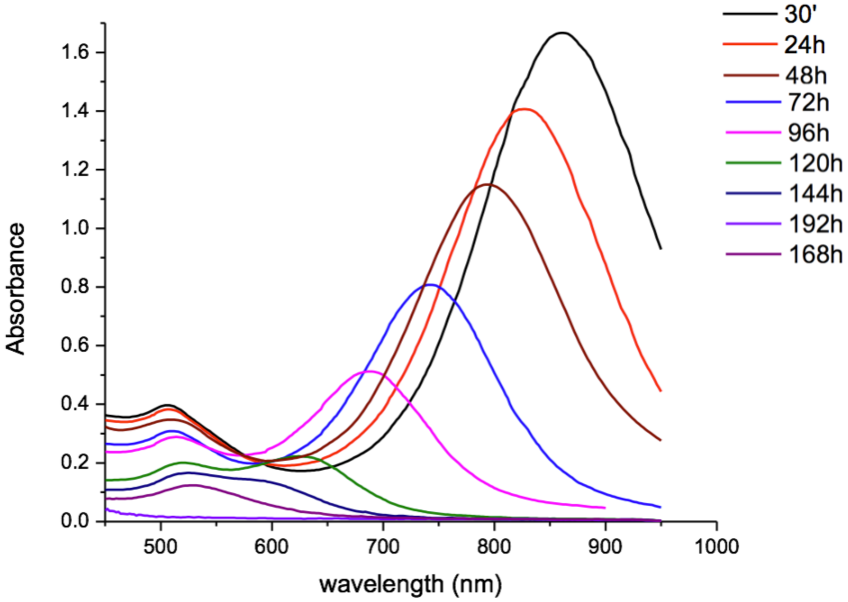

Figure 2. Time course extinction spectra of GNRs during the oxidation.

Figure 2 shows the extinction spectra of GNRs acquired after 30 minutes from the seeds injection in the growth solution and every 24 hours for one week. GNRs after 30 minutes exhibit two extinction bands corresponding to the longitudinal and transversal plasmon resonances, respectively at 860 nm and 510 nm. Thereafter, the oxidation of GNRs by NOCl adsorbed on the glass surface of the glass container occurred.

During the oxidation a time-dependent blue-shift and a decrease of the intensity of the LSPR was detected, while the TSPR remains approximately at 510 nm, indicating a lowering of the AR of GNRs [4].

TEM images of three samples collected during the oxidation showed that after 30 minutes the LSPR of GNRs was at 860 nm with a size of (29.5±5.2 × 6.1±0.9) nm and AR 4.8±0.6 (Figure 3A), after 48 hours the LSPR was at 795 nm, the size (21.0±3.5×5.5±0.5) nm and AR 3.8±0.6 (Figure 3B), and after 72 hours the LSPR was at 755 nm, the size (17.1± 2.8 ×5.0± 0.5) nm and AR 3.4 ± 0.4 (Figure 3C).

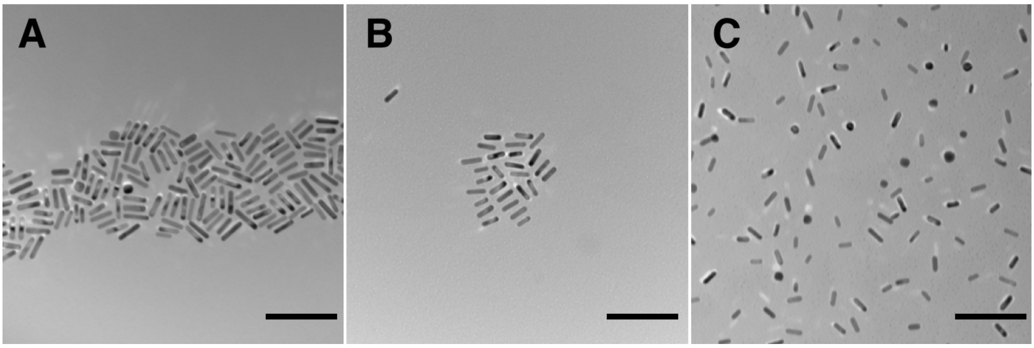

Figure 3. TEM images of GNRs collected after 30 minutes (A), 48h (B) and 72h (C) from seeds injection in the growth solution. Scale bar: 100nm

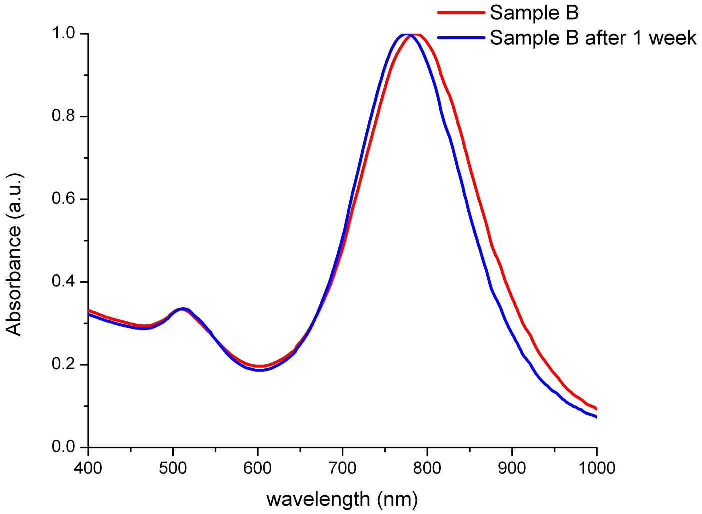

Figure 4. Extinction spectra of GNRs collected after 48h and stored in a plastic container. Spectra are recorded immediately after the synthesis (sample B) and after 1 week.

Moreover, after one week, when the oxidation process reached completion, the solution was colorless, indicating the presence of Au(I) and not Au(III) ions in solution. Thereafter, the possibility to scale up the synthesis was tested, performing the synthesis in a 1l glass bottle with 500 ml of growth solution. GNRs with similar size of the smaller batch were obtained. Figure S1 and Figure S2 illustrate, respectively, the TEM images and the extinction spectra of GNRs collected in two different stage of the process. Interestingly, samples collected during the oxidation and stored in plastic containers did not show significant changes in the extinction spectrum during the time, indicating that the speed of the oxidation was significantly reduced. Figure 4 shows the changing of the spectra of sample B (GNRs collected after 48h) stored in a plastic container during one week: only a 10 nm blue-shift of the LSPR was detected, while the TSPR did not show any changes.

Tuning the speed of the oxidation

In order to tune the speed of GNR's oxidation in the glass bottle, the number of washing cycles with milli-Q water was changed. Specifically, the time course of the extinction spectra of GNRs synthesized in a glass bottle after 8 washing cycles was recorded. It is evident that in this case the oxidation occurred faster in the first case (Figure 5).

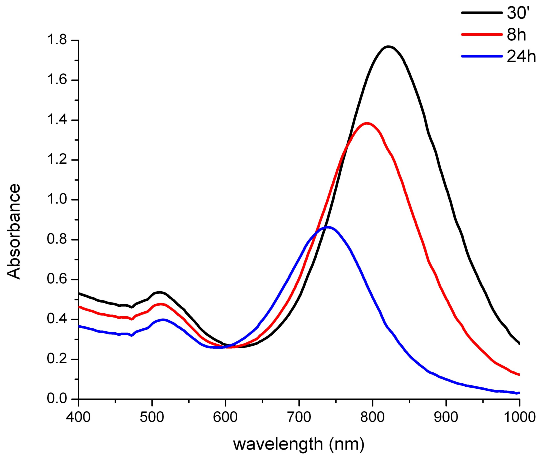

Figure 5. Time course extinction spectra of GNRs synthesized in a glass bottle washed 8 times with milli-Q water after treatment with aqua regia.

In another experiment, aqua regia prepared one week before the synthesis was used for the treatment of the bottle. The extinction spectra of GNRs recorded during the synthesis are reported in Figure 6. As it can be clearly seen, the speed of the oxidation was definitely lower than for GNRs synthesized in the glass bottle treated with freshly prepared aqua regia.

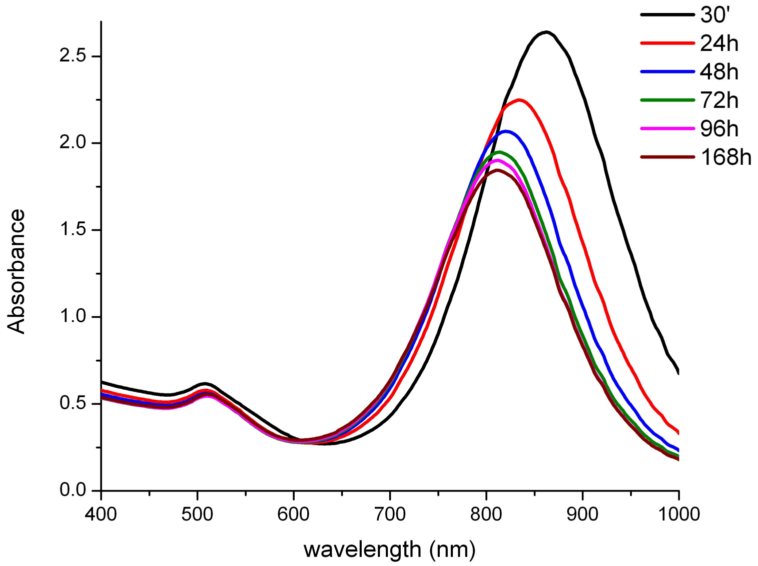

Figure 6. Extinction spectra of GNRs synthesized in a glass bottle treated with “old” aqua regia.

In Figure 6 GNRs exhibit a blue-shift of the LSPR from 854 nm to 810 nm within 72h and then remain stable, indicating that the oxidation occurred only during the first three days.

Subsequently, the effect of the lowering of the pH during the synthesis was tested. Therefore hydrochloric acid was added during the synthesis to obtain a growth solution at pH 1. The effect of the direct addition of HCl is illustrated in Figure 7. In these conditions the oxidation occurred faster respect to the synthesis performed without addition of HCl (pH 3). Results are consistent with the experiments reported in literature in which the direct addition of HCl combined with a high temperature (90°C) results in a consistent blue-shift of the LSPR and selective shortening of GNRs.[16]

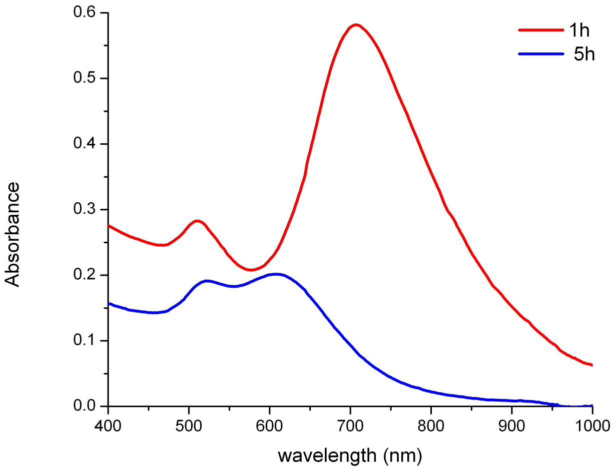

Figure 7. Time course extinction spectra of GNRs synthesized at pH 1.

A comparison with the selective shortening with $FeCl_3$

In literature several methods for the selective shortening of GNRs are reported. In order to compare GNRs synthesized in a pretreated glass bottle with those methods, a selective shortening of GNRs with $FeCl_3$[12] was reproduced in the same laboratory.

The oxidation was performed on GNRs with higher AR (see Figure S1) simply by addition of 5 mM $FeCl_3$ in the GNRs solution. The oxidation was fast and the LSPR of GNRs showed a blue-shift of approximately 40 nm in only 10 minutes.

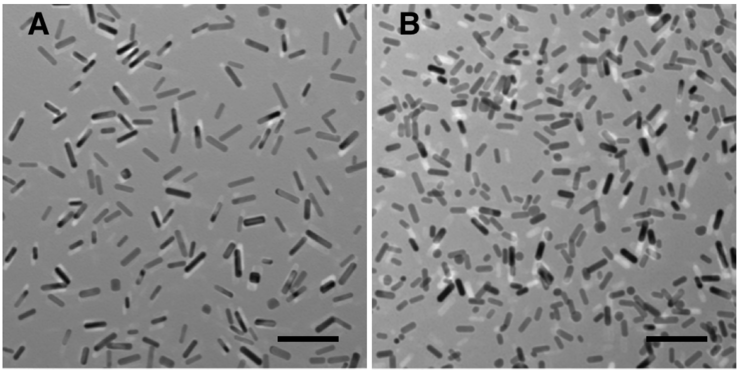

Figure 8. TEM images of GNRs before (A) and after (B) oxidation with 5mM $FeCl_3$. Scale bars: 100 nm

Thereafter GNRs were centrifugated, the supernatant removed and then resuspended in water to stop the oxidation. Figure 8 reports the TEM images of GNRs before and after the oxidation, while Figure 9 shows the extinction spectra of GNRs before and after 10 minutes of oxidation as well as after the centrifugation. It is evident that the process cannot be interrupted immediately since the oxidation occurred even during the centrifugation as it can be seen in the extinction spectra in Figure 9.

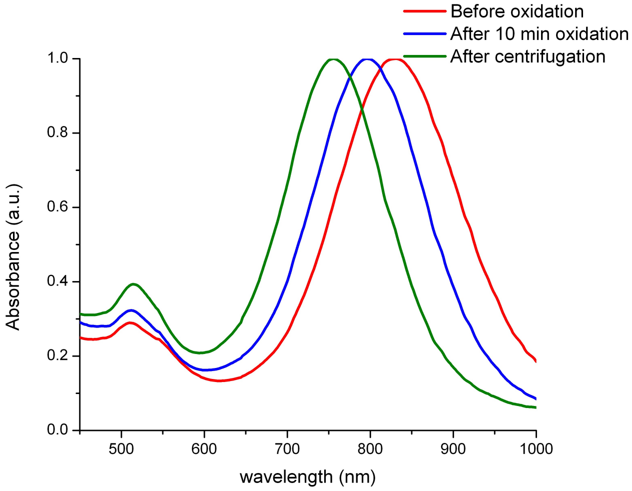

Figure 9. Extinction spectra of GNRs before and after oxidation with 5 mM $FeCl_3$.

Moreover, GNRs obtained though the oxidation with $FeCl_3$ were bigger than GNRs obtained through the synthesis in a pretreated glass bottle. The difference in size of GNRs obtained through these methods is illustrated in the TEM images in Figure 10. Specifically, the size of GNRs obtained after etching with $FeCl_3$ was 7x26nm.

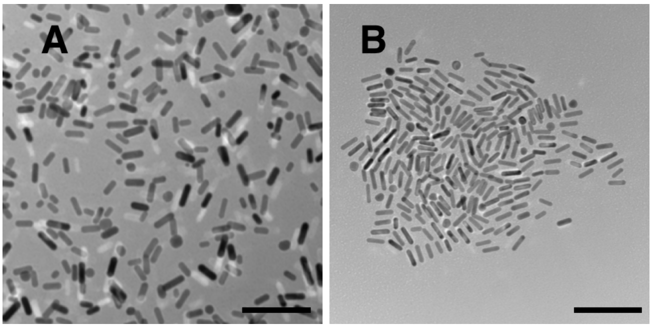

Figure 10. TEM images of GNRs after etching with $FeCl_3$ (A) compared to GNRs obtained after 48h in the glass bottle (B). Scale bars: 100nm

3. Discussion

The key term of the GNRs' oxidation is the pretreatment with aqua regia ($HCl:HNO_3$, 3:1) of the glass bottle used for the synthesis. During this process hydronium ions (H_3O^+) exchange protons for the alkali ions leaching from the glass network.

$$H_3O^+ + {=}Si{-}O^- Na^+ \rightarrow {=}Si{-}OH + H_2O + Na^+$$

This process results in a hydrated silica-rich surface layer, sometimes referred to as gel layer [15].

Moreover, the combination of hydrochloric and nitric acids produces nitrosyl chloride (NOCl), according to the following reaction:[17]

$$HNO_3 + 3\ HCl \rightarrow Cl_2 + 2\ H_2O + NOCl$$

NOCl is a strong oxidizing agent and its adsorption on glass surfaces, and subsequent release by pumping, has been demonstrated by E. M. Stoddart [18]. Therefore, if the glass bottle treated with aqua regia is used immediately without any further treatment, the surface is saturated with NOCl which can be released during the GNR's synthesis.

Therefore the release of NOCl along with the presence of a considerable concentration of bromide in solution (from CTAB) can promote the selective shortening of GNRs through oxidation of Au into the colorless $AuBr_2^-$, but not into the yellow $AuBr_4^{3-}$. Table S1 reports the standard reduction potentials of the half reactions involved in the oxidation process.

It is well-known that GNRs of AR 2-5, prepared in the presence of surfactants (i.e. CTAB) have unstable {110} facets [18]. Moreover, due to the presence of CTAB, which adsorbs preferentially on {100} facets, both growth and shortening reactions occur mainly at the ends of single-crystalline GNRs.[12]

Therefore, thanks to the presence of NOCl released from the glass bottle, the oxidation of GNRs occurred mainly at the ends of the rod leading to a shortening of the nanorods. These results are in agreement with a previous work by Stucky et al. [14] . However, in this latter case the oxidation occurred only at the ends of the rods, while in the present work it is evident that the oxidation occurred also on the surface along the rods. Moreover, in this synthesis an increase of the temperature was not to necessary to speed up the oxidation and the process could be interrupted simply removing the solution from the glass bottle and store GNRs in a plastic container.

The speed of the oxidation can be controlled by varying the number of washings with milli-Q water after treatment with aqua regia or lowering the pH by addition of HCl. In fact, if the glass bottle was washed 8 times the oxidation process was faster than the same synthesis performed after 10 washings, presumably due to the higher amount of NOCl that can be released. In the other case, the addition of HCl enhances the oxidation rate of GNRs because the addition of H+ increases the reduction potential of the half-reaction of O_2, which can also be involved [14] . In fact, in this latter experiment the oxidation could be interrupted only through centrifugation and washing. [14]

A proof of the effect of NOCl adsorption on the glass wall of the bottle is the experiment performed after treatment with “old” aqua regia. In this case the oxidation was slow and after 72h further shortening was not detected, indicating that all the NOCl was already released. In fact, in nitric acid NOCl is readily oxidized into nitrogen dioxide; therefore, presumably, when“old” aqua regia is used for the treatment less NOCl can be adsorbed on the glass surface, reducing its oxidizing effect on GNRs.

4. Conclusions

In the present chapter a method to synthesize GNRs with a size smaller than those obtained with the seeded-growth method is illustrated. This novel method consists of an in-situ oxidation of GNRs directly during the synthesis through pretreatment of the glass bottle used for the synthesis. The NOCl release-mediated oxidation of GNRs can be interrupted simply removing the solution from the treated glass container, allowing a good control of the AR and the LSPR of GNRs. Therefore the problem of a continuos oxidation during the centrifugation and washing, which is necessary to stop the oxidation in common shortening process [14], can be avoided. Moreover, contrary to the seedles method [11], the present synthesis can be scaled up and considerable amount of GNRs can be synthesized. In a future work this system could be engineered for the production of GNRs in continuos through the use of a reservoir of GNRs and pumping nanorods in a treated glass tube. Therefore, the control of GNRs’ flow into the glass tube could provide GNRs with different length in a large scale.

5. Experimental section

Materials

Sodium borohydride (>98%), cetyltrimethylammonium bromide (>99%), and silver nitrate (99.5%) were purchased from Acros Organics. Chloroauric acid (99.9%) was purchased from Strem Chemical, and L-(+)-ascorbic acid was purchased from Alfa Aesar, while polysorbate 20 (Tween20) was obtained from Sigma Aldrich. All chemicals were used as received. All the solutions were prepared with deionized water produced by a Millipore System.

GNR synthesis

GNRs' synthesis was performed in a 250 ml glass bottle. Before synthesis the bottle was filled with approximately 100 ml of freshly prepared aqua regia ($HCl:HNO_3$, 3:1) and gently shaked. Thereafter, aqua regia was left in the bottle overnight and then removed. After the cleaning with aqua regia, the bottle and the magnetic stir bars were thoroughly washed (8-10 times) with 100 ml of Milli-Q water and immediately used for the synthesis of GNRs with tunable length. For the synthesis of GNRs with AR of 4.9, the glass bottle was left overnight in milli-Q water and dried before use. GNRs were synthesized by a seed-mediated method according to Nikoobakht et al. [3] and Ratto et al.[6] modified as follows.

1) Preparation of the seeds

CTAB (218.5 mg) was added in a 20 ml glass vial with a small stir bar. Then 6 ml of milli-Q water were added and CTAB was dissolved by heating at 37°C and gently stirring the solution with a stirring/hot plate, to obtain a solution of 0.1 M CTAB. $HAuCl_4$ 0.01M (144 µl) was added and the solution was gently stirred. The vial was covered with aluminium foil and the speed of the stirring was increased. Thereafter, $NaBH_4$ 0.015 M (229.5 µl) was quickly added and the solution was stirred for 10 minutes. After the addition of $NaBH_4$ the solution changed color, from orange to yellow brownish, indicating the formation of gold seeds. Then the stirring was stopped and the seeds solution was left undisturbed in the dark for 1 hour and 50 minutes.

2) *GNRs' growth*

CTAB (4.05 g) was added in a 250 ml glass bottle with 100 ml of milli-Q water and a big stirring bar. The solution was heated at 37°C and gently stirred to allow the dissolution of CTAB. Then $HAuCl_4$ 0.1M (470 µl) was added and the solution was stirred for a while. Subsequently, $AgNO_3$ 0.1 M (92 µl for GNRs with AR 4.8 and GNRs with tunable length obtained with the oxidation; 48 µl for GNRs AR of 3.9 ± 0.8, with a width of 7.5 ± 1.0 nm and length of 28.6 ± 3.5 nm (LSPR at 789 nm)was added and the solution was gently stirred. AA 0.01 M (4.5 ml) was added drop-wise with a burette to the solution continuously stirred. During the addition of AA the solution changed color, from orange to colorless, indicating that Au(III) was reduced to Au(I). Thereafter the 15% more AA (0.675 ml) and Tween 20 10% (1 ml) were added and the solution was gently stirred. The glass bottle was covered with aluminium foil and the speed of the stirring increased before seeds addition. Finally, 1.8 ml of the seeds solution was quickly added to the growth solution and stirred for 30 minutes. The color of the growth solution turned to brown, indicating the formation of gold nanorods.

Then GNRs where stored as follows, depending on the type of synthesis performed.

A) Synthesis of GNRs with tunable length: after 30 minutes the stirring was stopped and the GNRs' oxidation started. When the desired AR was obtained, the reaction was stopped removing the growth solution from the glass bottle and stored in plastic containers and stored in the dark at room temperature.

B) Synthesis of GNRs with AR 4.8: after 30 minutes from seeds injection the GNRs' solution was simply stored in the dark at room temperature.

All the GNRs were then washed as reported in Chapter 1.

GNRs characterization

After the synthesis, the structural and optical properties of GNRs were characterized by Transmission Electron Microscopy (TEM) and spectrophotometric analysis. TEM images were acquired on a JEOL 200FX with a tungsten filament operating at 200 kV. Optical extinction spectra were recorded using a Molecular Devices SpectraMax M2 plate reader.

UV-vis-NIR

After the synthesis 700 µl of the growth solution was put into a disposable plastic cuvette and the spectrum of GNRs was recorded between 400 nm and 1000 nm with a step of 2 nm. A solution of CTAB 0.1 M (700 µl) was used as a reference for the measurement.

TEM

A TEM sample was prepared as follow: a small amount of the growth solution (1.5 ml) was washed as reported in Chapter 1. After washing 10 µl of the GNRs solution was carefully deposited with a pipet on the TEM grid, the sample was then covered and stored overnight to allow a slow drying of the drop on the TEM grid. The sample was analyzed with the transmission electron microscope.

Determination of the size

The size of the GNRs was estimated as follow: the sizes of 300 GNRs were measured with ImageJ software and the average width, length and AR were calculated.

6. Supporting Informations

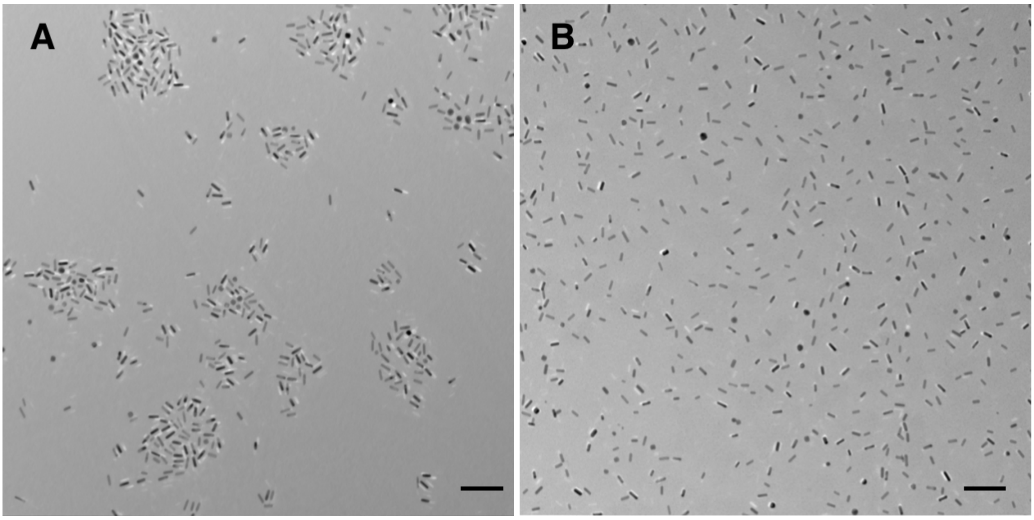

Figure S1. TEM images of GNRs collected after 48h (A) and 72h (B) from a 500 ml batch. Scale barr: 100nm.

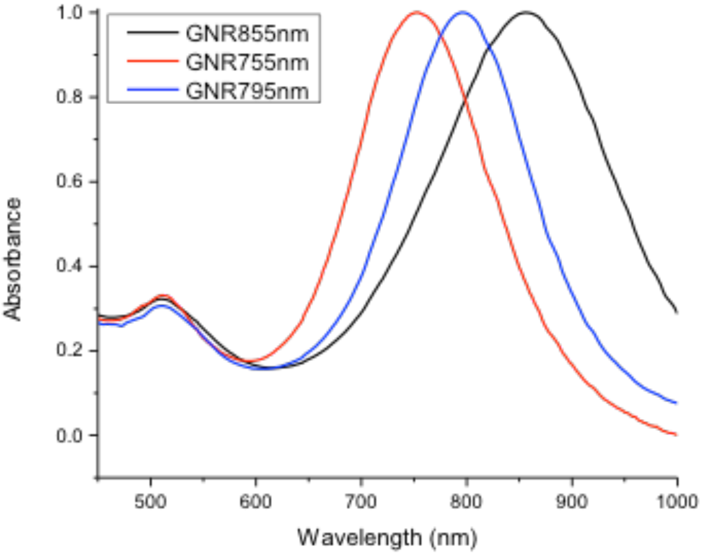

Figure S2. Normalized extinction spectra of GNRs collected during the synthesis of 500 ml batch.

Table S1. Standard reduction potentials of some related half reactions

Half reaction	Standard reduction potential (E°)
$NO^+ + e \rightarrow NO$	~ 1.2 V*
$O_2 + 4H^+ + 4e \rightarrow 2H_2O$	1.229 V
$AuBr_2^- + e \rightarrow Au + 2Br^-$	0.959 V
$AuBr_4^- + 3e \rightarrow Au + 4Br^-$	0.854 V
$AuCl_4^- + 2H^+ + 2e \rightarrow Au + 4Cl^-$	1.776 V

From “Electrochemical Series”, in CRC Handbook of Chemistry and Physics, Internet Version 2005; Lide, D. R., Ed.; <http://www.hbcpnetbase.com>; CRC Press: Boca Raton, FL, 2005.
*The reduction potential of NO^+ to NO has been measured in non aqueous media and estimated for water [20].

Acknowledgments

The present work was financially supported by Beneficentia Stiftung (Vaduz, Liechtestein) and the National Institutes of Health (EB014277 and GM077173).

References

[1] M.A. Garcia, J. Phys. D: Appl. Phys. 44 (2011) 283001.
[2] C.J. Murphy, C.J. Orendorff, Adv. Mater. 17 (2005) 2173.
[3] B. Nikoobakht, M.A. El-Sayed, Chem. Mater. 15 (2003) 1957.
[4] E.B. Dickerson, E.C. Dreaden, X. Huang, I.H. El-Sayed, H. Chu, S. Pushpanketh, J.F. McDonald, M.A. El-Sayed, Cancer Lett. 269 (2008) 57.
[5] T. K. Sau, C. J. Murphy, J. Am. Chem. Soc. 126 (2004) 8648.
[6] F. Ratto, P. Matteini, F. Rossi, R. Pini, J. Nanopart. Res. 12 (2010) 2029.
[7] X. Ye, L. Jin, H. Caglayan, J. Chen, G. Xing, C. Zheng, V. Doan-Nguyen, Y. Kang, N. Engheta, C. R. Kagan, and C. B. Murray, ACS Nano, 2012, 6 (3), pp 2804–2817.
[8] X. Huang, S. Neretina, M. A. El-Sayed, Adv. Mater. 21 (2009) 4880.
[9] X. Huang, S. Neretina, M. A. El-Sayed, Adv. Mater. 21 (2009) 4880.
[10] L. Tong. H-Wei, Y. Zhang, W. Zheng, J. X. Cheng, Langmuir, 25 (2009) 12454.
[11] M. R. K. Ali, B. Snyder, M. A. El-Sayed, Langmuir 28 (2012) 9807.

[12] R. Zou, X. Guo, J. Yang, D. Li, F. Peng, L. Zhang, H. Wang, H. Yua, Cryst. Eng.Comm,.11 (2009) 2797.

[13] W. Ni, X. Kou, Z. Yang, J. Wang, ACS Nano 4 (2008) 667.

[14] C. K. Tsung, X. Kou, Q. Shi, J. Zhang, M. H. Yeung, J. Wang, G. D. Stucky, J. Am. Chem. Soc. 128 (2006) 5352.

[15] S. Davison, Conservation and Restoration of Glass, Elsevier Science, 2003.

[16] L. J. Beckham, W. A. Fessler, M. A. Kise 48 (1951)319.

[17] E. M. Stoddart J. Chem. Soc. (1944) 388.

[18] Z. L. Wang, R. P. Gao, B. Nikoobakht, M. A. El-Sayed, J. Phys. Chem. B 104 (2000) 5417.

[19] P. C. Ford et al. Reaction mechanisms of nitric oxide in Advances in Inorganic Chemistry: inorganic reaction mechanisms. Vol 54, Academic Press 2003.

Chapter 2

Rapid Purification of Small Gold Nanorods

Rapid Purification of Small Gold Nanorods*

* *F. Scaletti, C. S. Kim, L. Messori, V. M. Rotello, Rapid Purification of Gold Nanorods for Biomedical Applications. MethodsX 1 (2014) 118-123.*

Graphical abstract

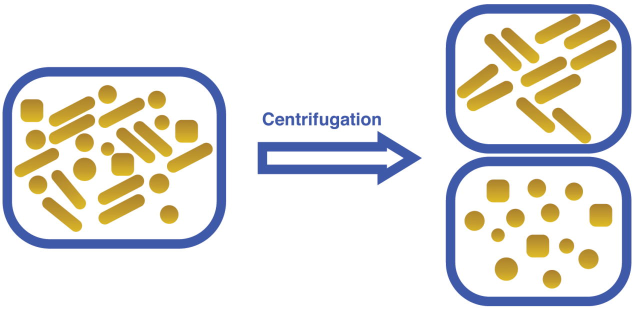

1. Introduction

Among the various gold NPs, gold nanorods (GNRs) have attracted particular attention due to their unique properties (structural, optical, and electronic) [1,2]. Moreover, facile and well-established synthetic routes (e.g., seed-mediated growth protocol [3]) permit to produce stable structures of GNRs with high yield and monodispersity.

However, the common synthetic method of GNRs, such as the seed-mediated method [3], produces a variety of gold spheres and cubes as by-products. Several methods such as selective precipitation [4,5] or oxidation [6], size exclusion chromatography [7], electrophoresis [8], and centrifugation [9,10], have been reported for the purification of high AR (AR > 4), relatively big sized GNRs (width ≥ 10 nm). Moreover, it is difficult to separate small sized GNRs while there is an increasing demand of small GNRs because of their strong absorption properties [11] and their high-payload-to-carrier ratio (e.g., drug delivery) [12]. Here, a method for the separation of small GNRs has been optimized. This method does not require the addition of surfactant or salts. Moreover, a large amount of GNRs can be easily obtained from by-products with a high yield.

2. Results and Discussion

Method of purification

The final reaction mixture for GNRs contains the desired GNRs, a variety of gold nanoparticles (NPs) of different shapes (spherical, cubic, etc.). To obtain a homogeneous population of GNRs, two cycles of centrifugation were carried out. After the synthesis, all reaction products (spheres, cubes, and rods) were first isolated and purified from the excess of cetyltrimethylammonium bromide (CTAB) through centrifugation at high rpm. CTAB needs to be removed as much as possible for many applications owing to its cytotoxicity [13]. Then, shape separation was afforded through a second cycle of centrifugation adapted from the method reported by Sharma et al. [9] and optimized for the size of interest.

Due to the large shape-dependent differences in the respective sedimentation velocities, in the course of centrifugation, spheres and cubes were sedimented at the bottom of the centrifuge tube while most GNRs remained in the supernatant solution. Therefore, an efficient shape separation can be achieved by tuning the centrifugation times and speeds (see Materials and Methods section).

In order to choose the best conditions of separation, different time and the speed of centrifugation have been tested as reported in SI section.

Characterization of purified GNRs

After separation, the colors of the solutions of the three samples were clearly different as shown in Fig. 1. In fact before separation the solution of reaction products was reddish brown (Sample A) and after the second cycle of centrifugation the solutions of purified GNRs and by-products were brown (Sample B) and red (Sample C), respectively.

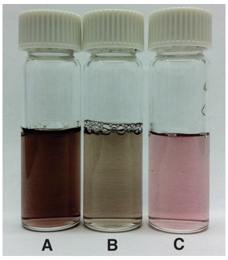

Figure 1. Separation of gold nanorods from reaction products. The figure shows the reaction products after the first centrifugation (A), the supernatant after the shape separation (B), and the resuspended precipitate (C).

Moreover, the structural and optical properties of the separated NPs (Samples B and C) were characterized by optical extinction spectra and TEM images, compared to Sample A (Figures 2 and 3). The absorption spectrum relative to Sample A (Figure 2) showed a transversal surface plasmon peak with a maximum at 514 nm and a broadening at longer wavelength, indicating the presence of GNRs and spherical and cubical NPs as well. The absorption spectrum of Sample C showed that, after the separation, the maximum of the surface plasmon peak was at 522 nm while the spectrum relative to Sample B showed a transversal surface plasmon peak with a maximum at 510 nm. These differences indicated the loss of spherical and cubical NPs in Sample B while the bulk of the by-products were in Sample C. Moreover, the longitudinal surface plasmon peak with a maximum at 800 nm in the absorption spectra of Sample C indicated that some GNRs were present as well.

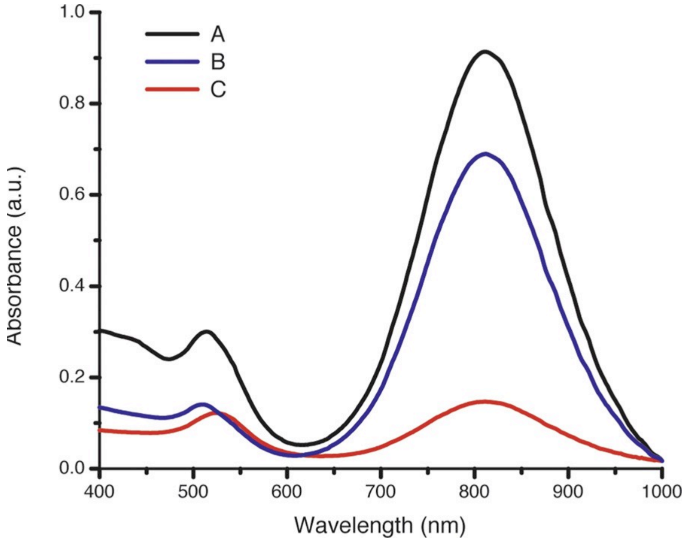

Figure 2. Absorption spectra of reaction products after the first centrifugation (A), the supernatant after the shape separation (B), and the resuspended precipitate (C).

The size and shape of the reaction products (Sample A) and separated NPs (Sample B and Sample C) are shown in the TEM images (Figure 3). As a result, Sample B (Figure 3B) was comprised mainly of GNRs while Sample C (Figure 3C) contained mostly spherical NPs, confirming the shape separation by the two steps of centrifugation.

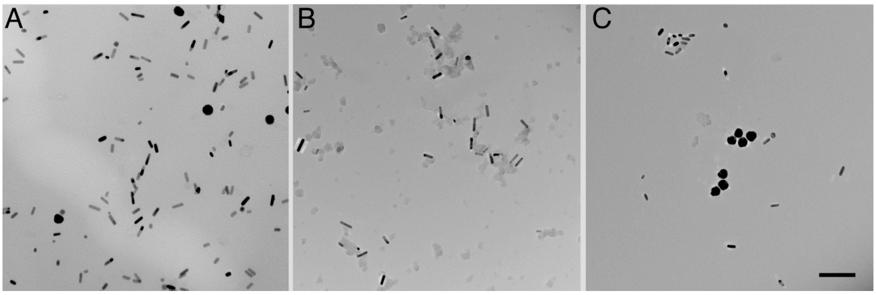

Figure 3. TEM images of reaction products after the first centrifugation (A), the supernatant after the shape separation (B), and the resuspended precipitate (C). Scale bar: 100 nm.

Quantification of the separation

The quantification of the separation was evaluated in terms of volume percentage of by-products (spheres and cubes) or GNRs respect to the total volume of all the reaction products (Figure 4).

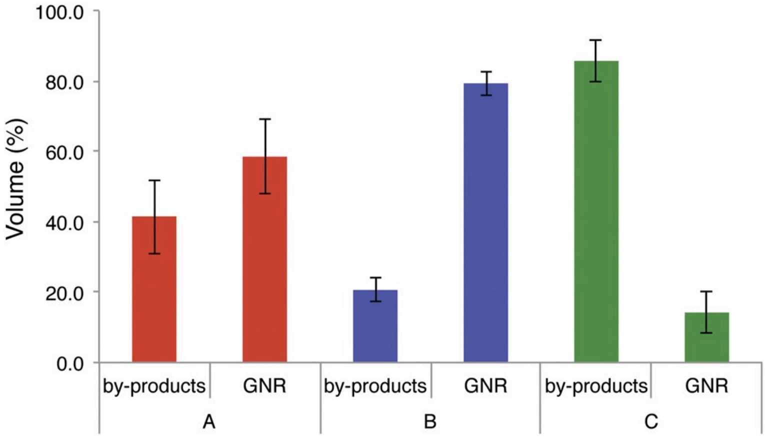

Figure 4. Volume percentage of by-products (spheres and cubes) and GNRs in the sample after the first centrifugation (A), in the supernatant after the shape separation (B), and in the resuspended precipitates (C).

Before separation, Sample A was comprised of 41.5% of by-products and 58.5% of GNRs (Figure 4A). After separation, Sample B contained 79.4% of GNRs and 20.6% of by-products while Sample C consisted 14.2% of GNRs and 85.8% of by-products. As shown in Figure 1, it is important to notice that the sizes (and the volumes) of most by-products were larger than the size of GNRs, implying that even a small amount of by-products greatly affect the total volume of the sample.

3. Conclusions

In the present Chapter a modified method for the purification of small GNRs from reaction by-products (i.e. spherical and cubic nanoparticles or aggregates) is accurately described. Contrary to other methods, the present one does not require the addition of surfactant or salts and large amount of GNRs can be easily separated from by-products with a high yield.

4. Experimental section

Materials

Sodium borohydride (>98%), cetyltrimethylammonium bromide (>99%), and silver nitrate (99.5%) were purchased from Acros Organics. Chloroauric acid (99.9%) was purchased from Strem Chemical, and L-(+)-ascorbic acid was purchased from Alfa Aesar. All chemicals were used as received. All the solutions were prepared with deionized water produced by a Millipore System.

GNR synthesis

GNRs, with AR of 3.9 ± 0.5 (width= 7.5 ± 0.8 nm, length= 28.6 ± 3.5 nm) were synthesized by a seed-mediated method according to Nikoobakht et al. [14] and Ratto et al. [15] modified according to the synthetic procedure reported in Chapter 1. After the synthesis, the structural and optical properties of GNRs were characterized by Transmission Electron Microscopy (TEM) and spectrophotometric analysis. TEM images were acquired on a JEOL 200FX with a tungsten filament operating at 200 kV. Optical extinction spectra were recorded using a Molecular Devices SpectraMax M2 plate reader.

Method

The GNRs were separated from excess CTAB and then purified from the by-products through centrifugation with an Eppendorf centrifuge 5810R using 2 ml centrifuge tubes. During centrifugation, temperature was kept at 27°C to avoid the crystallization of CTAB that may affect the separation.

Step 1: GNR separation from CTAB

The purification from excess of CTAB and unreacted Au(I) as follow:

- Synthesized GNRs were placed in centrifuge tubes (1.5 ml of GNRs for each centrifuge tube) and centrifuged at the rate of 10630 rpm (12000 × g) for 30 min. After centrifugation, precipitates can be clearly seen at the bottom of the centrifuge tubes.

- The supernatant was carefully removed with a pipet, leaving a volume of ~50 μl solution with the precipitates.

- The precipitates were resuspended by addition of 1.45 ml of Milli-Q water, leading to a final volume of 1.5 ml.

- The resuspended GNRs were then combined (Sample A).

Step 2: Shape separation

- The isolated products from the first centrifugation were placed in centrifuge tubes (1.5 ml for each centrifuge tube) and centrifuged at the rate of 6000 rpm (3824 g) for 15 min.

- The supernatant (GNRs) was carefully collected with a pipet (Sample B), leaving ~50 ml of the solution with the precipitates in the centrifuge tubes.

- The precipitates at the bottom (spheres and cubes) in the 50 ml of the solution were resuspended by the addition of 1.45 ml of Milli-Q water, leading to a final volume of 1.5 ml.

- All the resuspended GNRs were then combined (Sample C).

Step 3: Quantification of the separation

The quantification of the separation was estimated as follow:

- The sizes of 300 NPs (spheres, cubes and GNRs) for each sample were measured with ImageJ software: spherical NPs showed the average diameter of 28.6 ± 4.7 nm, cubes showed the average side length of 14.1 ± 2.9 nm while GNRs showed a width of 7.5 ± 0.8 nm and length of 28.6 ± 3.5 nm.

- The volumes of spherical, cubical NPs and GNRs were calculated; to calculate the volume of GNR, the shape of GNR was approximated to a cylinder capped with two half-spheres.

- The quantification of the separation was expressed in terms of volume percentage of by-products (spheres and cubes) or GNRs respect to the total volume of all the reaction products (Figure 4).

5. Supporting Informations

The following is an other example of separation of a GNRs' batch with a high amount of spherical by-products.

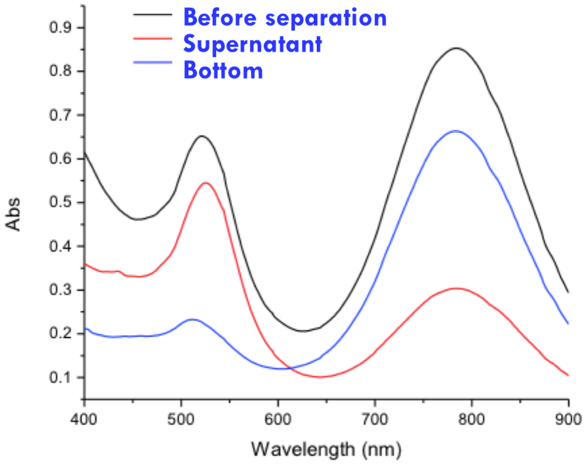

Figure S1. An other example of absorption spectra of reaction products after the first centrifugation (black line), the supernatant after the shape separation (blue line), and the resuspended precipitate (red line).

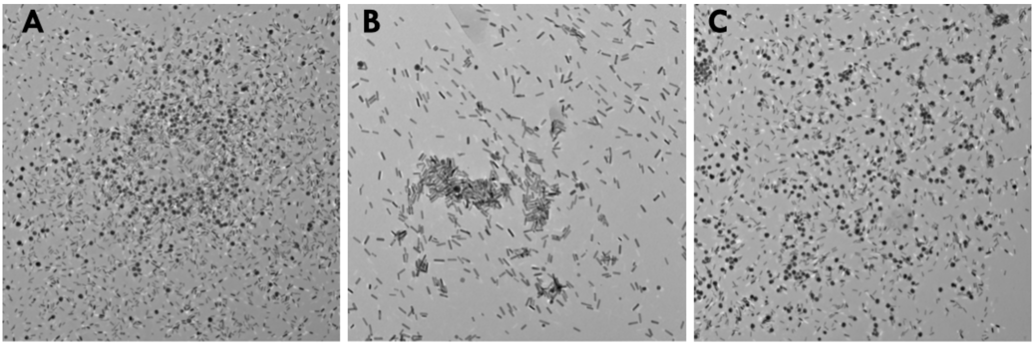

Figure S2. TEM images of reaction products after the first centrifugation (A), the supernatant after the shape separation (B), and the resuspended precipitate (C).

In order to choose the best conditions of separation, different time and the speed of centrifugation have been tested as reported below.

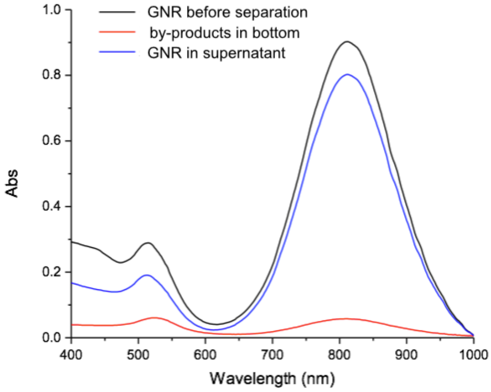

Figure S3. Absorption spectra of GNRs purified through a first centrifugation at 10630 rpm (black line) and a second one at 6000rpm for 5 minutes.

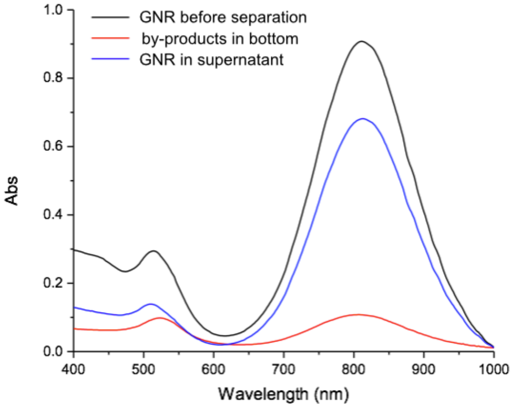

Figure S4. Absorption spectra of GNRs purified through a first centrifugation at 10630 rpm (black line) and a second one at 5000rpm for 15 minutes.

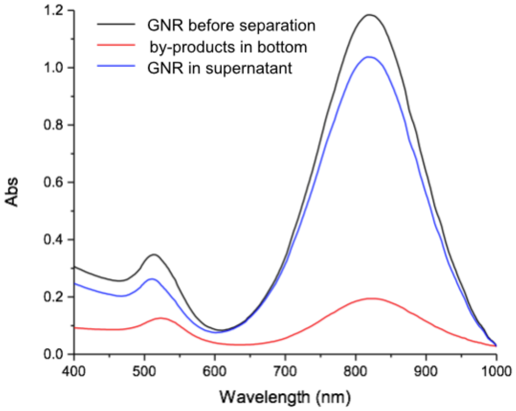

Figure S5. Absorption spectra of GNRs without the first centrifugation at 10630 rpm (black line) and purified only with a centrifugation at 6000rpm for 15 minutes.

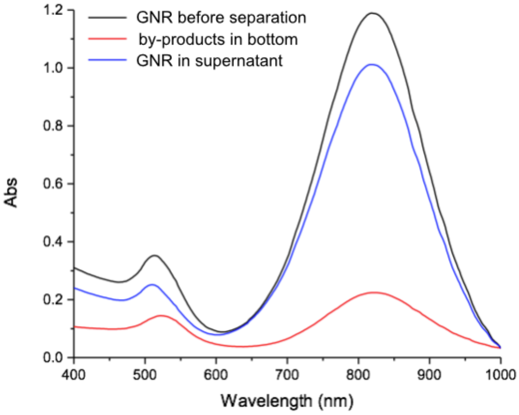

Figure S6. Absorption spectra of GNRs without the first centrifugation at 10630 rpm (black line) and purified only with a centrifugation at 5000rpm for 15 minutes.

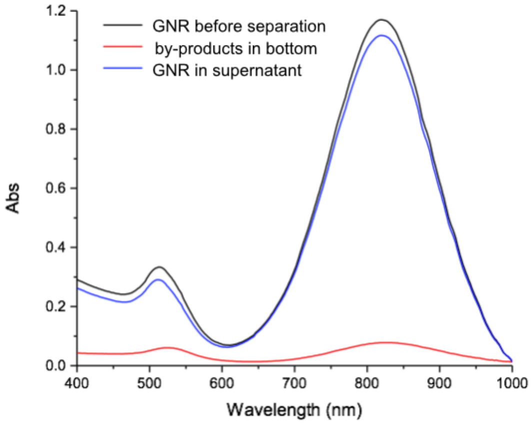

Figure S7. Absorption spectra of GNRs without the first centrifugation at 10630 rpm (black line) and purified only with a centrifugation at 6000rpm for 5 minutes.

Acknowledgments

The present work was financially supported by Beneficentia Stiftung (Vaduz, Liechtestein) and the National Institutes of Health (EB014277 and GM077173).

References

[1] S. Eustis, M. A. El-Sayed, Chem. Soc. Rev. 35 (2006) 209.

[2] J. Perez-Juste, I. Pastoriza-Santos, L.M. Liz-Marzan, P. Mulvaney, Coord. Chem. Rev. 249 (2005) 1870.

[3] N.R. Jana, L. Gearheart, C.J. Murphy, Adv. Mater. 13 (2001) 1389.

[4] N.R. Jana, Chem. Commun. (2003) 1950.

[5] K. Park, H. Koerner, R.A. Vaia, Nano Lett. 10 (2010) 1433.

[6] B.P. Khanal, E.R. Zubarev, J. Am. Chem. Soc. 130 (2008) 12634.

[7] G.T. Wei, F.K. Liu, C.R. Chris Wang, Anal. Chem. 71 (1999) 2085.

[8] M. Hanauer, S. Pierrat, I. Zins, A. Lotz, C. Sonnichsen, Nano Lett. 7 (2007) 2881.

[9] V. Sharma, K. Park, M. Srinivasarao, Proc. Natl. Acad. Sci. U.S.A. 106 (2009) 4981.

[10] O. Akbulut, C.R. Mace, R.V. Martinez, A.A. Kumar, Z. Nie, M.R. Patton, G.M. Whitesides, Nano Lett. 12 (2012) 4060.

[11] M.A. Mackey, M.R.K. Ali, L.A. Austin, R.D. Near, M.A. El-Sayed, J. Phys. Chem. B 118 (2014) 1319.

[12] Q. Wei, J. Ji, J. Shen, Macromol. Rapid. Commun. 29 (2008) 645.

[13] S. Wang, W. Lu, O. Tovmachenko, U.S. Ray, H. Yu, P.C. Ray, Chem. Phys. Lett. 463 (2008) 145.

[14] B. Nikoobakht, M.A. El-Sayed, Chem. Mater. 15 (2003) 1957.
[15] F. Ratto, P. Matteini, F. Rossi, R. Pini, J. Nanopart. Res. 12 (2010) 2029.

Chapter 3

Size Dependent Biological profiles of PEGylated Gold Nanorods

Size Dependent Biological profiles of PEGylated Gold Nanorods*

* *F. Tatini, I. Landini, F. Scaletti, L. Massai, S. Centi, F. Ratto, S. Nobili, G. Romano, F. Fusi, L. Messori, E. Mini, R. Pini, Size dependent biological profiles of PEGylated gold nanorods. J. Mater. Chem. B 2 (2014) 6072-6080.*

Graphical abstract

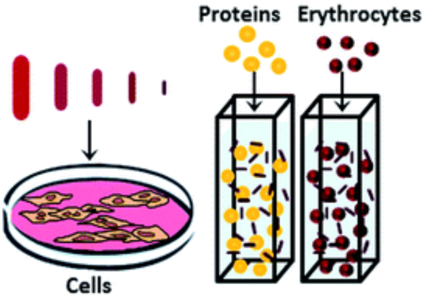

1. Introduction

The cellular applications of plasmonic particles in the context of biomedical optics, ranging from imaging and diagnostics to therapeutics, have received considerable attention over recent years[1-5]. With actual perspectives to reach the clinical arena, the need for well-characterized and biocompatible particles is becoming urgent. However, in spite of an increasing number of studies, the available data in the scientific literature remain fragmented and heterogeneous.[6,7] Among the various plasmonic particles, so-called gold nanorods (GNRs) are attracting particular interest because of their unique optical properties [8], extreme efficiency and stability of photothermal conversion [9] and biochemical versatility. Their optical absorbance exhibits two intense resonances that correspond to orthogonal modes of plasmonic oscillations, i.e. a transversal mode in the green region and a longitudinal mode in a range of frequencies that may be tuned in the far red-near infrared window (650-1000 nm) of principal interest in biomedical optics [8].

The wavelength of this resonance depends on the particle shape and in particular the aspect ratio (i.e. length divided by diameter, AR), with the particle size playing a secondary role [10,11]. Other factors of impact on the frequency of both transversal and longitudinal bands are the refractive index of the environment and particle aggregation. [12] All these features make GNRs ideal contrast agents and sensitizers for applications such as the photoacoustic imaging [13] and the optical hyperthermia of cancer. [14]

Crucial features of GNRs include their coating, shape and size. The kind of coating is critical to modulate their interface with the biological systems, enable to bind functional moieties such as ligands and govern the colloidal stability in culture media and body fluids. Polyethylene glycol (PEG) is perceived as the coating of choice because of its biocompatibility, [15-17] ability to avoid the detection from macrophages, readiness of biochemical modification and steric hindrance against particle aggregation.

As it was mentioned, the choice of particle shape follows from the need for specific spectral features. Therefore, particle size remains the principal variable to play with. Particle size may modulate critical parameters such as: the cellular penetration, [18,19] the intracellular localization, [20] the biodistribution, [21] features that depend on specific surface area, including the rate of interaction with proteins, residual toxicity of contaminants or load of ligands, [20] the ratio of optical absorption to scattering, [11] the efficiency and stability of photothermal conversion and the optical and thermal hotspot distribution. [22] As mentioned above, for individual GNRs, the light extinction cross sections roughly scale with the particle volumes. [9,11] Therefore, in order to maintain the same optical absorbance, one should compare samples containing the same gold molarity, rather than e.g. the same particle density by number.

In the present chapter, an extensive survey on the characterization, stability, toxicity and cellular uptake of PEGylated GNRs (PEG-GNRs) of five different size classes is presented.

A critical requirement for biomedical applications of GNRs is their colloidal stability in physiological buffers. Previous studies showed that gold nanoparticles exposed to biological fluids may become coated with proteins, [23,24] which may modify their conformation, thus causing a loss of their biological activity, [25] elicit an altered immune response and modulate their biodistribution and cellular uptake.

Here, the effect of particle size on the stability of PEG-GNRs in biological buffers and their interactions with significant proteins, such as the hen egg white lysozyme (HEWL), cytochrome c (cyt c) and bovine serum albumin (BSA) has been addressed. The correlation between size and toxicity of gold nanoparticles of various shapes has been investigated in a few cases with alternate results. [16,21,26-30]

While as-synthesized cetyltrimethylammoium (CTAB)-stabilized GNRs impart significant cellular damage, PEG-GNRs display little cytotoxicity. [17,31,32] This cytotoxicity may persist from the retention of contaminants used in the synthesis, such as CTAB and silver ions, which may explain the correlation between particle surface area and cellular damage [16,33] and project a stronger toxicity for smaller particles. [21,27,34] To my knowledge, the effect of size on the cytotoxicity and cellular uptake of PEG-GNRs has never been reported before, which requires a careful examination of multiple parameters including cell proliferation, viability, membrane integrity and blood compatibility. Moreover, in order to avoid a possible bias that may affect existing data [7] due to the use of HeLa cells with their anomalous phenotype, we resort to a battery of cellular models. Finally, the size of PEG-GNRs may affect their cellular uptake by nonspecific interactions, which is another critical issue in view of biomedical applications. Although the available literature is inconclusive, [6] particle size was found to modulate their cellular uptake and determine different mechanisms of internalization. [6,23] In this chapter, all these issues are scanned in a range of particle concentrations of common use in preclinical trials for therapeutic applications in rodents, i.e. in the order of 10 mg Au/ Kg tissue, or 50 μM Au. [35-38]

2. Results

Size and shape of gold nanorods

In order to be as representative as possible, PEG-GNRs were prepared by usual protocols with slight modifications to tune their size statistics. In particular, GNRs were synthesized by the common seed-mediated approach, [39,40] where particle growth is triggered by the injection of gold nuclei in a growth solution and develops without additional nucleation. [39,41] The initial seed density equals the final particle density and so dictates the average particle size, because the ions in the growth solution are shared in either of a larger number of smaller particles or a smaller number of larger particles. Instead the typical particle AR exhibits little dependence on the initial seed density. Here, these notions were exploited to modulate the average particle size at comparable shape statistics.

Figure 1 displays a spectroscopic and microscopic analysis of five different size of GNRs.

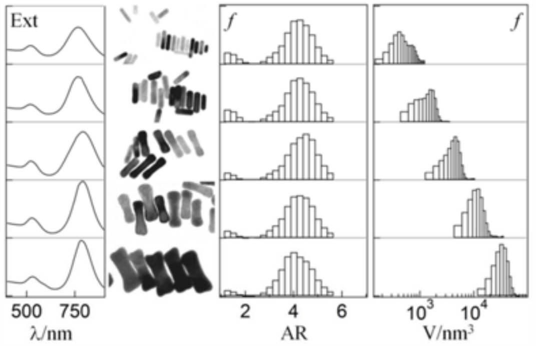

Figure 1. Light extinction spectra, representative (170 × 100) nm^2 TEM micrographs, volumetric distributions of particle aspect ratios and volumes of samples GNRs **1/9**, **1/3**, **1**, **3** and **9** from top to bottom.

From sample to sample, the experimental spectra are consistent in terms of peak intensities and positions, which reflect their sameness of gold molarity [22,41,42] and typical particle shapes, respectively. The transmission electron micrographs corroborate our predictions on the trends of particle volumes and AR with the seed density. The volumetric distributions of particle AR are consistent from sample to sample, despite subtle modifications of particle shapes, such as lesser quasi spherical byproducts and more dogbone profiles [39,43] at lower seed densities. Instead, typical particle volumes scale well with the inverse of the seed density. The average particle effective radii are (19.4 ± 0.4), (13.5 ± 0.3), (9.8 ± 0.2), (6.8 ± 0.4) or (4.8 ± 0.5) nm. We note that the overlap between the volumetric distributions of particle volumes of every second sample is rather negligible.

After synthesis, GNRs were PEGylated by standard methods for gold nanoparticles and substrates. [44] By the use of dynamic light scattering, we found that the hydrodynamic thickness of the PEG shells in PBS was about 13-18 nm for all samples, which suggests a so-called brush [45] configuration and a density in the order of 0.8 PEG strands per nm. Purification from contaminants was pursued by extraction in a common surfactant such as polysorbate 20 and five cycles of centrifugation and decantation. Additional details on sample preparation are given in the Experimental section. This variety of particle sizes covers the range of principal interest for biomedical applications, smaller particles beginning to display poor plasmonic oscillations [46] and larger particles becoming problematic for blood circulation.[47]

Hereafter, GNR's samples will be labelled with the numbers **9**, **3**, **1**, **1/3**, **1/9**, which indicate their relative average particle volumes with respect to sample **1**. The latter corresponds to a standard size of ~ 41 nm average length per ~ 10 nm average diameter.

Stability of PEGylated gold nanorods

PEG-GNRs proved to be stable in the most common buffers for cell biology and in the presence of representative proteins. In order to understand the stability of PEG-GNRs in the presence of representative biological components, we monitored possible variations of their plasmonic bands at ~520 and ~780 nm, which display high sensitivity to particle aggregation,[12] protein adsorption [48] and charge injection.[49,50].

Therefore, the stability of the various PEG-GNRs in the presence of relatively large concentrations of representative proteins in PBS was tested. Experiments were performed at 37°C, in an attempt to represent physiological conditions. Three different proteins were chosen for these tests, namely BSA (Figure 2), HEWL and cyt c (Figures S1 and S2 of the SI section). The choice of these proteins was guided by their importance, globular structure, stability, solubility and availability. Their addition up to a final concentration of 10 μM did not significantly affect the plasmonic bands of all PEG-GNRs. Only minor shifts were noticed around 780 nm in a few cases.

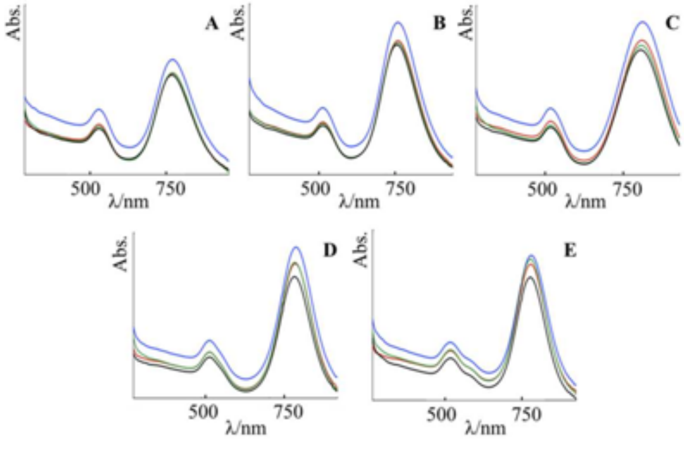

Figure 2. Light extinction spectra of PEG-GNRs of different average size in PBS containing BSA A) GNRs **1/9**; B) **1/3**; C) **1**; D) **3**; E) **9**. The figure shows spectra recorded at time zero (black line) and after 1 h (green line), 24 h (red line) and 168 h (blue line).

The onset of partial flocculation and sedimentation led to a modest decrease in optical density over one week. The case of cyt c is particularly informative, as this protein exhibits an intense Soret band around 400 nm, arising from its heme cofactor. This feature allowed us to simultaneously monitor both the protein and the particles. No significant changes were observed right after mixing nor after two days, which implies a substantial weakness of possible interactions. However, after one week of incubation a partial reduction of cyt c was noticed as it can be seen from the appearance of the typical spectrum of the cyt c's reduced form. [51] It is known that the cyt c in solution may reach an equilibrium between the oxidized and reduced form.[52] Therefore, the subsequent blue-shift of the GNRs' longitudinal band may be ascribed to the charge injection due to cyt c reduction. Direct evidence of this weakness comes from the possibility to readily separate these species by centrifugation. The residual amount of cyt c adsorbed on PEG-GNRs turned out to be negligible, as it is shown in Figure S3 of the SI section.

The effects of addition of RPMI medium (Figure 3) was also analyzed. For all PEG-GNRs, a significant and progressive red-shifts of the main bands at 780 nm occurred. This process is relatively slow and reaches completion in a few days. In agreement with previous reports, red-shifts imply changes in the local environment of the PEG-GNRs. [49,50] It is hypotesized that this effect may follow from the interplay of partial PEG substitution and selective adsorption of different components in a complex environment such as RPMI. [52] Notably, the spectra of PEG-GNRs with BSA differ much from those in RPMI. Therefore, BSA alone cannot be responsible for the modifications seen in RPMI. [26]

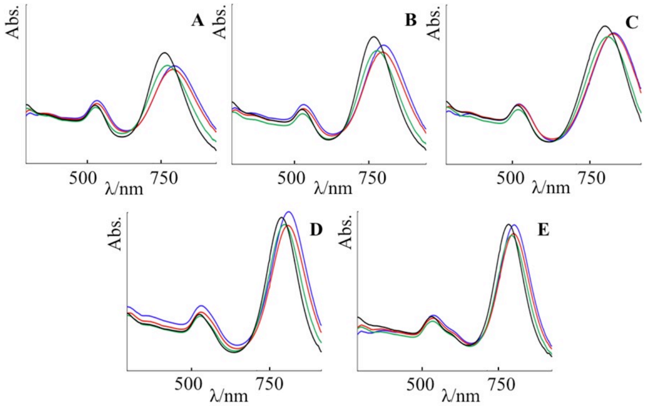

Figure 3. Stability of PEGylated gold nanorods in RPMI. Light extinction spectra of PEG-GNRs of different average size in RPMI A) GNRs **1/9**; B) **1/3**; C) **1**; D) **3**; E) **9**. The figure shows spectra recorded at time zero (black line) and after 24h (green line), 72h (red line) and 168h (blue line).

Cytotoxicity and cell viability

PEG-GNRs did not significantly affect the cell viability and were not cytotoxic, with the exception of the smallest size class. In order to evaluate the cytotoxic effects of PEG-GNRs, we combined two quantitative colorimetric assays indicating both survival/ growth and viability of cultured cells. The inhibition of cell growth was assessed by the SRB test, which measures the total amount of proteins, and therefore the presence of cells, in the microtiter plates. Cell viability was analyzed by the MTT test, which quantifies the reduction of tetrazolium salts by metabolically active cells. MTT is the test of choice in many studies on particle toxicity, thus enabling a direct comparison with the available literature.[33] Furthermore, the effect of an acute treatment with PEG-GNRs on cell membrane integrity was evaluated. The combination of different tests is important because the biological activity of gold nanoparticles and its mechanisms of action remain largely unknown and the output of each individual test may be biased by the interference with the particles.

Table 1 Inhibitory effect of 5 different suspensions of PEG-GNRs on cell growth of HeLa, A2780/S, SKOV3 and IGROV-1 cell lines after 72 and 168 h exposure.

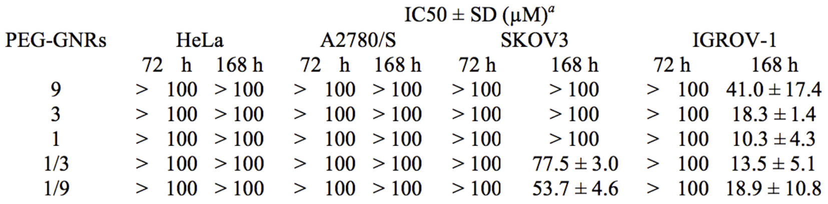

	IC50 ± SD (μM)[a]							
PEG-GNRs	HeLa		A2780/S		SKOV3		IGROV-1	
	72 h	168 h	72 h	168 h	72 h	168 h	72 h	168 h
9	> 100	> 100	> 100	> 100	> 100	> 100	> 100	41.0 ± 17.4
3	> 100	> 100	> 100	> 100	> 100	> 100	> 100	18.3 ± 1.4
1	> 100	> 100	> 100	> 100	> 100	> 100	> 100	10.3 ± 4.3
1/3	> 100	> 100	> 100	> 100	> 100	77.5 ± 3.0	> 100	13.5 ± 5.1
1/9	> 100	> 100	> 100	> 100	> 100	53.7 ± 4.6	> 100	18.9 ± 10.8

[a] IC50 is defined as the concentration of drug required to inhibit cell growth by 50%; SD, standard deviation; data represent the mean of three independent experiments each performed in triplicate.

- *Cell growth inhibition.*

  The cytotoxic effects of PEG-GNRs were evaluated against four tumor cell lines (HeLa, A2780/S, SKOV3 and IGROV-1) after 72 and 168 hours exposure (Table 1 and Figure 4). After 72 hours, 50% inhibitory cell growth thresholds (IC50) were not reached at gold concentrations up to 100 μM. However, at the highest concentration (100 μM Au), some inhibition was observed. Such an effect varied among the different cell lines: lower in HeLa cells (range 2.5-7.9%) and higher in IGROV-1 cells (range 35.9-46.3%), but without a clear pattern to particle size.

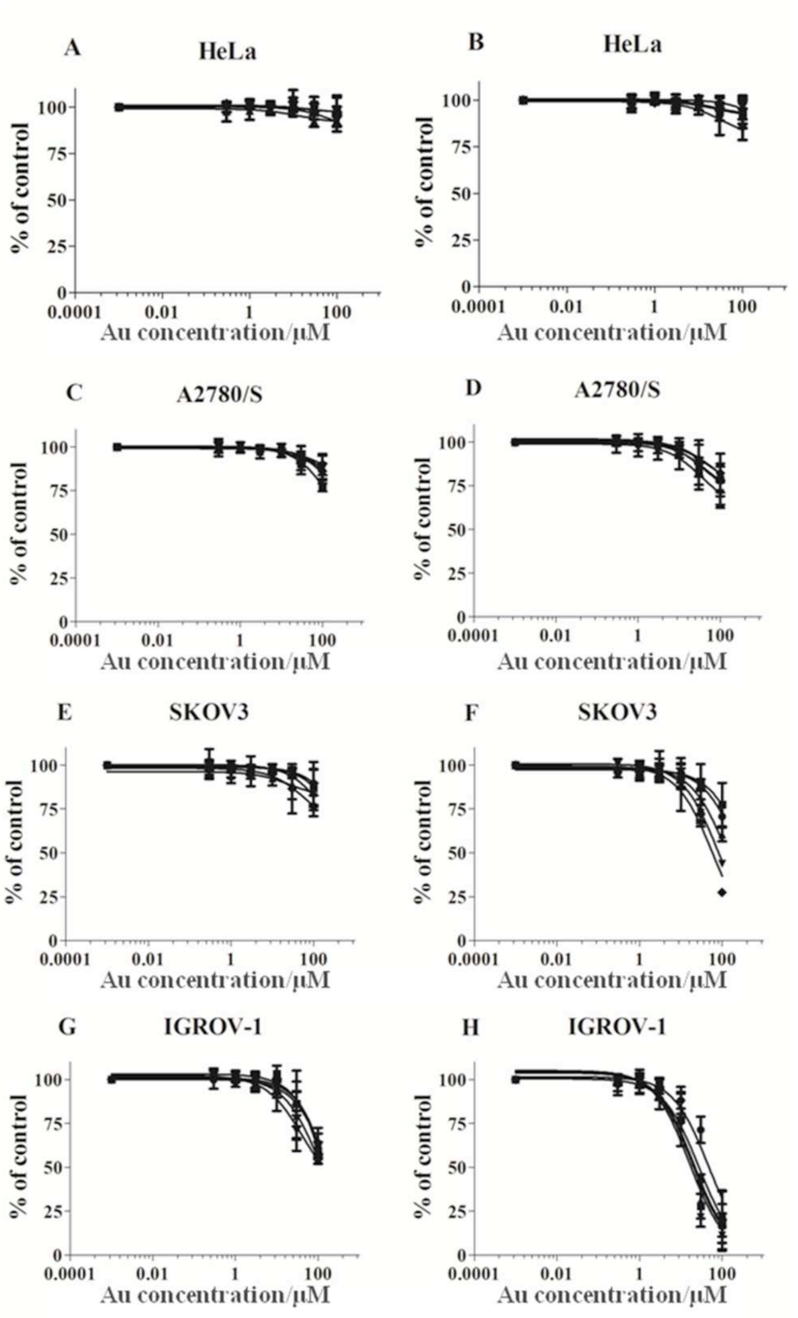

Figure 4. Cytotoxic effects of 5 different suspensions of PEG-GNRs on cell growth of HeLa, A2780/S, SKOV3 and IGROV-1 cell lines after 72 h (panels A, C, E, G) and 168 h (panels B, D, F, H) exposure. The figure shows values for GNRs 9 (●), 3 (■), 1 (▲), 1/3 (▼), 1/9 (♦).

- After 168 h exposure, the IC50 threshold was not reached in HeLa and A2780/S cells. In this case, at 100 µM Au, the inhibitory growth effects on HeLa and A2780/S cells ranged from 1.8 to 15.8% and from 17.7 to 29.3%, respectively with irrelevant dependence on particle size.

  A similar behaviour was also observed in SKOV3 cells treated with larger GNRs **9**, **3** and **1**: although IC50 values were not reached, the inhibitory effect at 100 µM Au was 29.4, 22.5 and 39.5% respectively. Conversely, smaller GNRs **1/3** and **1/9** gave IC50 values of 77.5 and 53.7 µM Au, respectively, indicating that in this cell line the cytotoxicity of PEG-GNRs seems to grow with miniaturization.

  All PEG-GNRs exhibited IC_{50} thresholds ranging from 10.3 µM to 41.0 µM Au against IGROV-1 cells with poor dependence on particle size.

- *Cell viability.*

  The effects of PEG-GNRs on cell viability were evaluated against four tumor cell lines (HeLa, A2780/S, SKOV3 and IGROV-1) after 24 hours exposure (Figure 5). All PEG-GNRs did not affect HeLa cells up to 100 µM Au and exhibited a moderate inhibition of cell viability only at 300 µM Au, which did not vary with particle size.

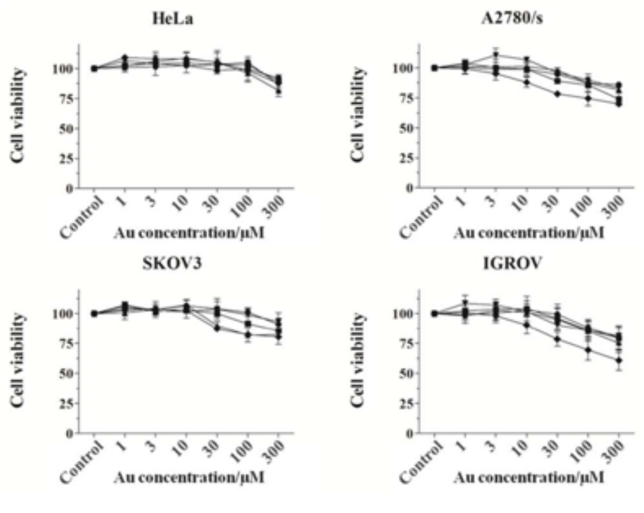

Figure 5. MTT test on HeLa, A2780/S, SKOV3 and IGROV-1 cell lines after 24 h exposure to PEG-GNRs. Cell viability is expressed as percent of MTT reduction in treated cells with respect to control cells. Reported data represents the mean ± standard deviation of three independent experiments. Figure shows values for GNRs **9 (●)**, **3 (▪)**, **1 (▲)**, **1/3 (▼)**, **1/9 (♦)**.

A2780/s and IGROV-1 cells suffered from moderate inhibition of cell viability with all particle sizes, but this effect started at lower concentrations (10 μM Au) for smaller GNRs **1/9** with respect to the others (30-100 μM Au).

The same trend was observed for SKOV3 cells. Although a different sensitivity of the various cell lines was observed, with HeLa cells holding the greatest resistance, the principal trends with particle size did not depend on cell line. Smaller particles provided slightly more MTT reduction inhibition, which falls below statistical relevance and emerged only at high gold concentrations.

- *Membrane integrity.*

Membrane stability after exposure to PEG-GNRs was assessed by fluorescence analysis of calcein efflux. Calcein-AM is a non fluorescent dye that permeates cell membranes. In live cells, intracellular esterase converts calcein-AM to green fluorescent calcein, which is unable to pass intact cell membranes. In the case of membrane integrity disruption, which may reflect multiple conditions of cell damage, a decrease in intracellular calcein fluorescence would be observed.[54] Figure 6 shows fluorescence images of A2780/s cells preloaded with calcein-AM and treated with PEG-GNRs. After 3 h exposure at 300 μM Au, none of the particles induced leakage of calcein, thus indicating the absence of membrane permeabilization. All cell lines gave similar results (Figure S4 of the SI section).

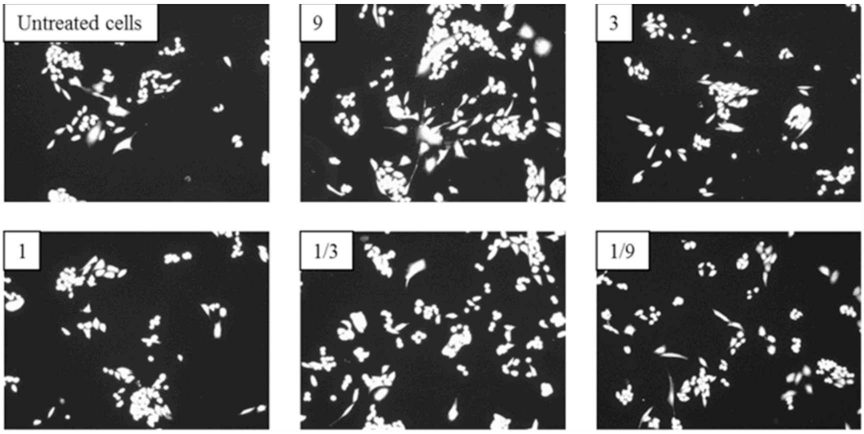

Figure 6. Calcein fluorescence in untreated A2780/S cells and after treatment with PEG-GNRs of different average size.

Blood compatibility and cellular uptake

PEG-GNRs proved to be safe for intravenous injection, without haemolytic activity nor significant detection from immune cells, especially for smaller sizes. The potential of PEG-GNRs for biomedical applications depends on their compatibility with a systemic administration. In addition, their unspecific cellular uptake may impair their potential to reach specific targets such as tumors. The effect of particle size on the haemolysis and unspecific uptake by HeLa cells taken as a standard model (Table 2) has been analyzed. Moreover, the results obtained with HeLa cells were compared with a monocyte/ macrophagic cell line (J774a.1), so as to distinguish the contribution of specific macrophage functions.

Table 2. PEG-GNRs uptake by HeLa and J774a.1 cells after different incubation times. Data are referred to the same number of cells.

	Au (ng / 10^6 cells)			
PEG-GNRs	J774a.1	HeLa		
	24 h	24 h	72 h	168 h
9	462	1178	3001	1885
3	340	/	/	/
1	209	312	1218	974
1/3	272	/	/	/
1/9	865	80	341	292

As indicated in Figure 7, none of the particles showed haemolytic activity, even at the highest concentrations. Data are referred to positive controls obtained by dosing ultrapure water to induce complete haemolysis. The effect of size on the cellular uptake of PEG-GNRs was investigated for three size classes with negligible statistical overlap (i.e. samples **1/9**, **1** and **9**, see Figure 1). The amount of gold internalized by HeLa cells exposed to 100 µM Au was evaluated at different time points. As shown in Table 2, there occurs little uptake in all samples, as it is expected for PEGylated particles and in particular GNRs. [20] As a rule of thumb, uptake grows with particle size. Table 2 also reports the values obtained with J774a.1 cells after 24 hours of incubation and shows that both smaller and bigger PEG-GNRs are internalized to a bigger extent than those of an intermediate size.

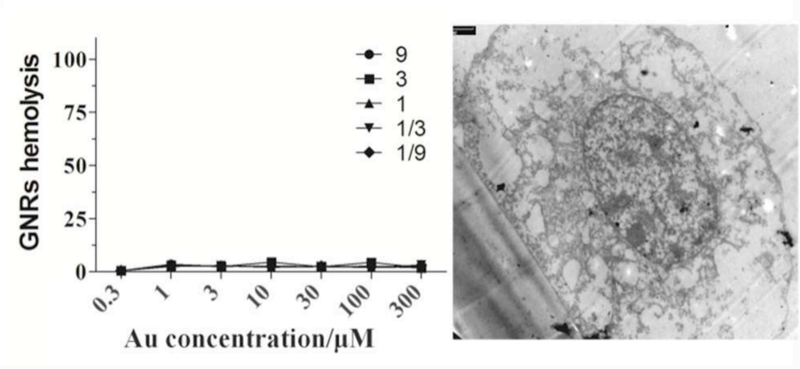

Figure 8. Left: red blood cells haemolysis from PEG-GNRs of different average size: data represent a mean of two independent experiments, both performed in triplicate, and haemolysis values are expressed as percentage of positive control. Right: representative transmission electron micrograph displaying a J774a.1 cell cultured on a transwell membrane and treated with PEG-GNRs **1**.

The impact of PEG-GNRs on macrophages was also addressed by the analysis of TEM images of J774a.1 cells treated with sample 1 and prepared with a method that is most representative of the living structure. In Figure 8, the cell morphology clearly shows the absence of alterations. No particles were detected within the cell nucleus or cytoplasm but in sporadic endocytic vesicles, indicating the rarity of unspecific internalization.

3. Discussion

In this article, different size classes of PEG-GNRs, which fall in a range suitable for biomedical applications of principal interest such as photoacoustic imaging and optical hyperthermia of cancer, different size classes. All PEG-GNRs are stable in PBS and their size does not modulate their interaction with proteins, which is very weak as it is seen in the case of cyt c. The data obtained with BSA are of particular relevance when considering PEG-GNRs for intravenous injection, albumin being the most abundant protein in the plasma. Conversely, the cell medium RPMI causes a significant red-shift of the plasmonic bands of all PEG-GNRs, although without evident precipitation. It is possible that the different components of RPMI may cooperate to modify the microenvironment of the particles, inducing a partial substitution of their PEG portion and protein adsorption. However, the extent of red-shift that was observed did not preclude the particle capacity to interact with light. In another set of experiments, the cytotoxic effects of PEG-GNRs on four tumor cell lines have been studied. Inhibitory growth effects occurred only at the highest gold concentrations and after prolonged exposures, as long as one week, when structural modifications such as those seen in RPMI may intervene. Available literature data are limited to shorter exposures (i.e. 24 or 48 hours).[54,55] A modulation of the cytotoxic effects in four cell lines suggests that the sensitivity to PEG-GNRs varies from model to model and is especially low for HeLa cells. Although HeLa cells are the most popular choice to compare the cytotoxicity of particles with different size and surface chemistry,[56] our evidence indicates that the inspection of additional cell lines and longer exposures can unveil new effects.

The cytotoxicity observed at high concentrations and long incubation times may reflect the presence of contaminants on the particle surface, such as CTAB and silver.[58] While the identification of CTAB fell below the detection capabilities of common analytic methods, the relative amount of silver was assessed by elemental analysis (Figure S5 of the SI section). This measurement confirmed that the silver content is higher for smaller particles, which reflects their larger specific surface area. Moreover, in HeLa cells, the trend of cellular uptake with particle size is opposite to the weak one observed for growth inhibition. In combination with the lack of plasmatic membrane permeabilization, these data refute any simple correlation between particle contact and cytotoxicity, which is more likely to depend on the release of silver ions and other contaminants retained on the particle surface.

In other words, the higher content of contaminants in smaller PEG-GNRs seems to over counteract the effect of a lower cellular uptake in the final cytotoxicity. An accurate quantification of the release of CTAB and silver ions into the cellular media will be the focus of future efforts. Notably, according to Figure S5 of the SI, a suspension containing 100 µM Au also comprises a total content of silver ranging between 0.6-1.6 ppm only, which is in the order of the sensitivity of our elemental analysis. The resultant release of silver ions falls below our current detection limits.

In the last set of experiments two parameters that are crucial for the use of PEG-GNRs in biomedical applications requiring their intravenous administration have been considered. Alkilany et al. reported that blood vessels are not damaged by an exposure to PEG-GNRs. [58]

Here, the absence of haemolysis and rarity of unspecific cellular uptake of PEG-GNRs is demonstrated. The latter grows with particle size. Previous studies reported a higher uptake for smaller particles.[18,24,31] However those studies extended the range of particle sizes much below our GNRs **1/9**, which we did not take into consideration because of their poor plasmonic behaviour and lack of synthetic methods. Other studies reported that the uptake of gold nanospheres displays a maximum for radii around 25 nm. [21,25] These PEG-GNRs with equivalent radii ranging from 5 to 20 nm seem to fit in the positive slope of that curve, even though the comparison of spherical and cylindrical particles requires some caution. [20] These considerations hold for those cells that do not exhibit specific phagocytic functions or conditions such as our HeLa cells. A macrophagic cell line was also considered, in order to model the uptake that may follow from systemic administration by the mononuclear phagocyte system. In this case, a different trend for smaller particles, which is ascribed to a phagocytic activity, was found.

4. Conclusions

In conclusion, PEG-GNRs are a stable platform for applications in biomedical optics. Their shape governs the frequency of their plasmonic resonances. Instead their size can be engineered to optimize the interface with an optical excitation and a biological environment for specific uses. Here we focused on the relationships between particle size and some biological profiles.

Modest PEG-GNRs cytotoxicity appears only at concentrations above 100 µM Au and after several days of incubation. This toxicity does not vary much with particle size. However some differences may arise from the larger specific surface area of smaller particles, which we associate with some contamination originating from the particle synthesis. Acute effects, such as membrane permeabilization and haemolysis, were not observed for any particle size. Data are coherent within different cell lines and toxicity tests, even though some models and parameters are more sensitive than others.

Future efforts should focus on the removal of contaminants from PEG-GNRs without destabilizing the PEG coating. The cellular uptake of PEG-GNRs is low and displays some modulation with particle size. Larger particles (say 85 nm length by 21 nm diameter) may be convenient for those contexts that require unspecific uptake, such as for loading of cellular vehicles,[55,56] while average particles (say 41 nm length by 10 nm diameter) may be ideal to inhibit unspecific uptake and pursue slower blood clearance or specificity by the addition of ligands. All this evidence, together with the absence of interactions with albumin, which is the most abundant protein in the plasma, suggests that PEG-GNRs are compatible with blood injection. In essence, particle size does not overturn the safety and blood compatibility of PEGylated GNRs in their range of greatest biomedical interest, but may still provide alternatives for a fine modulation of functional biological profiles.

5. Experimental section

Materials

Sodium borohydride, cetyltrimethylammonium bromide (CTAB), chloroauric acid, silver nitrate, ascorbic acid, alpha methoxy omega mercapto polyethylene glycol (MW 5000), polysorbate 20, sulforhodamine B and all chemicals for the various buffer solutions were obtained from Sigma Aldrich and used as received. Cell culture media (RPMI1640, DMEM and F12), fetal calf serum and antibiotics (penicillin, streptomycin) were purchased from Gibco. The water for particle synthesis was ultrapure.

Synthesis of PEGylated gold nanorods

Gold nanorods were synthesised at 25°C. A seed suspension was prepared by rapid injection of ice-cold 10 mM aqueous sodium borohydride into a solution containing 100 mM CTAB and 240 µM chloroauric acid until a final concentration of 560 µM sodium borohydride. This suspension was left under vigorous agitation for 10 min and then at rest for another 2 hours before rapid addition into a growth solution in different amounts. Meanwhile 500 ml growth solution were prepared with 100 mM CTAB, 470 µM chloroauric acid, 92 µM silver nitrate and 520 µM ascorbic acid. This solution was divided into five aliquots with a volume of 100 ml each, before injection of 1.8 (particle sample **1/9**), 0.59 (**1/3**), 0.20 (**1**), 0.066 (**3**) or 0.022 ml (**9**) seed suspension (for particle size1/9 see also Chapter 1). After 24 hours, 100 mM aqueous ascorbic acid was added until a total content of 710 µM ascorbic acid, which served to complete the metal reduction. [9,61] After two cycles of centrifugation and decantation, particles were transferred at a rate of 1.9 mM Au into an acetate buffer at pH 5 containing 500 µM CTAB and 50 µM alpha methoxy omega mercapto PEG (MW 5000). The PEGylation was left to develop at 37°C for two hours, before centrifugation, decantation and resuspension in 1% (v/v) aqueous polysorbate 20. This suspension was left at rest for 2 hours at 37°C, in an attempt to extract possible contaminants. Finally, PEG-GNRs were transferred at a rate of 4.0 mM Au into sterile PBS after purification by four cycles of centrifugation and decantation with a dead volume ratio of ~ 1 / 200.

Stability of PEGylated gold nano rods

Spectrophotometric studies were performed by a Jasco V-560 spectrophotometer. Optical extinction spectra were recorded after dilution of PEG-GNRs either in PBS or RPMI at physiological pH. The final gold concentration in the various suspensions was 100 µM. Spectra of PEG-GNRs in PBS were recorded before and after addition of 10 µM BSA, lysozyme and cyt c. All spectra were collected over 168 h both at room temperature and at 37°C. In order to achieve additional evidence of possible interactions between PEG-GNRs and proteins in a representative case, 10 µM cyt c was incubated with 100 µM Au PEG-GNRs **1** in PBS at 37°C. After 24 hours, the sample was separated by centrifugation at 10000 rpm for 13 min, the supernatant was collected and the pellet was suspended in PBS. Both components were analyzed by a Varian Cary 50 Bio UV/Vis spectrophotometer.

Cell growth and viability

All cellular lines were maintained under standard conditions as described in the SI section. For cell growth and viability studies, cells were inoculated into 96-well microplates. After 24 h, the medium was replaced with fresh medium containing PEG-GNRs. The inhibition of cell growth was studied on SKOV3, IGROV-1, A2780/S and HeLa cells, according to the sulforhodamine B (SRB) assay described by Skehan et al.[62] SRB assay was performed after 72 and 168 h of incubation with PEG-GNRs. For cell viability evaluation, the 3-(4,5-Dimethylthiazol-2-yl)-2,5-diphenyltetrazolium bromide (MTT) [63] test was conducted after 24 h of exposure to PEG-GNRs. More detail for cell growth and viability studies is given in the supporting information section.

Cell membrane permeability

To assess membrane integrity disruption, after cell inoculation, the microtiter plates were incubated under standard culture conditions for 24 h and then treated with 2.0 µM calcein-AM for 20 min. Then, the medium was replaced with fresh medium containing PEG-GNRs with 300 µM Au for 3 h. After treatment, cells were extensively washed with PBS and imaged using a Leica DMI3000B inverted microscope.

Haemolysis

For the evaluation of haemolysis, informed signed consent was obtained and human whole blood was collected from healthy volunteers. EDTA (1.8 mg/ml)-containing test tubes were used to collect the whole blood, which was centrifuged at 3000 rpm for 20 min. The buffy coat was collected, washed and diluted with normal saline to a 50% hematocrit. 100 µl of these samples were added to 3 ml of normal saline (negative control), ultrapure water (positive control) and PEG-GNRs suspensions in PBS at different concentrations. All samples were incubated at 37°C for 1 h and haemolysis was stopped by the addition of 50 µl of 2.5% glutaraldehyde prior to centrifugation at 3000 rpm for 15 min. Supernatants were collected in 96-well microplates and their absorbance at 405 nm was measured using an automated plate reader.

Particle composition and cellular uptake by elemental analysis

The determination of gold and silver concentrations in the particles was performed in triplicate by a Varian 720-ES Inductively Coupled Plasma Atomic Emission Spectrometer (ICP-AES).[64] Before analysis, 10 µl suspension of PEG-GNRs in PBS were digested in PE vials by heating at 80°C for 24 hours with 1 ml aqua regia (HCl suprapure grade and HNO_3 sub-boiled in 3:1 ratio). HeLa cells and J774a.1 cells that had been exposed to PEG-GNRs were digested by heating at 80°C for 24 hours with 1 ml aqua regia and 100 µl H_2O_2 suprapure grade. After digestion, samples were diluted to 5 ml with ultrapure water, spiked with 4 ppm Ge used as internal standard and analyzed. Wavelengths used for Ag, Au and Ge were 328.068, 242.794 and 209.426 nm, respectively. Between samples, a rinse solution containing 2% v/v HNO_3 was used.

Cellular uptake by electron microscopy

J774a.1 cells were seeded onto transwell membranes and treated overnight with PEG-GNRs. Cells were then washed and fixed with paraformaldehyde (3,6%, 5 min at room temperature). Samples were washed with fresh PBS and membranes were cut in triangles, post-fixed in 1% osmium tetroxide in PBS at 4°C for 2 h, washed again, dehydrated in a graded series of ethanol at room temperature and incubated in propylene oxide (twice, 30 min each time). Samples were then incubated in 1:1 mixture of propylene oxide and Spurr resin for 24 h at room temperature, next in 1:2 mixture for 1 h at room temperature and finally in pure resin for 1 h at room temperature, 1 h at 45°C and 24 h at 70°C. After sectioning and staining with uranyl acetate for 1 h at room temperature, slices were washed and inspected with a Philips CM12 transmission electron microscope.

6. Supporting Informations

Supplementary Methods

- *Cell lines and culture conditions*

For cellular studies, three human ovarian tumor cell lines (SKOV3, IGROV-1 and A2780/S), one human cervix carcinoma cell line (HeLa) and one murine monocytic/ macrophagic cell line (J774a.1) were used. A2780/S and IGROV-1 cell lines were maintained in RPMI1640 medium, HeLa and J774a.1 cell lines in DMEM medium and SKOV-3 cell line in F-12 medium. All cell lines were supplemented with fetal bovine serum, 100 units/mL penicillin, and 100 μg/mL streptomycin and maintained under standard culture conditions (37°C, 5% CO_2, 95% air and 100% relative humidity).

- *Cell growth inhibition studies*

The cytotoxic effects of five different GNRs samples (1/9, 1/3, 1, 3 and 9) were evaluated against SKOV3, IGROV-1, A2780/S and HeLa, according to the sulforhodamine B (SRB) assay described by Skehan et al.[36]. Exponentially growing cells were inoculated into 96-well microplates at specific plating density/well (range 1 – 5 × 103) according to the various types of cell lines. After 24 h, the medium was replaced with fresh medium containing PEG-GNRs for exposure times of 72 and 168 h. Gold concentrations in the different suspensions ranged from 0.003 to 100 μM. Cells were then fixed in situ by 10% trichloroacetic acid (TCA) and stained by SRB solution at 0.4% (w/v) in 1% acetic acid. After staining, unbound dye was removed by washing five times with 1% acetic acid and the plates were air dried. Bound stain was subsequently solubilized with 10 mM tris base and its absorbance was read on an automated plate reader at a wavelength of 540 nm. The IC50 gold concentration resulting in a 50% reduction in the net protein content in cells treated with particles as compared to controls was determined after 72 or 168 h particle exposures. The IC50 data represent the mean of at least three independent experiments.

- *Cell viability studies*

Exponentially growing cells were inoculated into 96-well microplates and maintained under standard culture conditions for 24 h. Thereafter, the medium was replaced with fresh medium containing different concentrations of PEG-GNRs. After 24 h, the MTT reduction assay described by Mosmann [41] was performed: cells were incubated with a

0.5 mg/ml MTT solution at 37°C for 4 h and then with cell lysis buffer (20% SDS, 50% N,Ndimethylformamide, pH 4.7) for 3 h. The absorbance values of blue formazan were determined at 590 nm by an automated plate reader.

Supplementary data

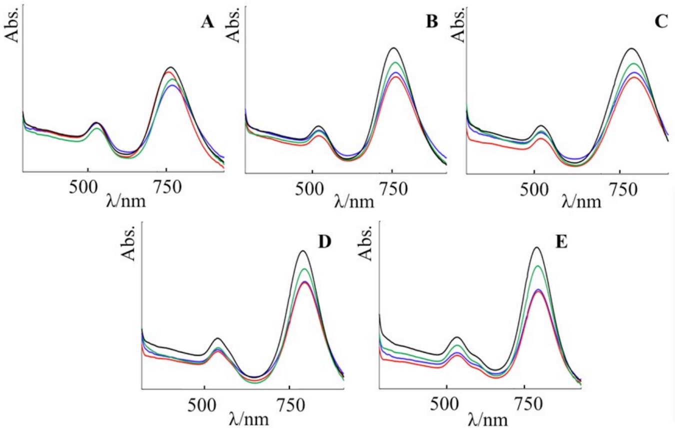

Figure S1. Stability of PEGylated gold nanorods with lysozyme. Absorption spectra of five sizes of PEG-GNRs in PBS with lysozyme. A) GNRs **1/9**; B) **1/3**; C) **1**; D) **3**; E) **9**. The figure shows spectra recorded at time zero (black line) and after 1 h (green line), 24 h (red line) and 168 h (blue line).

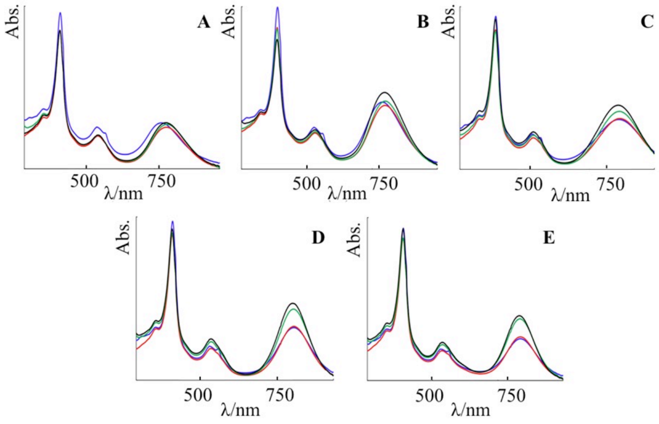

Figure S2. Stability of PEGylated gold nanorods with cyt c. Absorption spectra of five sizes of PEG-GNRs in PBS with cyt c. A) GNRs **1/9**; B) **1/3**; C) **1**; D) **3**; E) **9**. The figure shows spectra recorded at time zero (black line) and after 1 h (green line), 24 h (red line) and 168 h (blue line).

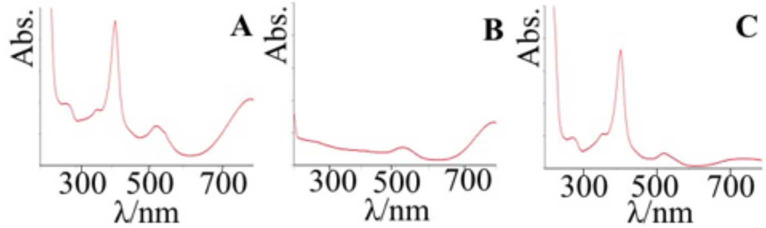

Figure S3. Interaction of PEGylated gold nanorods with cyt c. Absorption spectra of PEG-GNRs **1** with cyt c incubated for 24 h at 37°C (A) and after centrifugation and washing (B). Supernatant obtained after the first washing cycle (C).

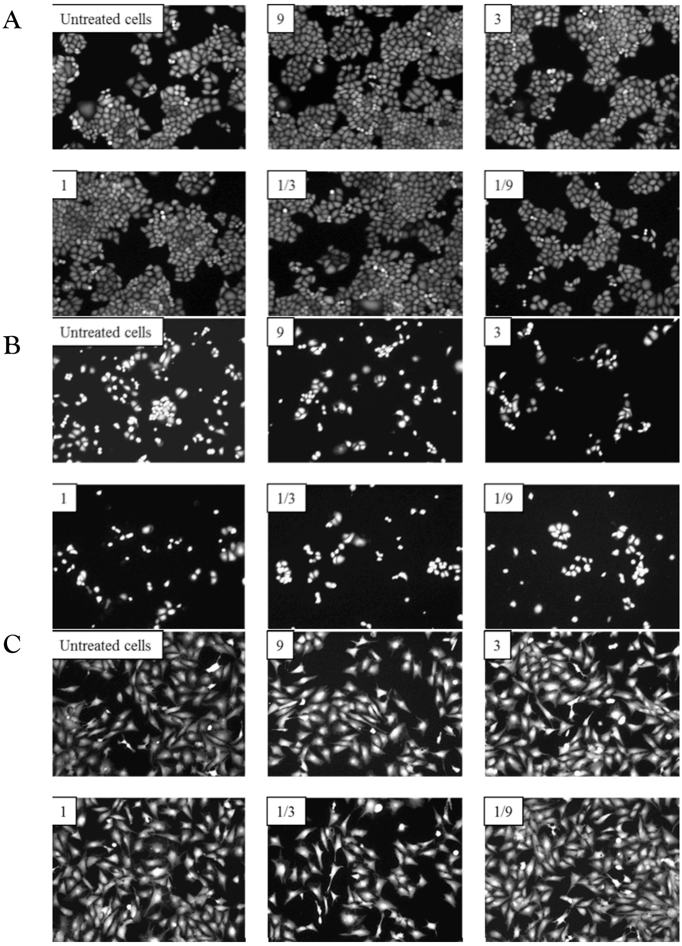

Figure S4. Membrane integrity. Calcein fluorescence in HeLa (A), IGROV (B) and SKOV3 (C) untreated cells and after treatment with PEG-GNRs of different sizes. All samples exhibit no release of calcein after treatment with GNRs, indicating that the membrane integrity has not been altered.

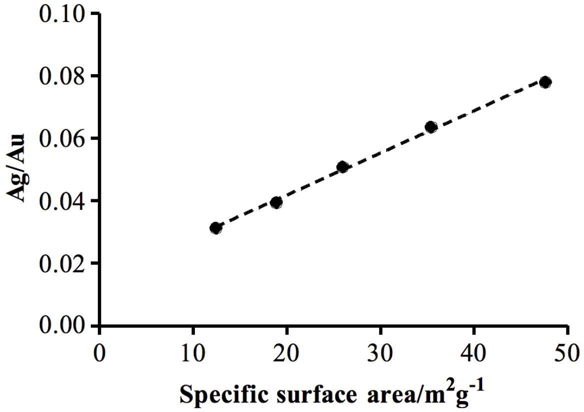

Figure S5. Particle composition by elemental analysis. Ratio between Ag and Au among the different sizes of PEG-GNRs.

Acknowledgments

This work has been partially supported by the Projects of the Health Board of the Tuscan Region "NANOTREAT" and "NANO-CHROM". Francesco Rugi is gratefully acknowledged for the ICP-AES measurements. Chiara Gabbiani is also acknowledged for her work in the first stage of the project.

References

[1] 1. K. Huang, P.K. Jain, I.H. El-Sayed and M.A. El-Sayed, Nanomed. 2 (2007) 681.
[2] X. Huang, P.K. Jain, I.H. El-Sayed and M.A. El-Sayed, Lasers Med. Sci. 23 (2008) 217.
[3] L. Tong, Q. Wei, A. Wie and J.X. Cheng, Photochem. Photobiol. 85 (2009) 21.
[4] I.H. El-Sayed, Curr. Oncol. Rep. 12 (2010) 121.
[5] F. Ratto, P. Matteini, S. Centi, F. Rossi and R. Pini, J. Biophotonics 4 (2011) 64.
[6] A.M. Alkilany and C.J. Murphy, J. Nanopart. Res. 12 (2010) 2313.
[7] N. Khlebtsov and L. Dykman, Chem. Soc. Rev., 40 (2011) 1647.
[8] H. Chen, L. Shao, Q. Li, J. Wang, Chem. Soc. Rev. 42 (2013) 2679.
[9] F. Ratto, P. Matteini, A. Cini, S. Centi, F. Rossi, F. Fusi and R. Pini, J Nanopart. Res. 13 (2011) 4337.
[10] J. Perez-Juste, I. Pastoriza-Santos, L.M. Liz-Marzan and P. Mulvaney, Coord. Chem. Rev., 249 (2005) 1870.
[11] P.K. Jain, K.S. Lee, I.H. El-Sayed and M.A. El- Sayed, J. Phys. Chem. B 110 (2006) 7238.

[12] P.K. Jain and M.A. El-Sayed, Chem. Phys. Lett. 487 (2010) 153.

[13] M. Eghtedari, A. Oraevsky, J. A. Copland, N. A. Kotov, A. Conjusteau, M. Motamedi, Nano Lett. 7 (2007)1914.

[14] L. Tong, Y. Zhao, T.B. Huff, M. N. Hansen, A. Wei, J. X. Cheng, Adv. Mater. 19 (2007) 3136.

[15] A. Kopwitthaya, K.T. Yong, R. Hu, I. Roy, H. Ding, L.A. Vathy, E.J. Bergey and P.N. Prasad, Nanotechnol,21 (2010) 315101.

[16] R.G. Rayavarapu, W. Petersen, L. Hartsuiker, P. Chin, H. Janssen, F.W. van Leeuwen, C. Otto, S. Manohar and T.G. van Leeuwen, Nanotechnol. 21 (2010) 145101.

[17] C. Grabinski, N. Schaeublin, A. Wijaya, H. D'Couto, S.H. Baxamusa, J. Hamad-Schifferli and S.M. Hussain, ACS Nano, 5 (2011) 2870.

[18] T. Mironava, M. Hadjiargyrou, M. Simon, V. Jurukovski and M.H. Rafailovich, Nanotoxicology 4 (2010) 120.

[19] C. Freese, M.I. Gibson, H.A. Klok, R.E. Unger and C.J. Kirkpatrick, Biomacromolecules, 13 (2012)1533.

[20] E. Oh, J.B. Delehanty, K.E. Sapsford, K. Susumu, R. Goswami, J.B. Blanco-Canosa, P.E. Dawson, J. Granek, M. Shoff, Q. Zhang, P.L. Goering, A. Huston and I.L. Medintz, ACS Nano, 5 (2011) 6434.

[21] X.D. Zhang, D. Wu, X. Shen, P.X. Liu, N. Yang, B. Zhao, H. Zhang, Y.M. Sun, L.A. Zhang, F.Y. Fan, Int. J. Nanomed. 6 (2011) 2071.

[22] P. Matteini, F. Ratto, F. Rossi and R. Pini, J. Biomed. Opt. 17 (2012) 010701.

[23] B.D. Chithrani, A.A. Ghazani, W.C. Chan, Nano Lett. 6 (2006) 662.

[24] C.D. Walkey, J.B. Olsen, H. Guo, A. Emili and W.C. Chan, J. Am. Chem. Soc. 134 (2012) 2139.

[25] S. Chakraborty, P. Joshi, V. Shanker, Z.A. Ansari, S.P. Singh and P. Chakrabarti, Langmuir, 27 (2011) 7722.

[26] W. S. Cho, S. Kim, B.S. Han, W.C. Son and J. Jeong, Toxicol. Lett. 191 (2009) 96.

[27] M.A. Abdelhalim, Lipids Health Dis. 205 (2011) 205.

[28] L.S. Rieznichenko, S.M. Dybkova, T.G. Gruzina, Z.R. Ulberg, I.N. Todor, N.Y. Lukyanova, S.I. Shpyleva, V.F. Chekhun, Exp. Oncol. 34 (2012) 25.

[29] M. Schulz, L. Ma-Hock, S. Brill, V. Strauss, S. Treumann, S. Gröters, B. van Ravenzwaay and R. Landsiedel, Mutat. Res. 745 (2012) 51.

[30] G. Vecchio, A. Galeone, V. Brunetti, G. Maiorano, S. Sabella, R. Cingolani and P.P. Pompa, PLoS One 7 (2012) e29980.

[31] T. Niidome, M. Yamagata, Y. Okamoto, Y. Akiyama, H. Takahashi, T. Kawano, Y. Katayama, Y. Niidome, J. Control. Release 114 (2006) 343.

[32] I.P. Lau, H. Chen, J. Wang, H.C. Ong, K.G. Leung, H.P. Ho, and S.K. Kong, Nanotoxicology 6 (2011) 847.

[33] A.M. Alkilany, L.B. Thompson, S.P. Boulos, P.N. Sisco and C.J. Murphy, Adv. Drug. Deliv. Rev. 64 (2012) 190.

[34] W.S. Cho, M. Cho, J. Jeong, M. Choi, H.Y. Cho, B.S. Han, S.H. Kim, H.O. Kim, Y.T. Lim, B.H. Chung, J. Jeong, Toxicol. Appl. Pharmacol. 236 (2009) 16.

[35] E.B. Dickerson, E.C. Dreaden, X. Huang, I.H. El-Sayed, H. Chu, S. Pushpanketh, J.F. McDonald, M.A. El-Sayed, Cancer Lett. 269 (2008) 57.

[36] G. von Maltzahn, J.H. Park, A. Agrawal, N.K. Bandaru, S.K. Das, M.J. Sailor, S.N. Bhatia, Cancer Res. 69 (2009) 3892.

[37] W.I. Choi, J.Y. Kim, C. Kang, C.C. Byeon, Y.H. Kim, G. Tae, ACS Nano 5 (2011) 1995.

[38] A.F. Bagley, S. Hill, G.S. Rogers, S.N. Bhatia, ACS Nano 7 (2013) 8089.

[39] F. Ratto, P. Matteini, F. Rossi and R. Pini, J. Nanopart. Res. (2010) 2029.

[40] B. Nikoobakht and M.A. El-Sayed, Chem. Mater., 2003, 15, 1957-62.

[41] L. Cavigli, M. de Angelis, F. Ratto, P. Matteini, F. Rossi, S. Centi, F. Fusi and R. Pini, J. Phys. Chem. C, (2014)

[42] R. Mercatelli, G. Romano, F. Ratto, P. Matteini, S. Centi, F. Cialdai, M. Monici, R. Pini, F. Fusi, Appl. Phys. Lett., 2011, 99, 131113.

[43] X.D. Xu and M.B. Cortie, Adv. Funct. Mat. 2006, 16, 2170.

[44] A. Wijaya, K. Hamad-Schifferli, Langmuir 24 (2008) 9966.

[45] O. Garbuzenko, Y. Barenholz, A. Priev. Chem. Phys. Lipids 135 (2005) 117.

[46] S. Link and M.A. El Sayed, Int. Rev. Phys. Chem., 2000, 19, 409-53.

[47] G.S. Terentyuk, G.N. Maslyakova, L.V. Suleymanova, B.N. Khlebtsov, B.Y. Kogan, G.G. Akchurin, A.V. Shantrocha, I.L. Maksimova, N.G. Khlebtsov and V.V. Tuchin, J. Biophotonics, 2 (2009) 292.

[48] S. Chakraborty, P. Joshi, Z. A. Ansari, S. P. Singh, P. Chakrabarti, Langmuir 27 (2011) 7722.

[49] M. Iosin, F. Toderas, P.L. Baldeck, S. Astilean, J. Mol. Struct., 2009, 196, 924–6.

[50] K. Saha, A. Bajaj, B. Duncan and V.M. Rotello, Small, 2011, 7, 1903- 18.

[51] L. Wang, E. santos, D. Schenk, M. Rabago-Smith, Antioxidants 3 (2014) 559.

[52] C. Li, C. Wu, J. Zheng, J. Lai, C. Zhang and Y. Zhao, Langmuir, 2010, 26, 9130-5.

[53] J.C. Bischof, J. Padanilam, W.H. Holmes, R.M. Ezzell, R.C. Lee, R.G. Tompkins, M.L. Yarmush and M. Toner, Biophys. J., 1995, 68, 2608-14.

[54] M. Mahmood, D.A. Casciano, T. Mocan, C. Iancu, Y. Xu, L. Mocan, D.T. Iancu, E. Dervishi, Z. Li, M. Abdalmuhsen, A.R. Biris, N. Ali, P. Howard and A.S. Biris, J. Appl. Toxicol., 30 (2010)74.

[55] W. Cui, J. Li, Y. Zhang, H. Rong, W. Lu and L. Jiang, Nanomed. 8 (2012) 46.

[56] Y. Pan, S. Neuss, A. Leifert, M. Fischler, F. Wen, U. Simon, G. Schmid, W. Brandau and W. Jahnen-Dechent, Small 3 (2007) 1941.

[57] A.M. Alkilany, P.N. Nagaria, C.R. Hexel, T.J. Shaw, C.J. Murphy, M.D. Wyatt, Small (2009) 701.

[58] A.M. Alkilany, A. Shatanawi, T. Kurtz, R.B. Caldwell, R.W. Caldwell, Small 8 (2012) 1270.

[59] S.K. Baek, A.R. Makkouk, T. Krasieva, C.H. Sun, S.J. Madsen and H. Hirschberg, J. Neurooncol. 104 (2011) 439.

[60] S.J. Madsen, S.K. Baek, A.R. Makkouk, T. Krasieva and H. Hirschberg, Ann. Biomed. Eng., 40 (2012) 507.
[61] L. Cavigli, M. de Angelis, F. Ratto, P. Matteini, F. Rossi, S. Centi, F. Fusi and R. Pini, J. Phys. Chem. C 2014.
[62] P. Skekan, R. Stroreng, D. Scudiero, A. Monks, J. Mcmahon, D. Vistica, J.T. Warren, H. Bokesch, S. Kenney, M.R. Boyd, J. Natl. Cancer Inst. 82 (1990) 1107.
[63] T. Mosmann, J. Immunol. Methods 65 (1983) 55.
[64] E. Fantechi, G. Campo, D. Carta, A. Corrias, C. de Julián Fernández, D. Gatteschi, C. Innocenti, F. Pineider, F. Rugi and C. Sangregorio, J. Phys. Chem. C 116 (2012) 8261.

Chapter 4

Tuning the Interactions of Gold Nanorods with Proteins through Functionalization

Tuning the Interactions of Gold Nanorods with Proteins through Functionalization*

* *F. Scaletti**, A. Feis, S. Centi, R. Pini, V. M. Rotello, L. Messori, Tuning the interactions of PEG-coated gold nanorods with BSA and model proteins through insertion of amino or carboxylate groups. J. Inorg. Biochem. (2015) In Press.*

**Corresponding Author*

Graphical abstract

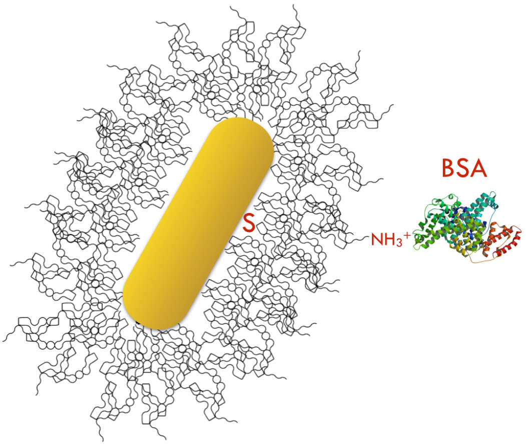

1. Introduction

Gold nanorods (GNRs) feature unique and useful optical properties that are highly dependent on size and aspect ratio [1-5]. While gold nanospheres absorb mainly in the visible region, the localized surface plasmon resonance (LSPR) band of GNRs splits into an extinction band in the visible region (due to the transverse plasmon excitation) and a second intense band in the vis-NIR region (due to the longitudinal excitation), whose position depends critically on the aspect ratio of the particle [6]. These strong absorptions open a range of biomedical applications in diagnosis [7,8] and therapy (i.e. drug delivery [9] and photothermal therapy [10-12]). In particular, the unique optical properties of GNRs make them suitable platforms for sensing applications [13,14].

Specifically, the longitudinal component of the GNR LSPR band is highly sensitive to changes in the refractive index of the immediate environment of the GNRs [15,16]. Several examples demonstrate how GNRs can be used for biosensing through conjugation with biological receptors. Chen et al. [17] and Nusz et al. [18] report the use of GNRs functionalized with biotin molecules for the quantitative detection of streptavidin through monitoring the spectral wavelength shift of the longitudinal LSPR. GNRs modified with antibodies for the detection of specific antigens were likewise used for the multiplex biosensing [19]. Several studies have explored the interactions of gold nanoparticles [20-22] and nanorods with proteins [23–25] and revealed how the nature of the coating is critical to modulate the interface between particles and biomolecules [26-29]. This control enables the attachment of additional functional molecules such as ligands for biochemical targets of interest [10] and enhances the stability of the particles within culture media and body fluids [24].

The use of GNRs for both sensing and delivery relies on their stability in biological fluids, avoiding deleterious aggregation and precipitation phenomena [30,31]. Studies have identified polyethylene glycol (PEG) as the coating of choice for GNRs to achieve this goal. PEG-coated GNRs manifest excellent stability and biocompatibility profiles in comparison with cetyl trimethylammonium bromide (CTAB)-capped GNRs [32,33]. Moreover, PEG-coated GNRs manifest on the whole a far lower reactivity with proteins in comparison to CTAB-coated GNRs [33,34]. We hypothesized that modification of PEG through attachment of charged groups at their termini could be used to modulate the interactions of GNRs with proteins while maintaining colloidal stability. For this reason, we prepared two types of PEG-coated GNRs bearing cationic amino (PEG-NH_3^+) or anionic carboxylate (PEG-COO^-) groups. Results showed how different functional groups on the PEG ligand can modulate the GNR–protein adducts through electrostatic interactions and the reversibility of the protein binding process to the GNRs.

2. Results and Discussion

Synthesis and characterization of PEG-coated GNRs

GNRs, of average size 5 nm × 20 nm (aspect ratio 4), were synthesized and functionalized with PEG-NH_2 (GNR-PEG-NH_2) or PEG-COOH (GNR-PEG-COOH) as described above. A TEM image of the GNRs obtained following this procedure is shown in Figure S1. UV–vis–NIR absorption spectra were recorded for the various types of GNRs in the window between 350 and 1000 nm, where two LSPR bands are observed. Surprisingly, the maxima of both plasmonic bands are superimposable for the as-synthesized GNRs (GNR-CTAB), the GNR-PEG-NH_2, and GNR-PEG-COOH (Figure S2).

Interactions of PEG-coated GNRs with proteins

The interactions of GNR-PEG-NH_2 and GNR-PEG-COOH with three proteins (hCC, HEWL and BSA) was then studied using spectrophotometric analysis. As expected, due to charge complementarity, a noticeable change occurred when BSA was added to GNR-PEG-NH_2 (Figure 1); an intensity redistribution was noticed leading to a decrease of the extinction at the original maximum and a progressive red-shift of the longitudinal LSPR. The protein-induced red-shift and asymmetry in the longitudinal LSPR bands can both be rationalized on the basis of theoretical predictions [35]. The LSPR of anisotropic nanoparticles like GNRs is especially sensitive to changes of the environment dielectric function [36,37]. Small changes, in fact, may occur upon water displacement by those protein molecules which bind at the water/ammonium PEG coating interface. This displacement will lead to an increase of the refractive index [38], and therefore to a red-shift of the longitudinal LSPR band position. The intensity redistribution, whereby the intensity of the longitudinal band is decreased and a broad extinction at longer wavelengths (> 900 nm) appears (Figure 1), indicates the formation of a considerable amount of plasmonically coupled GNR aggregates [39]. The shift to longer wavelengths is a strong indication for the prevalence of end-to-end dimers [35].

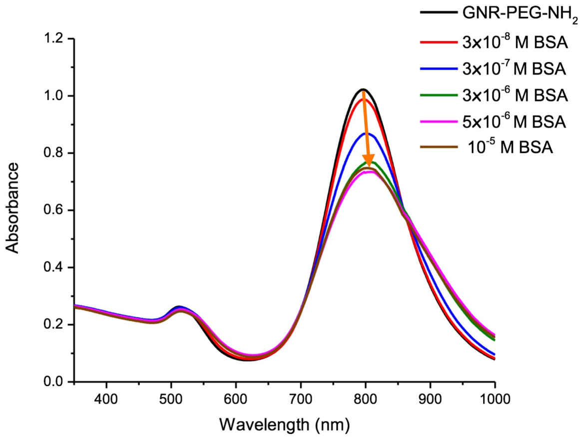

Figure 1. UV-vis-NIR spectra of GNR-PEG-NH$_2$ (15 nM) in water before and after the addition of BSA at different concentrations.

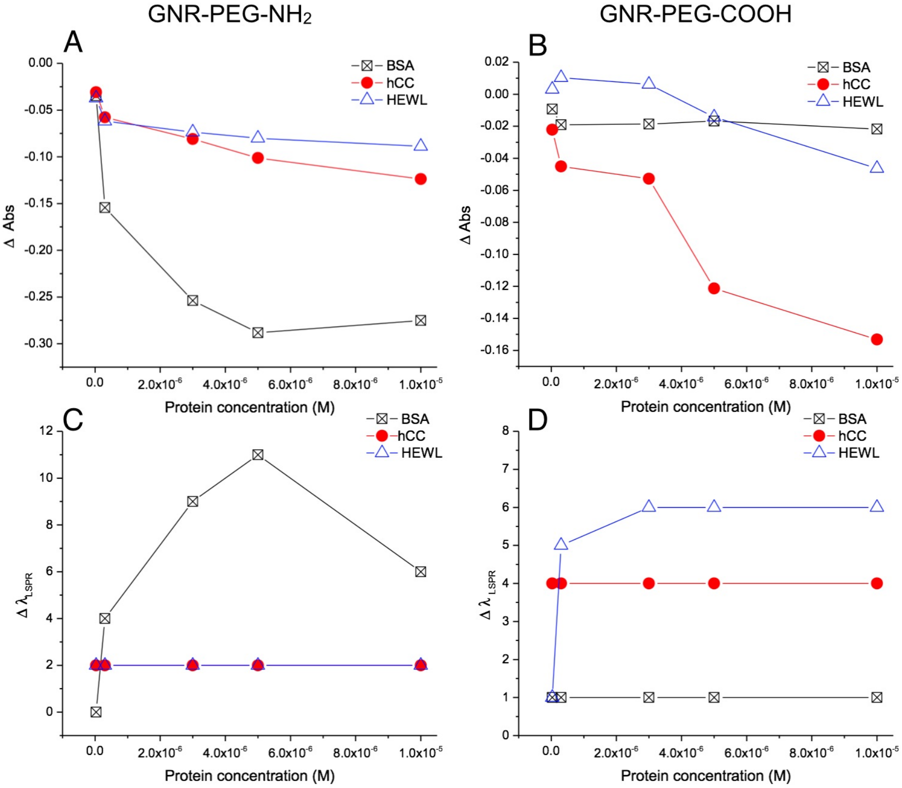

Figure 2. Plot of the extinction change (ΔAbs) measured at the maximum of the longitudinal LSPR of GNR-PEG-NH$_2$ (A) and GNR-PEG-COOH (B) and of longitudinal LSPR shift (Δλ) of GNR-PEG-NH$_2$ (C) and GNR-PEG-COOH (D) at different proteins concentration.

Figure 2 reports the spectral effects produced by addition of BSA, hCC or HEWL, showing a different behavior for the three proteins. Small changes were detected in the extinction spectra of GNR-PEG-NH_2 with increasing concentrations of cationic hCC and HEWL (Figure 2A). In particular the longitudinal LSPR shift ($\Delta\lambda$) of GNR-PEG-NH_2 did not show any differences upon interaction with both cationic proteins (Figure 2C). The intensity of the longer-wavelength band of GNR-PEG-NH_2 decreased upon addition of the two model proteins with a small red-shift. Therefore, a similar behavior can be ascribed to the interaction between GNR-PEG-NH_2 and hCC or HEWL. However, in the presence of GNR-PEG-COOH, different patterns can be assigned to the three proteins (Figure 2B and D). As expected, the interaction between GNR-PEG-COOH and BSA was negligible; only a minimal intensity decrease of the longer-wavelength band was observed when BSA was added to aqueous dispersions of GNR-PEG-COOH while hCC and HEWL showed greater spectroscopic changes. HEWL has a net positive charge under all applied experimental conditions, as its isoelectric point is 11.3. As a consequence, the interaction with GNR-PEG-COOH is favored (Figure 2B and D) whereas the extinction spectra of GNR-PEG-NH_2 are changed to a very limited extent (Figure 2A and C). Remarkably the interaction with GNR-PEG-COOH was particularly evident at low concentrations of the protein, leading to an increase of the extinction and a consistent red-shift of the longitudinal LSPR as a consequence of the alteration of the GNRs local environment and the dielectric constant of the medium [16]. At higher concentrations of HEWL a decrease of the extinction at the maximum was detected, possibly due to the formation of aggregates. The extinction changes in the presence of HEWL were not so pronounced as in the case of BSA, suggesting that the HEWL-induced GNR aggregates were less abundant and/or less ordered. The results obtained in the case of hCC were similar to those obtained with HEWL: the intensity of the longitudinal LSPR band progressively decreased—and the maximum slightly red-shifted—upon addition of hCC to GNR-PEG-COOH sample. hCC, like HEWL, is positively charged in water solution or in PB solutions at pH 7.4, its isoelectric point being about 10.5. Then hCC appeared to interact mostly with the negatively charged GNRs, leading to a larger decrease of the extinction compared to HEWL (Figure 2B and D). Similar experiments performed in 50 mM PB showed that the spectral changes were largely suppressed or attenuated for both functionalized GNRs upon addiction of HEWL (Figure S3), hCC (Figure S4) and BSA (FigureS5), as expected due to electrostatic screening effects at higher salt concentrations [40].

Effects of electrolyte addition on GNR–protein interactions

In most above cases, a clear effect of the buffer was detected. To separate pH effects from ionic strength effects, we have studied the interaction of BSA with GNR-PEG-NH_2 that produces the largest spectral variations, in the presence of a salt. Figure 3 shows the extinction changes occurring upon addition of BSA to GNR-PEG-NH_2 in a 50 mM sodium sulfate solution (Figure 3A) and after the addition of sodium sulfate to an already formed BSA/GNR-PEG-NH_2 conjugate (Figure 3B). It was apparent that the interaction was then largely inhibited by the presence of salt. In fact, as it was shown in pure water (Figure 1), both the longer-wavelength band and the shorter-wavelength one became asymmetric, leading to a decrease of the extinction and an increase on the red side of the LSPR band. In particular, an isosbestic point can be seen in Figure 1, indicating an equilibrium between two species, that are GNRs and end-to-end dimers, while in the presence of salts (Figure 3A) only a decrease in the intensity could be detected. Moreover, sodium sulfate almost completely reversed the spectral changes when it was added to an already formed BSA/GNR-PEG-NH_2 conjugate (Figure 3B).

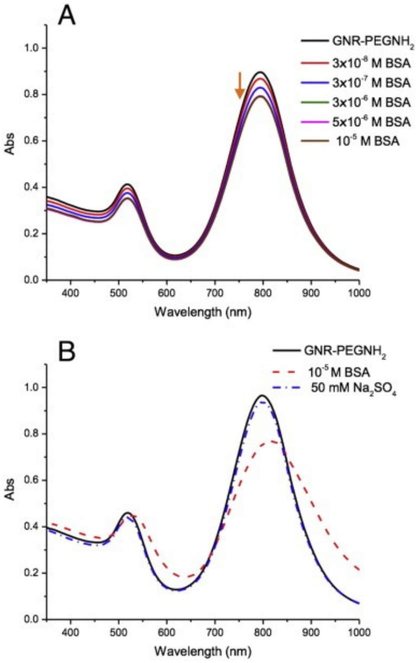

Figure 3. UV-vis-NIR spectra of GNR-PEG-NH_2 (15 nM) in 50 mM Na_2SO_4 solution in the presence of BSA at different concentrations (A) and of GNR-PEG-NH_2, in the presence of BSA 10^{-5} M and after the addition of 50 mM Na_2SO_4 (B).

Therefore, GNR-PEG-NH$_2$ can be easily separated from the adsorbed protein, indicating that any chemical bonds are formed between the gold surface and protein cysteine residues, owing to the PEG layer. These results are consistent with the recently reported distinct interactions between BSA and either positively or negatively charged GNRs [40] and demonstrate the importance of electrostatic interactions. Moreover, the observation that a small fraction of BSA is irreversibly bound, whereas most protein molecules can be displaced by the addition of sodium sulfate is compatible with the formation of both a "hard" and a "soft" protein corona [41].

DLS and CD measurements

To correlate the protein-induced GNR extinction changes with GNR size parameters, we performed DLS measurements of the most representative sample, namely, GNR-PEG-NH$_2$, upon interaction with BSA. Results are reported in Figure 4 while the hydrodynamic radius and the relative intensity of the DLS peaks are summarized in Table 1.

Table 1. Hydrodynamic diameter of GNRs-PEG-NH$_2$ and intensity percentage of DLS peaks before and after the addition of increasing concentrations of BSA

GNR-PEG-NH$_2$/ BSA	**Hydrodynamic radius ± σ (nm)**		**Intensity (%)**	
[BSA]	**Peak 1**	**Peak 2**	**Peak 1**	**Peak 2**
0	57.2 ± 20.0	1.4 ± 0.3	78.5	21.5
3×10^{-8} M	65.3 ± 29.4	1.3 ± 0.2	82.7	17.3
3×10^{-7} M	365.7 ± 84.0	--	100	--
5×10^{-6} M	591.4 ± 208.6	--	100	--
10^{-5} M	781.6 ± 304.8	--	100	--

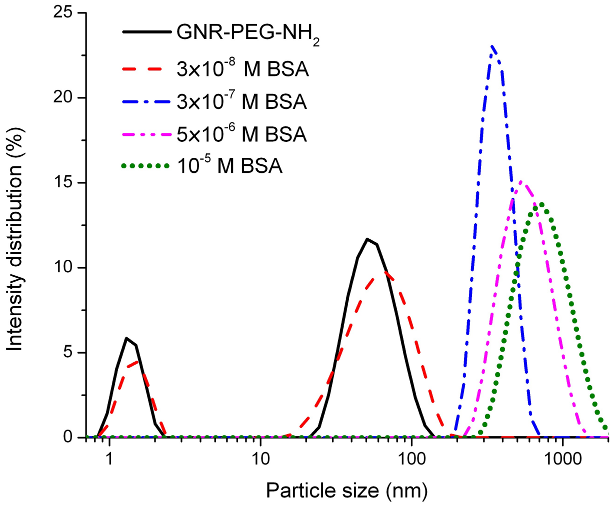

Figure 4. Size distribution curves of GNR-PEG-NH2 (15 nM) in water before and after the addition of increasing concentrations of BSA.

The size distribution diagram of GNR-PEG-NH2 in Figure 4 shows two peaks, one at 1.4 nm and the second one at 50-60 nm. According to the literature [42,43], the small size distribution peak is not an actual particle size but a representation of the rotational diffusion of nanorods while peak at 50-60 nm is the hydrodynamic diameter of GNRs. Upon addition of BSA, a progressive increase of the hydrodynamic radius of GNR-PEG-NH2 was observed (Figure 4). Moreover the relative intensity of the small size peak decreased from 21.5% to 0%, while the relative intensity of the large size peak increased from 78.5% to 100%. The increase in the hydrodynamic radius points to the progressive formation of protein layers, wrapping the GNRs, which will partly stay in their monomeric form and partly form GNR aggregates. Moreover the small size DLS peak, due to the rotational diffusion of rod-like nano-particles, disappeared upon addition of BSA beyond 5×10^{-6} M (Figure 4). This indicates that the large-sized protein/GNR aggregates, formed at high BSA concentrations, were essentially spherical, as previously observed in similar cases [43,44]. For comparison purposes, DLS measurements of GNR-PEG-COOH interacting with hCC were performed. The size distribution peaks are reported in Figure S6 and summarized in Table S2. In the case of GNRs-PEG-COOH, a significant increase of the hydrodynamic diameter could be observed only above 3×10^{-7} M protein concentration. This contrasts with the extinction results, where a small change

was observed already at 3×10^{-8} M hCC concentration. However DLS data of GNR-PEG-COOH in PB (Figure S7 and Table S3) showed a good agreement with the spectrophotometric measurements. In fact the presence of phosphate both hindered the protein-induced extinction changes, and suppressed the increase of the hydrodynamic radius that, in contrast, is clearly observed in the absence of phosphate.
Then, CD measurements were performed to determine the effect of GNR–protein interaction on the protein structure. Figure 5 compares the CD spectra—in the 200–260 nm range—of BSA at 3×10^{-7} M and 9×10^{-7} M before and after the addition of GNR-PEG-NH_2. The interaction led to an intensity decrease of the negative bands at 209 and 222 nm for the lower protein concentration (Figure 5A), whereas the CD spectra at 9×10^{-7} M protein are not changed by the presence of GNRs but for a small baseline offset (Figure 5B). This can be explained considering that the CD spectra at higher BSA molarity result from all the protein molecules, including the unbound ones and those lying in the outer layers around the GNRs. Therefore, the contribution of the unaltered BSA molecules to the measured CD will be relatively more important at higher protein concentrations and overwhelm the CD decrease due to GNR–protein interaction. In fact, it has been previously observed that surface-induced CD changes are best observed at very low protein concentrations [45,46].

Interestingly, the GNR-induced changes were not restored by addition of sulfate, in contrast to the extinction changes (Figure 6), indicating a partially irreversible loss of α-helical structure. Both the observed spectral changes (Figure 1) and the irreversibility showed in the CD spectra (Figure 6) were similar to those induced in BSA by adsorption to, and desorption from, polystyrene sulfonate particles [47]. Moreover, CD decrease has been reported in a previous study on the interaction of BSA with CTAB-coated GNRs [24]. In that case, the incubation temperature was 65 °C, that possibly further destabilized the protein secondary structure.

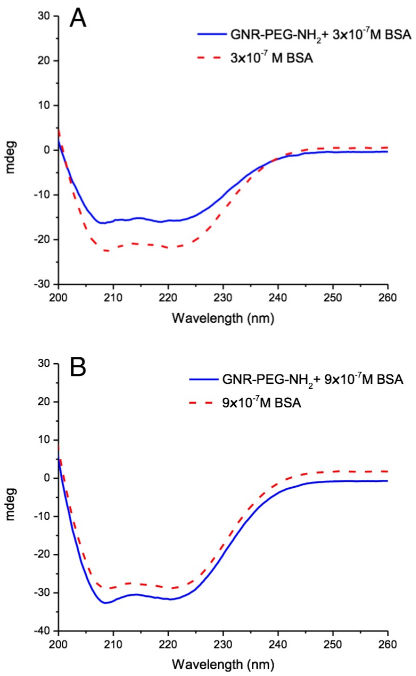

Figure 5. CD spectra of BSA 3×10^{-7} M (A) or 9×10^{-7} M (B) recorded in water and in the presence of GNR-PEG-NH_2 (15nm).

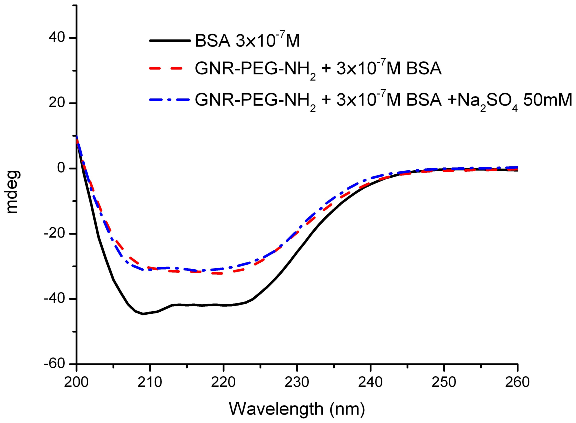

Figure 6. CD spectra of BSA, in the presence of GNR-PEG-NH_2 (15 nM) and after the addition of Na_2SO_4.

Surface-induced protein unfolding has been discussed for different kinds of surfaces, including nanostructured surfaces [48]. After the formation of contacts at the surface/ solvent interface, the interactions between protein and surface are optimized to some extent. This process can involve, besides other interactions, protein structural rearrangements. Irreversible protein changes can occur at this stage, depending on the type and strength of the surface/protein interaction. Restoring protein solvation, which is more frequently obtained by dilution, or—as in our case—by charge neutralization, will lead to the solubilization of a protein form, which, in some cases, will not completely refold. Noticeably, the irreversibility of BSA secondary structure changes is not correlated with that of GNR-BSA binding which, in fact, is almost complete.

3. Conclusions

A comprehensive view of the reported results demonstrates quite unambiguously that the interactions between differently functionalized GNRs, on one side, and a few representative proteins, on the other, are mainly determined by the electrostatic properties of the interacting moieties—and, in addition, by the presence of electrolytes in solution. These interactions were analyzed in the case of three proteins: hCC, HEWL, and BSA. The interactions between the three proteins and the two kinds of functionalized GNRs appeared exemplary and clearly supported the Coulombic nature of the interaction. The case of the BSA/GNR-PEG-NH_2 complexes is the most relevant one. The interaction gave rise to i) LSPR extinction changes of both the transverse and longitudinal mode bands, ii) a concentration-dependent increase of the hydrodynamic radius, and iii) a net decrease in protein CD signal. In summary, the interaction between BSA and the surface of GNR-PEG-NH_2 can be schematically depicted as protein adsorption followed by partial unfolding. As in the case of the smaller proteins, we propose that the driving force for adsorption is the Coulombic interaction between GNR-PEG-NH_2, bearing a positively charged ammonium group, and the negatively charged BSA. The importance of electrostatic interactions is underscored both by the inhibitory effect of sodium sulfate on the interaction and by the extremely reduced extinction changes, observed when BSA was added to the negatively charged GNR-PEG-COOH.

We like to stress how the irreversibility of the secondary structure changes, observed for BSA, was not accompanied by irreversible BSA/GNR-PEG-NH_2 interactions.

To our knowledge, the strong influence of electrolytes on the interaction between proteins and functionalized nanoparticles - here highlighted- had not been investigated in depth so far, and offers strong evidence for the importance of the role of electrostatics in these interactions. In conclusion, the type of functionalization can direct quite selectively proteins binding to GNRs, leading to different interaction patters and providing useful hints for protein sensing applications.

4. Experimental section

Materials

Sodium borohydride, CTAB, chloroauric acid, silver nitrate, ascorbic acid, O-(3-carboxypropyl) -O″-[2- (3- mercaptopropionylamino) ethyl]-polyethylene glycol (MW 5000, HS-PEG-COOH), polysorbate 20 as well as all chemicals for the various buffer solutions were purchased from Sigma Aldrich. Thiol-PEG-amine (MW 5000, HS-PEG-NH_2) was purchased from Ibis Technologies. Horse heart cytochrome c (hCC, C7752) and chicken hen egg white lysozyme (HEWL, L-7651) were purchased from Sigma Aldrich. Bovine serum albumin (BSA) was purchased from Fluka (5470). Spermine and sodium sulfate were purchased from Merck. All the chemicals and proteins were used as received without further purification and the solutions were prepared with deionized water produced by a Millipore system.

Synthesis of gold nanorods

PEG-coated GNRs. GNRs with longitudinal LSPR band centered at 800 nm (5 nm×20 nm, aspect ratio 4) were synthesized by a seed-mediated CTAB- assisted reduction of chloroauric acid with ascorbic acid, according to Nikoobakht and El-Sayed [50] and modified by Ratto et al. [51,52]. Then GNRs were separated from the reaction by-products through centrifugation [53] and functionalized with HS-PEG-COOH or HS-PEG-NH_2 following the procedure by Tatini et al. [51].

UV–vis–NIR spectrophotometry

UV–vis–NIR spectra were recorded with a double-beam Cary 5 (Varian, Palo Alto, CA, USA) spectrophotometer in the range 1000–350 nm at room temperature in a 1 cm path length PE cuvettes and using Cary WinUV Scan software. Light extinction spectra were recorded after dilution (1:20) of the functionalized GNRs in Milli-Q water at pH 5.2 or 50 mM phosphate buffer (PB) at physiological pH. The final GNR concentration was 15 nM. The spectra were recorded before and after the addition of BSA, HEWL or hCC at increasing concentrations (3×10^{-8} M, 3×10^{-7} M, 3×10^{-6} M, 5×10^{-6} M and 10^{-5} M). All the spectra were collected at room temperature immediately after the addition and mixing of the protein in the sample.

Dynamic light scattering measurements

DLS was performed on a zeta potential/particle sizer (Malvern Nano ZS90) to determine the distribution of the hydrodynamic diameters of the functionalized GNRs and of aggregates eventually formed after the addition of the protein. Samples were prepared following the same procedure described for UV–vis–NIR spectrophotometry in 1 cm path length PE cuvettes.

Circular dichroism (CD) measurements

CD spectra were recorded at 25 °C with a Jasco J-810 spectropolarimeter equipped with a Peltier type temperature control system (Jasco PTC-4235) in a 1 cm path length quartz cell and using Spectra Manager software. Briefly, measurements were performed in Milli-Q water (1 ml) at pH 5.2 with GNR-PEG-COOH or GNR-PEG-NH_2 (15 nM) and increasing concentrations of BSA (9×10^{-8} M to 1.2×10^{-6} M). The instrumental conditions are reported in Table S1.

6. Supporting Informations

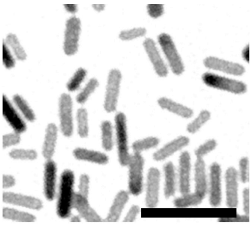

Figure S1. TEM images of GNR-CTAB of average size 5 nm x 20 nm, aspect ratio 4. Scale bar: 50 nm.

Table S1. CD measurements operating conditions.

Instrument	**Jasco J-810**
CD spectra range	200-260 nm
Scanning Speed	20 nm/min
Data pitch	1 nm
Accumulation	5

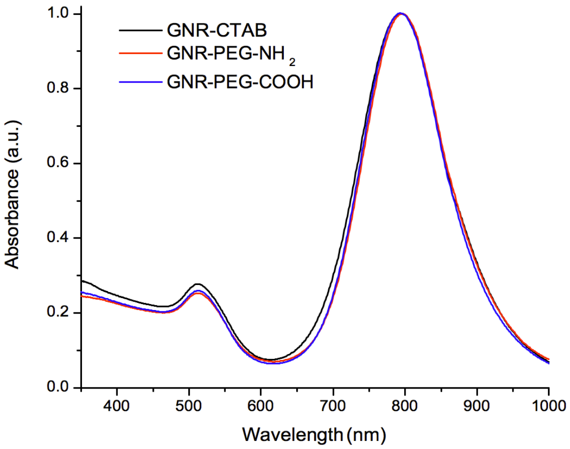

Figure S2. UV-vis-NIR spectra of GNR-CTAB, GNR-PEG-NH $_2$, and GNR-PEG-COOH in Milli-Q water.

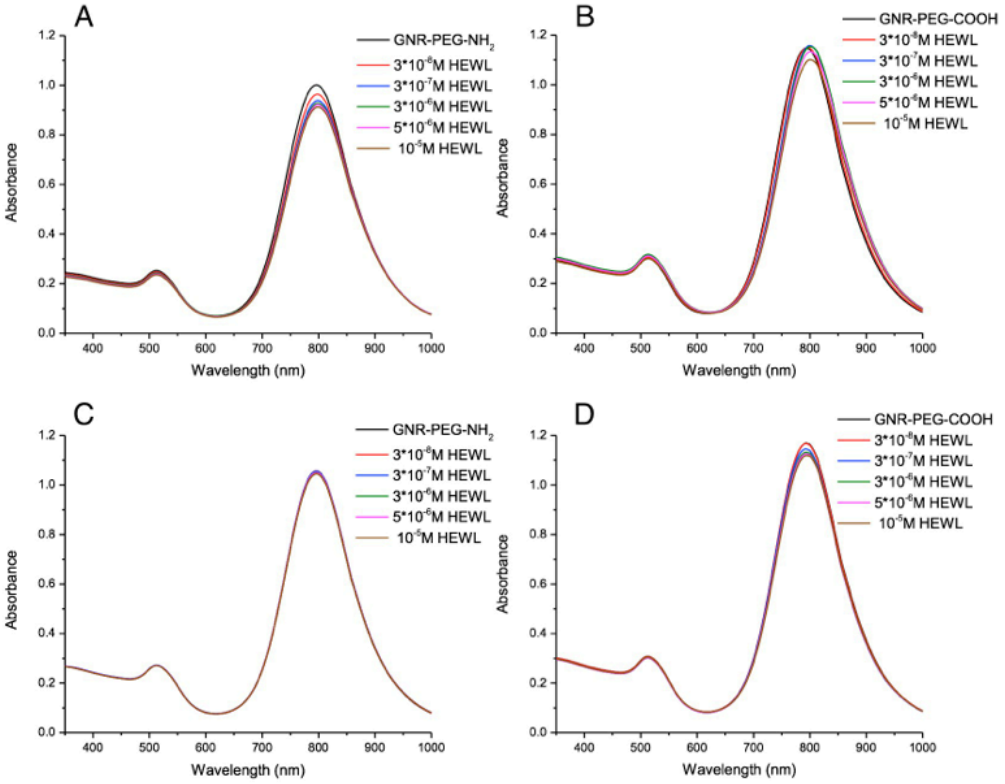

Figure S3. UV-vis-NIR spectra of GNR-PEG-NH_2 (15nM) in water (A) or in PB (C) and GNR-PEG-COOH in water (B) or PB (D). Specifically, spectra were recorded before and after the addition of HEWL at different concentrations. The inset in panel B shows the shift of the longitudinal LSPR band as a function of the HEWL concentration.

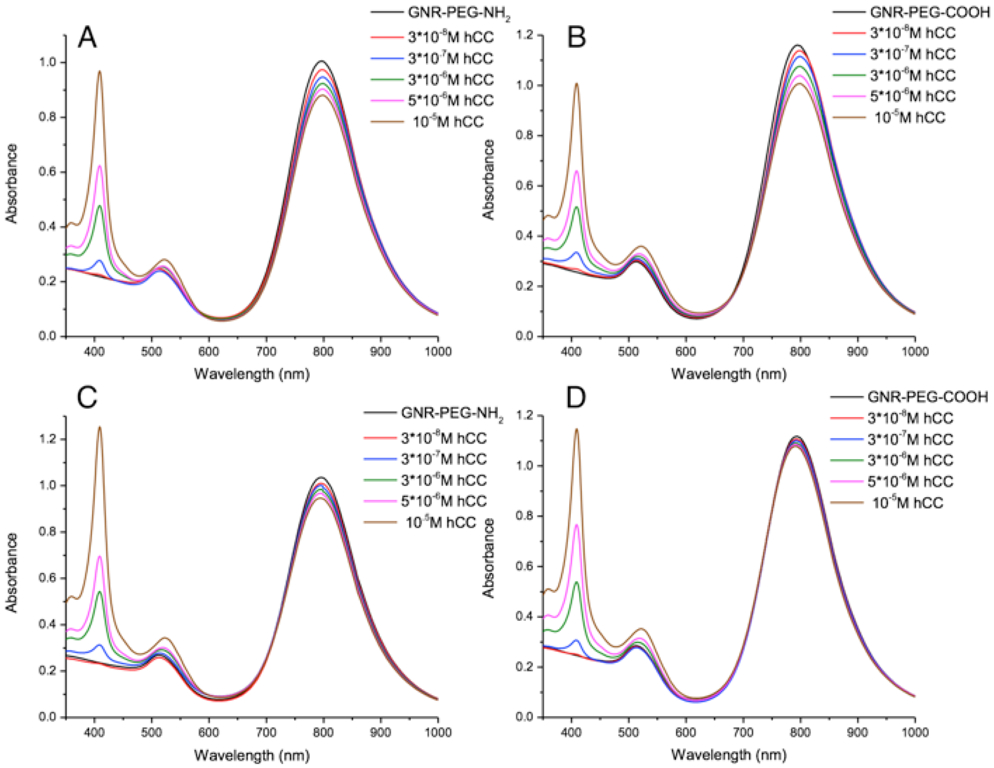

Figure S4. UV-vis-NIR spectra of GNR-PEG-NH$_2$ (15 nM) in water (A) or in PB (C) and GNR-PEG-COOH in water (B) or in PB (D). Specifically, spectra were recorded before and after the addition of hCC at different concentrations.

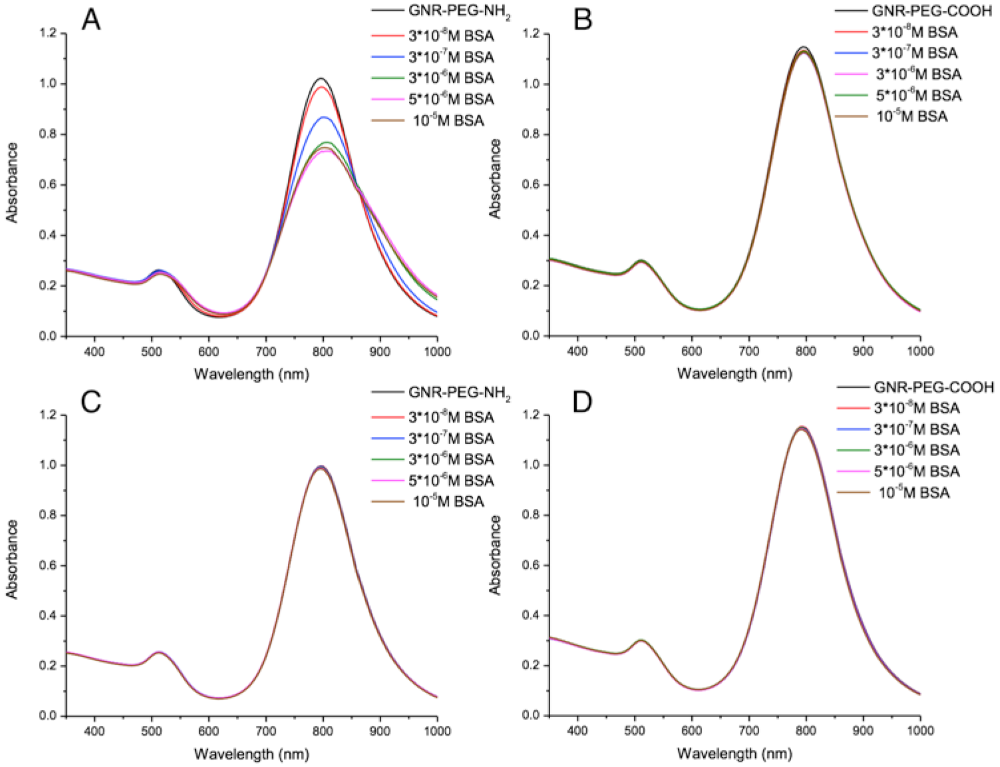

Figure S5. UV-vis-NIR spectra of GNR-PEG-NH_2 (15nM) in water (A) or in PB (C) and GNR-PEG-COOH in water (B) or PB (D). Specifically, spectra were recorded before and after the addition of BSA at different concentrations.

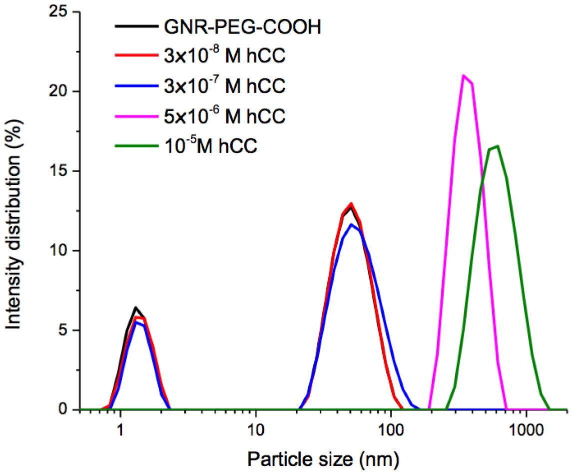

Figure S6. Size distribution curves of GNR-PEG-COOH (15nM) in Milli-Q water before and after the addition of increasing concentrations of hCC.

Table S2. Hydrodynamic diameter and intensity percentage of DLS peaks relative to GNR-PEG-COOH before and after the addition of increasing concentrations of hCC in Milli-Q water.

GNR-PEG-COOH/ hCC	**Hydrodynamic radius ± σ (nm)**		**Intensity (%)**	
[hCC]	**Peak 1**	**Peak 2**	**Peak 1**	**Peak 2**
0	52.6 ± 16.9	1.4 ± 0.3	75.9	24.1
3×10^{-8} M	52.8 ± 16.8	1.4 ± 0.3	76.5	23.5
3×10^{-7} M	57.9 ± 22.0	1.3 ± 0.3	79.9	20.1
5×10^{-6} M	375.7 ± 93.46	--	100	--
10^{-5} M	624.9 ± 203.5	--	100	--

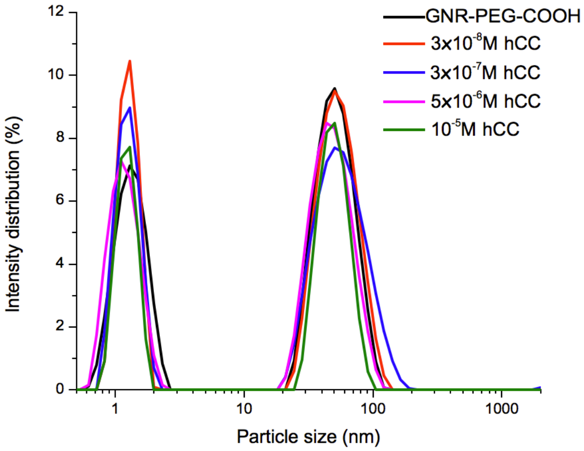

Figure S7. Size distribution curves of GNR-PEG-COOH (15nM) in PB before and after the addition of increasing concentrations of hCC.

Table S3. Hydrodynamic diameter and intensity percentage of DLS peaks relative to GNR-PEG-COOH before and after the addition of increasing concentrations of hCC in PB.

GNR-PEG-COOH/ hCC	**Hydrodynamic radius ± σ (nm)**		**Intensity (%)**	
[hCC]	**Peak 1**	**Peak 2**	**Peak 1**	**Peak 2**
0	59.5 ± 17.8	1.4 ± 0.4	62.1	37.9
3×10^{-8} M	56.0 ± 19.5	1.3 ± 0.3	62.2	37.8
3×10^{-7} M	60.8 ± 27.2	1.3 ± 0.3	63.3	36.7
5×10^{-6} M	50.1 ± 17.7	1.2 ± 0.3	60.8	39.2
10^{-5} M	50.9 ± 13.5	1.3 ± 0.2	60.9	39.1

Acknowledgments

Beneficentia Stiftung (Vaduz, Liechtenstein) and the Tuscan Region ("NANOTREAT" project) are gratefully acknowledge for the generous financial support.

References

[1] S. Eustis, M.A. El-Sayed, Chem. Soc. Rev. 35 (2006) 209.
[2] K. Liu, N. Zhao, E. Kumacheva, Chem. Soc. Rev. 40 (2011) 656.
[3] E.C. Dreaden, A. Alkilany, X. Huang, C.J. Murphy, M.A. El-Sayed, Chem. Soc. Rev. 41 (2012) 2740.
[4] M.A. Garcia, J. Phys. D. Appl. Phys. 44 (2011) 283001.
[5] N. Li, P. Zhao, D. Astruc, Angew. Chem. Int. Ed. 53 (2014) 1756.
[6] J. Pérez-Juste, I. Pastoriza Santos, L.M. Liz-Marzàn, P. Mulvaney, Coord. Chem. Rev. 249 (2005) 1870.
[7] X. Huang, I.H. El-Sayed, W. Qian, M.A. El-Sayed, J. Am. Chem. Soc. 128 (2006) 2115.
[8] C.J. Murphy, A.M. Gole, S.E. Hunyadi, J.W. Stone, P.N. Sisco, A. Alkilany, B.E. Kinard, P. Hankins, Chem. Commun. 5 (2008) 544.
[9] G. Han, P. Ghosh, V.M. Rotello, Adv. Exp. Med. Biol. 620 (2007) 48.
[10] L. Tong, Y. Zhao, T.B. Huff, M.N. Hansen, A. Wei, J.X. Cheng, Adv. Mater. 19 (2007) 3136.
[11] G. Von Maltzahn, J.H. Park, A.N. Agrawal, K. Bandaru, S.K. Das, M.J. Sailo, Cancer Res. 69 (2009) 3892.
[12] F. Ratto, P. Matteini, F. Rossi, L. Menabuoni, N. Tiwari, S.K. Kulkarni, R. Pini, Nanomed. Nanotechnol. Biol. Med. 5 (2009) 143.

[13] O. Kedem, A. Vaskevich, I. Rubinstein, J. Phys. Chem. C 118 (2014) 8227.
[14] O.R. Miranda, H.-T. Chen, C.-C. Yang, O.H.F. Bunz, V.M. Rotello, J. Am. Chem. Soc. 132 (2010) 5285.
[15] A.D. MacFarland, R.P. Van Duyne, Nano Lett. 3 (2003) 1057.
[16] S. Link, M.B. Mohamed, M.A. El-Sayed, J. Phys. Chem. B 103 (1999) 3073.
[17] C.-D. Chen, S.-F. Cheng, L.-K. Chau, C.R.C. Wang, Biosens. Bioelectron. 22 (2007) 926.
[18] G.J. Nusz, S.M. Marinakos, A. Curry, A. Dahlin, F. Höök, A. Wax, A. Chilkoti, Anal. Chem. 80 (2008) 984.
[19] C. Yu, J. Irudayaraj, Anal. Chem. 79 (2007) 572.
[20] K. Saha, S.S. Agasti, C. Kim, X. Li, V. Rotello, Chem. Rev. 112 (2012) 2739.
[21] M. De, S. Rana, H. Akpinar, O.R. Miranda, R.R. Arvizo, U.H.F. Bunz, V.M. Rotello, Nat. Chem. 1 (2009) 461.
[22] C.-C. You, O.R. Miranda, B. Gider, P.S. Ghosh, I.-B. Kim, B. Erdugan, S.A. Krovi, U.H.F. Bunz, V.M. Rotello, Nat. Nanotechnol. 2 (2007) 318.
[23] I. Lynch, K.A. Dawson, Nano Today 3 (2008) 40.
[24] S. Chakraborty, P. Joshi, V. Shanker, Z.A. Ansari, S.P. Singh, P. Chakrabarti, Langmuir 27 (2011) 7722.
[25] S. Alam, A. Mukhopadhyay, J. Phys. Chem. C 118 (2014) 27459.
[26] S.T. Kim, K. Saha, C.S. Kim, V.M. Rotello, Acc. Chem. Res. 46 (2013) 681.
[27] M.P. Monopoli, C. Aberg, A. Salvati, K.A. Dawson, Nat. Nanotechnol. 7 (2012) 779.
[28] A. Salvati, A.S. Pitek, M.P. Monopoli, K. Prapainop, F. Baldelli Bombelli, D.R. Kristov, P.M. Kelly, C. Aberg, E. Mahor, K.A. Dawson, Nat. Nanotechnol. 8 (2013) 137.
[29] A.E. Nel, L. Mädler, D. Velegol, T. Xia, E.M.V. Hoek, P. Somasundaran, F. Klaessig, V. Castranova, M. Thompson, Nat. Mater. 8 (2009) 543.
[30] T.T. Moghadam, B. Ranjbar, K. Khajeh, S.M. Etezad, K. Khalifeh, M.R. Ganjalikhanyl, Int. J. Biol. Macromol. 49 (2011) 629.
[31] S.O. Pereira, A. Barros-Timmons, T. Trindade, Colloid Polym. Sci. 292 (2014) 33.
[32] A.M. Alkilany, A. Shatanawi, T. Kurtz, R.B. Caldwell, R.W. Caldwell, Small 8 (2012) 1270.
[33] F. Tatini, I. Landini, F. Scaletti, L. Massai, S. Centi, F. Ratto, S. Nobili, G. Romano, F. Fusi, L. Messori, E. Mini, R. Pini, J. Mater. Chem. B 2 (2014) 6072.
[34] P.N. Sisco, C.G. Wilson, D. Chernak, J.C. Clark, E.M. Grzincic, K. Ako-Asare, E.C. Goldsmith, C.J. Murphy, PLoS One 9 (2014) e86670.
[35] P.K. Jain, S. Eustis, M.A. El-Sayed, J. Phys. Chem. B 110 (2006) 18243.
[36] S.K. Lee, M.A. El-Sayed, J. Phys. Chem. B 110 (2006) 19220.
[37] M. Chanana, L.M. Liz-Marzan, Nanophotonics 1 (2012) 199.
[38] J. Voros, Biophys. J. 87 (2004) 553.
[39] K.G. Thomas, S. Barazzouk, B.I. Ipe, S.T.S. Joseph, P.V. Kamat, J. Phys. Chem. B 108 (2004) 13066.
[40] A. Verma, J.M. Simard, V.M. Rotello, Langmuir 20 (2004) 4178.

[41] S. Boulos, T.A. Davis, J.A. Yang, S.E. Lohse, A.M. Alkilany, L.A. Holland, C.J. Murphy, Langmuir 29 (2013) 14984.

[42] S. Milani, F. Baldelli Bombelli, A.S. Pitek, K.A. Dawson, J. Radler, ACS Nano 6 (2012) 2532.

[43] J. Rodriguez-Fernandez, J. Perez-Juste, L.M. Liz-Marzan, P.R. Lang, J. Phys. Chem. C 111 (2007) 5020.

[44] H. Liu, N. Pierre-Pierre, Q. Huo, Gold Bull. 45 (2012) 187.

[45] K. Chen, Y. Xu, S. Rana, O.R. Miranda, P.L. Dubin, V.M. Rotello, L. Sun, X. Guo, Biomacromolecules 12 (2011) 2552.

[46] S. Laera, G. Ceccone, F. Rossi, D. Gilliland, R. Hussain, G. Siligardi, L. Calzolai, Nano Lett. 11 (2011) 4480.

[47] P. Sevilla, S. Sánchez-Cortés, J.V. García-Ramos, A. Feis, J. Phys. Chem. B 118 (2014) 5082.

[48] W. Norde, C.E. Giacomelli, J. Biotechnol. 79 (2000) 259.

[49] C.A. Haynes, W. Norde, Colloids Surf. B: Biointerfaces 2 (1994) 517.

[50] B. Nikoobakht, M.A. El-Sayed, Chem. Mater. 15 (2003) 1957.

[51] F. Tatini, I. Landini, F. Scaletti, L. Massai, S. Centi, F. Ratto, S. Nobili, G. Romano, F. Fusi, L. Messori, E. Mini, R. Pini, J. Mater. Chem. B 2 (2014) 6072.

[52] F. Ratto, P. Matteini, F. Rossi, R. Pini, J. Nanopart. Res. 12 (2010) 2029.

[53] F. Scaletti, C.S. Kim, L. Messori, V.M. Rotello, MethodsX 1 (2014) 118.

Chapter 5

Gold Nanorod-Stabilized Nanocapsules for the Delivery of Anticancer Drugs

Gold Nanorod-Stabilized Nanocapsules for the Delivery of Anticancer Drugs*

* *Unpublished results from a work in collaboration with Dr. Chang Soo Kim, Ms Gülen Yesilbag, Mr Ryan F. Landis, and Prof. V. M. Rotello (University of Massachusetts, Amherst).*

Graphical abstract

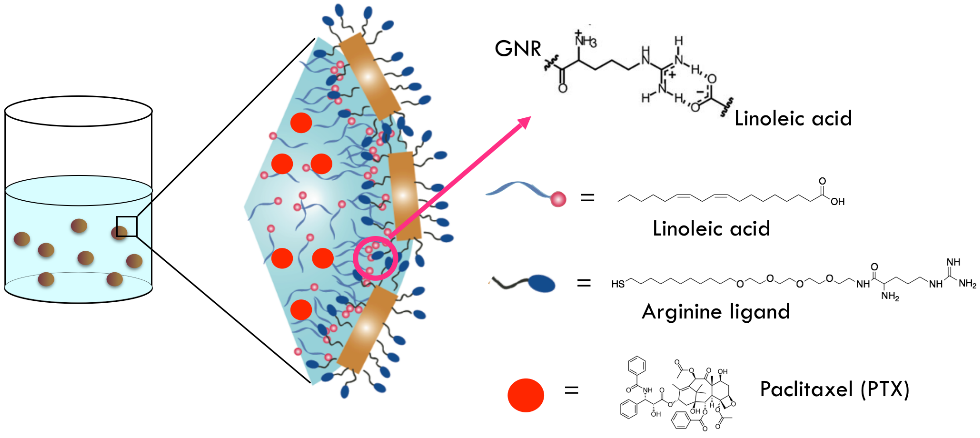

1. Introduction

Drug delivery systems (DDS) provide safe platforms for delivery of different pharmaceutical compounds, improving their therapeutic effect through controlled release properties. Targeting of therapeutics specifically to tumors further enhances the efficacy of these treatments, while minimizing side effects. There are three major strategies for targeting. Active targeting to cell-surface receptors provides an obvious strategy, [1] that has been challenging to implement. [2] Passive targeting uses particles that are small enough (between 10 and 200 nm) to avoid capture of the DDs by macrophages of the reticuloendothelial system. [3] Due to their nanoscale size (<200 nm), these systems can take advantage of the "enhanced permeability and retention (EPR) effect", accumulating preferentially in tumor tissues due to the leaky vasculature found there. [4] The final strategy is through external control of therapeutic action, providing the potential for pin-point accuracy in targeting. [5]

Nanocapsules (NCs) provide a versatile DDS platform, providing promising tools for drug delivery. [6] Most of these systems are comprised of lipids and/or polymers self-assembled into capsules with aqueous interiors. [7] Recently, gold nanoparticle (GNP)-stabilized NCs (GNP-NCs) have been demonstrated to deliver proteins and small molecule drugs directly into the cytosol. [8-10] In these systems, nanoparticles are assembled at the interface of an oil-in-water nanoemulsion through specific supramolecular interactions between GNPs and the oil droplet. [8] These GNP-NCs feature excellent stability and low toxicity, and demonstrate an efficient delivery of drugs and proteins into the cytosol leading to cellular apoptosis. [10] Additionally, their size (~100 nm) makes them ideal for utilizing the EPR effect.

Recent studies by Rotello have demonstrated that composite films containing gold nanoparticles and polyamidoamine (PAMAM) dendrimers allows tuning of the release profile of the loaded drug by changing dendrimer ratio and generation. [11,12] In particular, lower generation dendrimers show a faster doxorubicin release than higher generation analogs. Translating these films onto the surface of AuNPNCs provides a platform with readily tunable release properties in unpublished results by the Rotello group.

Replacing the spherical particles in GNP-NCs with nanorods (GNRs) would provide NCs with unique optical properties that would allow external control of drug release. In particular, GNRs feature an absorption in the near IR region (longitudinal surface plasmon resonance, LSPR) of the spectrum that can be tuned between 650 nm and 1100 nm. [13] Due to this intense longitudinal absorption, GNRs are able to efficiently convert NIR light into localized heat. This tunability in absorption allows GNRs to be heated at wavelengths where tissue features minimal absorption and scattering, allowing excellent deep-tissue heating of these systems. [14] This ability to localize heating provides an effective targeting tool, making GNRs of great interest for photothermal treatment of cancer. [15] Therefore, the goal of the present project is to integrate the controlled release properties of the current GNP-NCs systems with the NIR heating capabilities of GNRs, providing DDS with highly specific spatiotemporal therapeutic action.

Specifically, the present chapter reports:

- Synthesis, characterization and functionalization of small sized GNRs.
- Self-assembling of these GNRs onto fatty acid nanodroplets to provide 100-200 nm GNR-NCs and GNR-NCs loaded with the anticancer drug paclitaxel (PTX).
- Crosslinking of these GNR-NCs with a dendrimer.
- Demonstration of the structural and colloidal stability of GNR-NCs in physiological conditions.
- In vitro cytotoxicity of GNR-NCs and PTX loaded nanocapsules.

Further studies will be focused on the optimization of the NIR photorelease properties of the GNR-NCs in solution and on the in vitro effectiveness of the photothermal release against breast tumor cells, focusing on cell uptake and effective release of therapeutics.

2. Results and Discussion

Synthesis, characterization and functionalization of GNRs

Small GNRs (~20 nm length) are essential to obtain GNR-NCs with an optimal size for drug delivery purpose (100-200 nm). These small gold nanorods were synthesized following the seed-mediated method according to Nikoobakht et al., [16] with appropriate modifications to obtain smaller-sized GNRs as reported in Chapter 1. The optical properties of GNRs have been assessed through UV-vis spectroscopy, and the size evaluated by measuring the width and length of particles using transmission electron microscopy (TEM) imaging (see Chapter 1). After synthesis, GNRs were purified with a two-step centrifugation method, as reported in Chapter 2, to remove the excess cytotoxic cetyltrimethylammonium bromide (CTAB) required for their formation, and to separate GNRs from other reaction by-products. [17] The GNRs were then functionalized with a ligand bearing an arginine (Arg) group (Figure 1), designed to allow the NCs formation. [18] The functionalization was performed with a two-step procedure optimized for the GNR's size of interest (see the "Experimental section"for details).

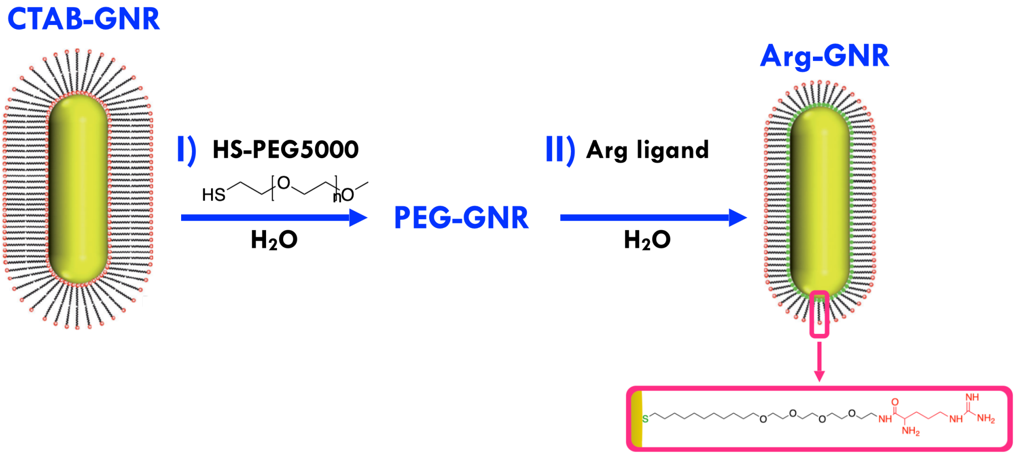

Figure 1. Schematic representation of GNR's functionalization with Arg ligand.

Firstly, GNRs were functionalized with HS-PEG5000 to stabilize GNRs, [19] and, thereafter, thiol exchange with the selected arginine ligand, was performed. Then GNRs were washed to remove the remaining displaced CTAB from GNRs functionalized with the arginine ligand (Arg-GNR). The characterization of Arg-GNRs was performed through UV-vis spectroscopy (Figure 2A) and TEM imaging (Figure 2B). Functionalized GNRs showed the same size of CTAB-coated GNRs, while the LSPR of GNRs was 15 nm red-shifted, according to literature. [20] Moreover, laser desorption ionization mass spectrometry (LDI-MS) was used to assess the effective functionalization and the complete removal of CTAB (Figure 3). [21] Specifically, in the LDI mass spectrum, peaks referred to CTAB (i.e. 285 m/z) or PEG (i.e. 5000m/z) were not detected. However small amount of PEG may not be detected through LDI-MS due to ionic suppressions. Therefore the complete thiol exchange can not be staten.

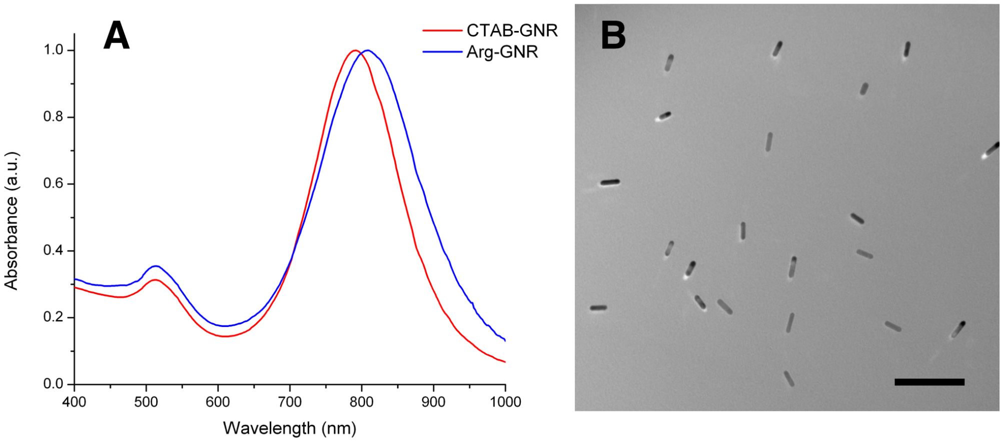

Figure 2. Extinction spectra of GNRs before and after functionalization with the Arg ligand (A) and TEM image (B) of Arg-GNRs. Scale bar: 100nm

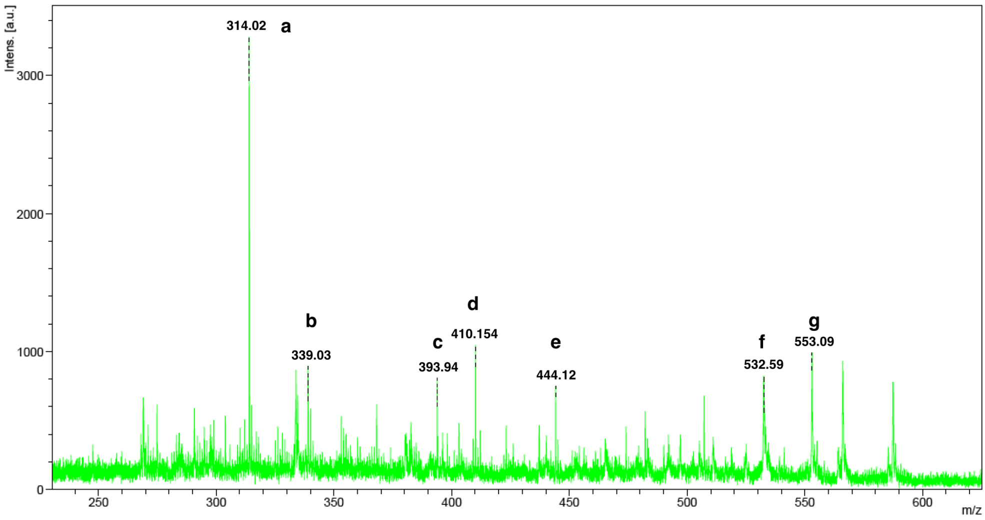

Figure 3. LDI mass spectrum of GNRs after functionalization with the arginine ligand. a) is a fragment of the Arg ligand with Na+ ($C_{15}H_{31}NaO_3S$) b), d), and e) are peaks presumably due to chemical transformations of the Arg ligand during LDI; f) is the Arg ligand, and g) is due to chemical transformation of Arg group in the N-hydroxyarginine. [22]

Fabrication and characterization of GNR-stabilized NCs

To generate nanoscale GNR-stabilized NCs, the method reported by Rotello et al. have been used and adapted to Arg-GNRs. [8] The strategy relies upon nanoscale oil droplet stabilization through supramolecular interactions between the GNRs that constitute the GNR-NCs shell with the "oil" interior. The well-known arginine-carboxylate hydrogen bonding/electrostatic interaction [23-24] was exploited through use of biocompatible linoleic acid as the "oil" interior and Arg-GNRs as the nanoparticle shell (Figure 4). GNR-stabilized NCs were fabricated by a two-step procedure. Firstly, template oil droplets with a size below 200 nm were generated by agitating linoleic acid in 5 mM phosphate buffer (PB) at pH 7.4 in the presence of a small amount of Arg-GNRs using a commercial homogenizer.

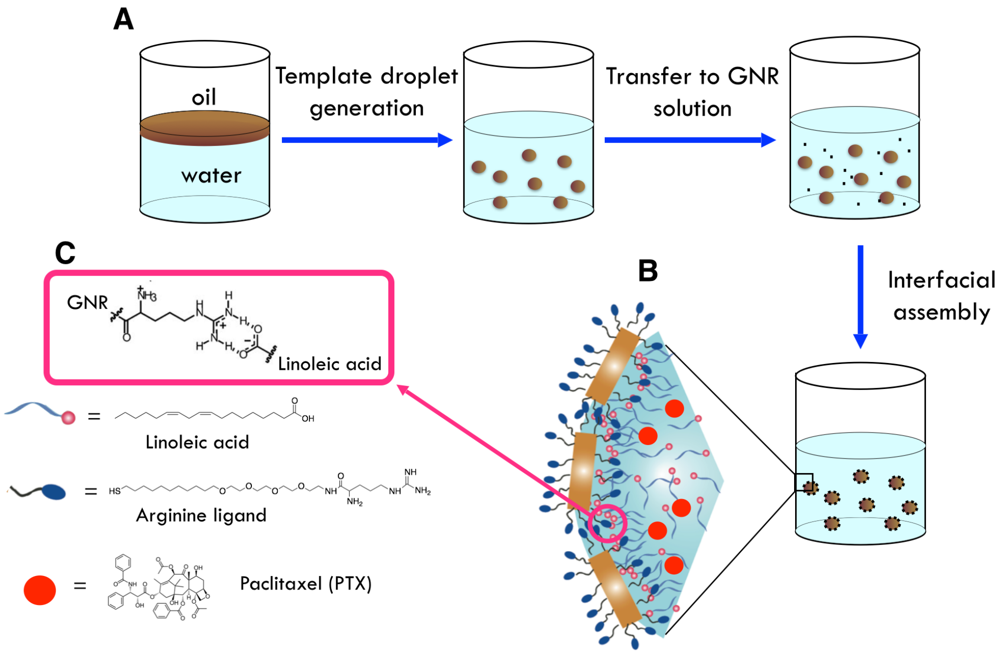

Figure 4. Fabrication of GNR-stabilized NCs. A) Generation of nanosized oil-in-water droplets followed by interfacial assembly of Arg-GNRs. B) Interface of the oil-in water emulsion. C) Supramolecular interactions between Arg-GNRs and linoleic acid through arginine-carboxylate hydrogen bonding/electrostatic interactions.

In the second step, the droplets were transferred into a solutions of Arg-GNRs, resulting in essentially instantaneous assembly of the Arg-GNRs at the droplets surface through Arg-carboxylate interactions. The GNR-NCs formation was optimized by varying the ratio between linoleic acid and Arg-GNRs as well as the Arg-GNR/droplet ratio (see "Experimental section"). The resultant assemblies were then characterized by UV-vis spectroscopy (Figure 5A) and TEM (Figure 5B). At the optimum GNR/droplet ratio, TEM image shows essentially no free GNRs on the sample grid and almost spherical assemblies of packed Arg-GNRs. Since TEM samples were obtained by drying a small amount of the GNR-NCs solution on a TEM grid, the size of the nanocapsules may be affected by the drying process. Therefore, DLS measurements were performed to evaluate the size of GNR-NCs. The hydrodynamic diameter of GNR-NCs was 144 nm.

Paclitaxel (PTX)-loaded GNR-NCs were prepared following the same procedure, adding PTX into the linoleic acid, where it is solubilized due to the hydrophobicity of PTX. [8]

Due to the interactions between the Arg group of Arg-GNR and the carboxylate group of the linoleic acid, the extinction spectrum of GNR-NCs shows a relevant red-shift of the LSPR compared to Arg-GNRs (Figure 5A). In fact it is well-known that an alteration of the GNR's local environment as well as the plasmon coupling between GNRs induce a shift of GNR's plasmon resonance. [25,26]

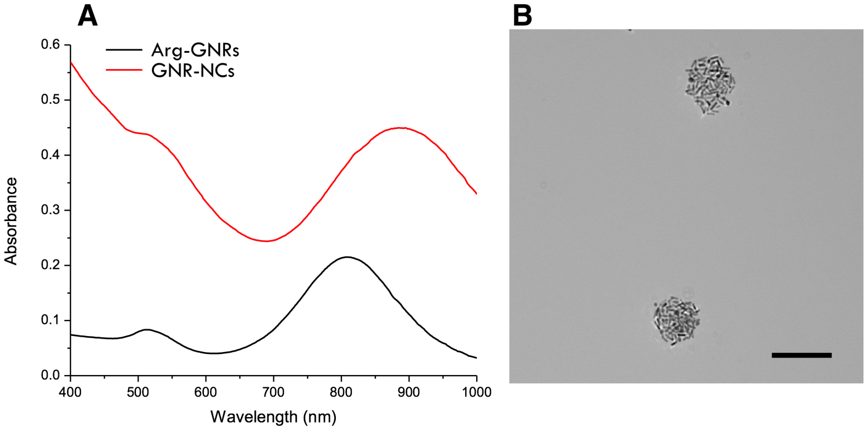

Figure 5. Extinction spectra of GNR-NCs and Arg-GNRs (A), and TEM image of GNR-NCs (B) obtained at the optimum Arg-GNR/droplets ratio. Scale bar: 200nm.

Crosslinking of GNR-NCs with polyamidoamine dendrimer

In order to generate ideal platforms for PTX release, GNRs in NCs were crosslinked with 4th generation (G4) polyamidoamine (PAMAM) dendrimer (Figure 11) using dithiocarbamate (DTC) chemistry (Figure 6), providing NCs that are stable to pH, temperature and ionic strength variations. [27] After crosslinking, GNR-NCs were washed through centrifugation, allowing removal of "free" GNRs and other potential by-products. Table 1 shows the hydrodynamic diameter of GNR-NCs crosslinked with different molar ratio between the dendrimer linkers and GNRs.

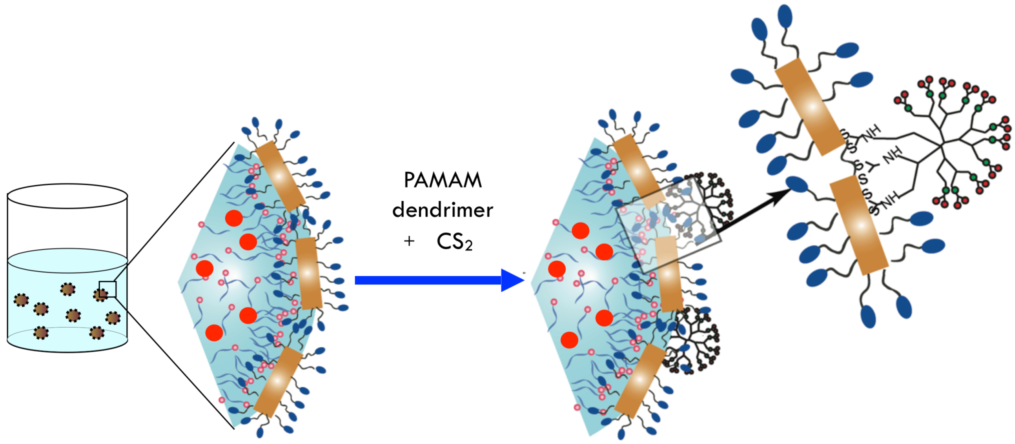

Figure 6. Schematic representation of the DTC crosslinking of GNR-NCs.

Table 1. Hydrodynamic diameter of GNR-NCs before and after crosslinking with G4 PAMAM dendrimer at different dendrimer/GNR molar ratio.

Sample*	Hydrodinamic diameter (nm)
A	144
B	159
C	167
D	210

* GNR-NCs before (A) and after crosslinking with G4 PAMAM dendrimer at dendrimer/GNR ratio of 0.25 (B), 0.50 (C) and 1.00 (D).

GNR-NCs crosslinked with the dendrimer were bigger than GNR-NCs. However the size was still reasonable to be used for drug delivery. Moreover it is evident that increasing the dendrimer/GNR molar ratio the GNR-NCs' hydrodynamic diameter increased as well, consistent with a higher amount of crosslinked dendrimer on the NCs surface. Crosslinked GNR-NCs were then characterized using UV-vis spectroscopy and TEM. After crosslinking, NCs maintain the optical properties (Figure 7) as well as the shape of GNR-NCs (Figure 8).

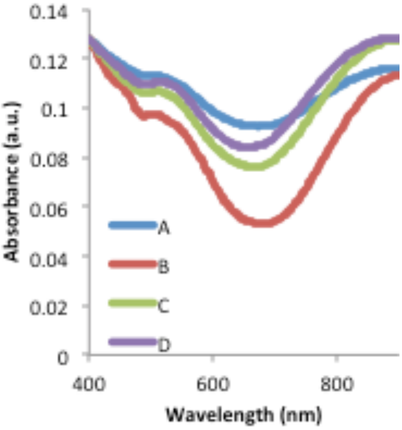

Figure 7. Extinction spectra of GNR-NCs before (A) and after crosslinking with G4 PAMAM dendrimer at dendrimer/GNR ratio of 0.25 (B), 0.50 (C) and 1.00 (D).

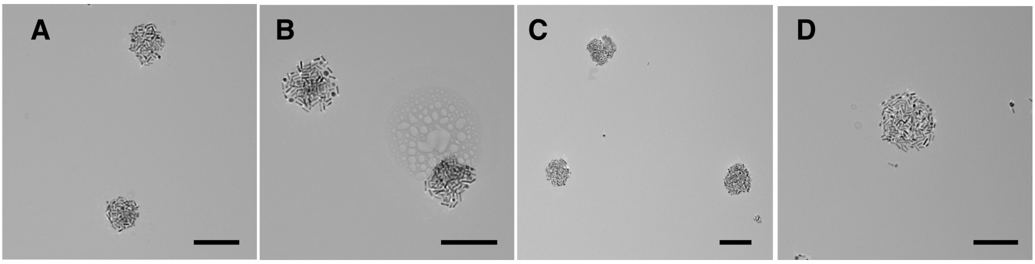

Figure 8. TEM images of GNR-NCs before (A) and after crosslinking with G4 PAMAM dendrimer at dendrimer/GNR ratio of 0.25 (B), 0.50 (C) and 1.00 (D). Scale bars: 200nm.

Structural and colloidal stability of GNR-NCs and crosslinked GNR-NCs in physiological conditions.

The stability in PB and in 50% serum of both GNR-NCs and GNR-NCs crosslinked with 25% G4 PAMAM dendrimer was then evaluated through UV-vis spectroscopy and DLS measurements over 24 hours. Due to the relevant absorption of serum, extinction spectra were recorded only in PB. Figure 8 shows a red-shift of the LSPR band of GNR-NCs, possibly due to reorganization of the structure, while the extinction spectrum of crosslinked GNR-NCs did not show significant changes in the LSPR band. In fact, DLS measurements (Table 2) revealed that in PB the hydrodynamic diameter of GNR-NCs was significantly increased respect to crosslinked GNR-NCs.

Moreover, GNR-NCs aggreagated and deposited at the bottom of the cuvette in the presence of 50% serum, while crosslinked GNR-NCs showed only an increase in the size, presumably due to interaction/adsorption of proteins on nanocapsules surface. Therefore, the high stability of crosslinked GNR-NCs under physiological conditions makes them potentially useful as delivery vehicles.

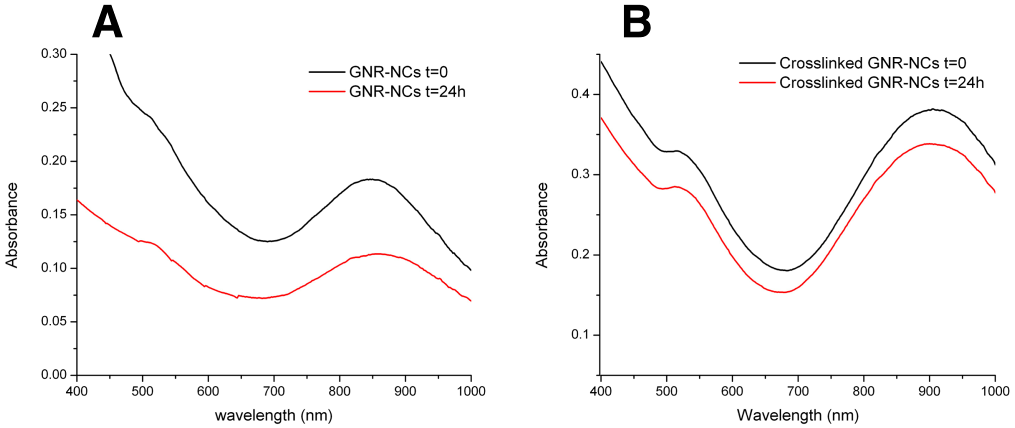

Figure 8. Extinction spectra of GNR-NCs (A) and crosslinked GNR-NCs (B) in 10 mM PB over 24h.

Table 2. Hydrodynamic diameter of GNR-NCs and crosslinked GNR-NCs in PB and 50% serum over 24 hours at 37°C.

Sample	Hydrodinamic diameter (nm)		
	PB t=0	PB t=24h	50% serum t=24h
GNR-NCs	144	310	- -
Crosslinked GNR-NCs	159	164	265

3. Preliminary *in vitro* studies

Preliminary studies of cellular delivery and citotoxicity of nanocapsules were performed. To test the delivery, GNR-NCs loaded with Nile Red fluorophore were incubated with HeLa cells, and payload delivery followed with a fluorescent microscope. As shown in Figure 9, a strong red fluorescence originated from nile red was evenly distributed thorough the whole cell cytosol, indicating an efficient and non-endosomal uptake of the dye (Figure 9B). Moreover, cells did not show any obvious morphology change after delivery, highlighting the bio-compatibility of the delivery vehicle (Figure 9A).

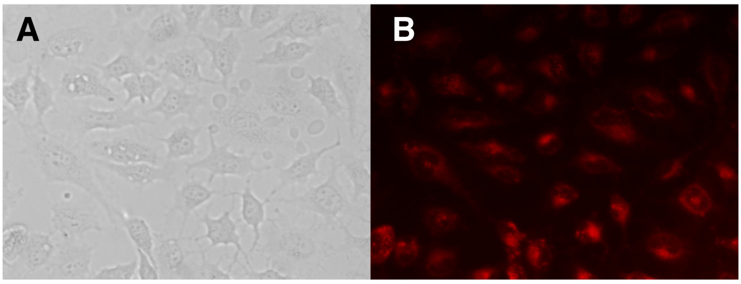

Figure 9. Delivery of Nile Red encapsulated GNR-NCs in HeLa cells.a) Bright field and b) red channel fluorescent microscopy images.

There are two potential mechanisms for this payload delivery. In the first mechanism, material is transferred through membrane fusion from GNR-NCs to the cell without nanocapsules uptake, while in the second one, the cell takes up the nanocapsule through an endocytotic mechanism, with payload release occurring inside the cell. Previous studies on GNP-NCs have shown that the payload delivery follows the nanocapsule-cell fusion mechanism. [8] However, further studies to confirm this hypothesis has to be performed.

In an other experiment, the efficacy of nanocapsules as drug delivery systems was investigated in cell culture models. Alamar Blue viability essay and HeLa cells were used to determine the cytotoxicity of GNR-NCs and crosslinked GNR-NCs compared to the PTX-loaded nanocapsules. Figure 10 shows the cell viability of HeLa cells incubated with different concentrations of GNR-NCs and crosslinked GNR-NCs, with and without PTX.

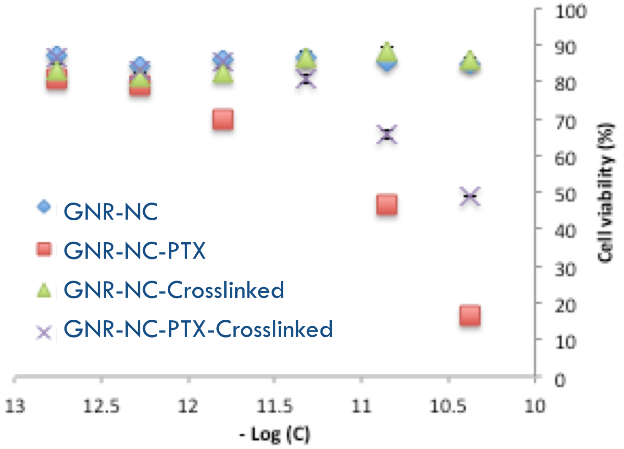

Figure 10. Cytotoxicity of GNR-NCs and crosslinked GNR-NCs compared to PTX-loaded nanocapsules at different concentrations. Cell viability was measured by Alamar Blue assay after 24 h incubation of nanocapsules with HeLa cells. Log (C) refers to concentration of NCs. See Experimental section for calculations of nanocapsules' concentration.

Both GNR-NCs and crosslinked GNR-NCs featured no non-specific cytotoxicity at the concentrations studied, while PTX loaded nanocapsules showed different cytotoxicity profiles. Specifically crosslinked PTX-loaded GNR-NCs were less cytotoxic than non-crosslinked one, indicating that PTX release may be inhibit thanks to the crosslinking of NCs with PAMAM dendrimer. In particular the IC_{50} value for the encapsulated drug was 234 nM for GNR-NCs and 741 nM for crosslinked GNR-NCs, as compared to 7.6 nM for free PTX. [8] Therefore, other than crosslinked nanocapsules, GNR-NCs, may inhibit PTX release, contrary to GNP-NCs (IC_{50} of PTX was 15.8 nM). This difference may be due to the different structure of GNR-NCs compared to 2 nm GNP-stabilized nanocapsules. However, further studies have to be performed to confirm this hypothesis.

4. Conclusions and Future work

In summary, the strategy to develope GNP-NCs has been adapted to produce GNR-stabilized NCs with a size below 200 nm. GNR-NCs have also been crosslinked with G4 PAMAM dendrimer to provide NCs that are stable in physiological conditions. Moreover, crosslinked GNR-NCs have been designed to be safe platforms for delivery and to promote the PTX release upon laser activation. In fact, nanocapsules did not show potential nonspecific NCs cytotoxicity on HeLa cells, while PTX-loaded crosslinked nanocapsules showed a different cytotoxicity profile compared to PTX-loaded GNR-NCs, suggesting that crosslinking may inhibit PTX release.

Further studies will be performed to characterize the potential PTX photorelease in solution and the in vitro effectiveness of the photorelease against HeLa cells.

Characterization of photorelease in solution

The PTX release behavior of the crosslinked capsules will be controlled by adjusting the molar ratio between dendrimer linkers and GNRs. NCs crosslinked with varying amounts of dendrimer will be placed in a dialysis cassette, and PTX release monitored by high-performance liquid chromatography (HPLC) of the surrounding solution. The PTX release rate is expected to decrease upon increasing the dendrimer:GNR ratio (unpublished results by the Rotello group). Thereafter crosslinked capsules, showing little/no release, will be chosen to evaluate the ability of NIR irradiation to promote the release of PTX. The NIR photorelease will be optimized by changing laser irradiation time and power, with the goal of effective PTX release with minimal NIR flux.

In vitro effectiveness of the photothermal release against breast cancer cells

GNR-NCs and PTX-loaded GNR-NCs will be tested in vitro on HeLa cells and, thereafter on MCF-7 (human breast cell line), focusing on both potential nonspecific NCs cytotoxicity as well as ability of the NIR irradiation to efficiently release PTX. The goal is to create carriers with low levels of non-specific toxicity and able to promote drug release upon laser activation. Firstly, the effects of the key components will be tested on the viability of the cell lines: 1) Arg-GNRs alone; 2) linoleic acid alone; 3) GNR-NCs with only linoleic acid; 4) PAMAM dendrimer alone; 5) Crosslinked GNR-NCs.

Then, the toxicity of: 1) PTX-loaded GNR-NCs; 2) Crosslinked PTX-loaded GNR-NCs and PTX alone will be determined, in particular focusing on the toxicity of the conjugates vs free drug. Finally, the effectiveness of the photothermal release will be evaluated testing the viability of cell lines after 1) NIR irradiation only; 2) GNR-NCs uptake and NIR irradiation; 3) PTX-loaded GNR-NCs uptake and NIR irradiation. We will test the effects of these components on cell viability using standard MTT assays. We will also use microscopy to observe any morphological changes that may occur during the delivery process. Finally, flow cytometry will be used to determine cell mortality, information that provides a useful adjunct to viability methods.

In summary crosslinked NCs are expected to be a safe and nontoxic platform for drug delivery and show an externally controlled enhanced drug effect (i.e. cytotoxicity) upon laser activation due to drug release, with minimal damage to normal cells from the NIR activation. These studies could, then, provide the foundation for future pre-clinical animal studies that could lead to an important new therapeutic strategy for tumors.

5. Experimental section

Materials

Sodium borohydride (>98%), cetyltrimethylammonium bromide (>99%), and silver nitrate (99.5%) were purchased from Acros Organics. Chloroauric acid (99.9%) was purchased from Strem Chemical, and L-(+)-ascorbic acid was purchased from Alfa Aesar, while polysorbate 20 (Tween20), the fourth generation (G4) poly (amido amine) (PAMAM) starburst dendrimers, trimethoxysilyl propylene diamine and CS_2 were purchased from Sigma Aldrich. All chemicals were used as received. Paclitaxel was purchased from Polymed Therapeutics. All the solutions were prepared with deionized water produced by a Millipore System.

Synthesis and characterization of gold nanorods

The synthesis of small sized GNRs was performed following the procedure described in Chapter 1. GNRs were characterized through UV-vis spectroscopy and TEM as reported in Experimental section of Chapter 1.

Functionalization of GNRs

GNRs were functionalized following a two step procedure: in the first step GNRs were partially funtionalized with HS-PEG5000, following the procedure by Kinnear et al. [28], to provide stability to GNRs during the removal of CTAB and, thereafter, thiol exchange with the Arg ligand was performed as follow.

The amount of ligand was calculated respect to the total surface of the GNRs as follow:

- The surface of a single GNR was approximated to the surface of a cylinder with two half spheres:

$$S = \pi r^2 + 2\pi r(l - w)$$

were r is the half of the width(w) and l is the length of the GNR.

- The total surface in the sample used for the functionalization was:

$$S_{Tot} = S \bullet m$$

were m is the number of the GNRs moles.

- The amount of ligand was calculated to be

$$Ligand(mg) = \frac{100_{Ligand\_molecules}}{nm^2} * S_{Tot} * \frac{Mw_{Arginine}(g/mol)}{1000}$$

Were $Mw_{Arginine}$ is the molecular weight of the arginine ligand (535.78 g·mol^{-1}).

The amount of calculated ligand was dissolved in Milli-Q water, previously purged with N_2 for 20 minutes; the concentration of the solution was 10mg/ml. The solution of the ligand was added drop wise to the washed GNRs in a glass vial with a magnetic stirring barr. The sample was kept under N_2 and stirred at room temperature for 48 hours.

Thereafter, Arg-functionalized GNRs were washed as follow:

Arg-GNRs were placed in centrifuge tubes (0.5ml for each tube) and Milli-Q water (1ml for each tube) was added: the result GNRs solution was 3 times diluted. GNRs were then centrifuged at a rate of 10630 rpm (12000 g) for 30 minutes for GNRs with AR of 4.8 or rpm (13000g) for 40 minutes. The supernatant was removed and the precipitates resuspended by the addition of 0.45 ml of Milli-Q water, previously purged with N_2. All the resuspended GNRs were then mixed together and kept at 4°C in the dark, under N_2.

Characterization of the functionality through LDI-MS

The LDI-MS analyses were done either on a Bruker Reflex III time-of-flight mass spectrometer (Reflex III). Thee spectrometer is equipped with a 337 nm nitrogen laser, a 1.0-m flight tube, and a stainless steel sample target. All mass spectra were acquired in reflectron mode. Areflectron voltage of 16.1 kV and an accelerating voltage of 20 kV were used. An average of 100 laser shots was fired to acquire each spectrum, and the typical laser power was 70%, which corresponds to approximately 210 μJ/pulse. A 1 μL solution of GNR-NCs (83 nM) in Milli-Q water was applied to target and allowed to air-dry before LDI-MS.

Determination of GNRs concentration

After purification the GNRs concentration was calculated through spectrophotometric measurements. 700 μl of milli-Q water were used as reference for the spectrophotometric measurement.

Then 70 μl of water were removed and 70 μl of washed GNRs were added in the same cuvette: the resulting solution was 10 times diluted respect to the washed GNRs. The spectrum was recorded between 400 nm and 1000 nm with a 2 nm step. The GNRs concentration was then calculated through the Lambert-Beer equation:

$$C= A/(\varepsilon^*l)$$

Where C is the concentration (M^*l^{-1}), A is the absorbance measured at the maximum of the longitudinal LSPR of GNRs, ε is the extinction coefficient calculated (1.15 $M^{-1}cm^{-1}$) and l is the path length (1 cm). The final concentration of the washed GNRs was then calculated as 10 times concentrated respect to the concentration obtained from the Lambert-Beer equation.

Preparation of GNR-NCs

To prepare the GNR-NCs, 1.0 μL of linoleic acid was emulsified in 500μL of arginine-functionalized GNRs (20 μl, 83 nM) in phosphate buffer solution (5.0 mM, pH 7.4) using an amalgamator (speed 5000 rpm for 200s).

This process results oil droplets having 1.58 nM in concentration. Next, 20 μL of the 1.58 nM droplets were incubated with Arg-GNRs (10 μl, 83 nM) in phosphate buffer (5.0 mM, pH 7.4) for 10 min. PTX-loaded GNR-NCs were prepared with the same procedure, dissolving PTX in linoleic acid (10 mg/ml) before preparation. The final concentration of PTX in the GNR-NCs formulation was 23.4 μM.

Calculation for NCs concentration

Concentrations of nanocapsules, both GNR-NCs and crosslinked GNR-NCs were calculated as reported by Rotello et al. [8] by setting the diameter of capsules=144nm (for GNR-NCs) or 159nm (for crosslinked GNR-NCs).

Crosslinking of GNR-NCs

Crosslinking of GNR-NCs was performed as follow:

1) 100 µl of CS_2 were added into 1.5 ml of DCM, then 1.5 mL of NaOH (1M) were added with 1µl of G4 PAMAM dendrimerm (Figure 11) and stirred for two hours;
2) The dendrimer was taken out from the upper fase;
3) GNR-NCs were added to the dendrimer solution from 4) at different dendrimer/ GNR ratio: 0.25, 0.50 and 1.00 and shaked overnight.
4) Finally, crosslinked GNR-NCs were centrifuged for 2 minutes at 2000rpm and resuspended in 10 mM PB.

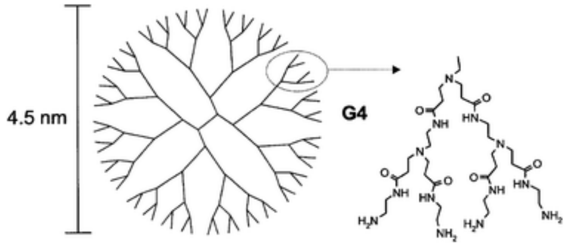

Figure 11. Schematic structure of poly(amido amine) (PAMAM) dendrimer, generation 4 (G4). This dendrimer contains 64 amine surface groups and additional 62 amine groups located inside the dendrimer structure. [29]

UV-vis spectroscopy and DLS measurements

Optical extinction spectra were recorded between 400 nm and 1000 nm with a step of 2 nm, using a Molecular Devices SpectraMax M2 plate reader. DLS was performed on a zeta potential/particle sizer (Malvern Nano ZS90) to determine the distribution of the hydrodynamic diameters of GNR-NCs. Nanocapsules were diluted 10 times in 5 mM PB before measurements.

TEM of GNR-NCs

GNR-NCs were drop casted onto a 200-mesh carbon-coated copper grid and dried for 24h. Then TEM images were acquired on a JEOL 7C operating at 80 keV.

Cell viability (Alamar Blue assay)

Cell Viability (Alamar Blue Assays). [30] HeLa cells were cultured at 37 °C under a humidified atmosphere of 5% CO2. The HeLa cells were grown in a low-glucose Dulbecco's modified Eagle's medium (DMEM, 1.0 g/L glucose) containing 10% fetal bovine serum (FBS) and 1% antibiotic (100 U/mL penicillin and 100 μg/mL streptomycin). The HeLa cells were maintained in the above medium and subcultured once every 4 days. The HeLa cells (6 × 104 cells/well) were seeded in a 24- well plate 24 h prior to delivery. On the next day, the old media was removed and the cells were washed with a phosphate buffer saline (PBS) three times before NPSC delivery. The cell viability was measured using an Alamar Blue assay (Invitrogen, CA).

Uptake of Nile Red loaded GNR-NCs

Nile red was dissolved in linoleic acid at a concentration of 1 mg/ml and then used to make GNR-NCs. HeLa cells were seeded in 24 well plate at a density of 50000cells/well one day prior to the delivery. On the day of the delivery, Hela cells were washed with PBS two times, then 20 ul of nile red loaded nanocapsule was suspended with 480 ul opti-medium, and added into cells followed by 2 hours incubation. So the final concentration of nile red for each well was 25 nM. After 2 hours incubation, cells were gently washed with PBS three times, then imagined under green channel using Olympus IX51 fluorescent microscope.

Acknowledgments

The present work was financially supported by Beneficentia Stiftung (Vaduz, Liechtestein) and the National Institutes of Health (EB014277 and GM077173).

References

[1] L. Brannon-Peppas, J. O. Blanchette, Adv. Drug Deliv. Rev. 64 (2012) 206.
[2] A. Salvati, A. S. Pitek, M. P. Monopoli, K. Prapainop, F. Baldelli Bombelli, D. R. Hristov, P. M. Kelly, C. Åberg, E. Mahon, K. A. Dawson. Nat. Nanotechnol. 8 (2013) 137.
[3] S. M. Moghimi, A. C. Hunter, J. C. Murray, Pharmacol. Rev. 53 (2001) 283.
[4] I. Brigger, C. Dubernet, P. Couvreur, Adv. Drug Deliv. Rev. 54 (2002) 631.

[5] I. H. El-Sayed, X. Huang , M. A. El-Sayed, Cancer lett. 239 (2006) 129.

[6] C.E. Mora-Huertasa, H. Fessia, A. Elaissari, Int. J. Pharm. 385 (2010) 113.

[7] S. Peyratout, L. D_hne, Angew. Chem. Int. Ed. 116 (2004) 3850.

[8] X.-C. Yang, B. Samanta, S. S. Agasti, Y. Jeong, Z.-J. Zhu, S. Rana, O. R. Miranda, V. M. Rotello, Angew. Chem. Int. Ed. 50 (2011) 477.

[9] R. Tang, C. S. Kim, D. J. Solfiell, S. Rana, R. Mout, E. M. Velazquez-Delgado, A. Chompoosor, Y. Jeong, B. Yan, Z.-J. Zhu, C. Kim, J. A. Hardy, V. M. Rotello, ACS Nano 7 (2013) 6667.

[10] C. S. Kim, R. Mout, Y. Zhao, Y.-C. Yeh, R. Tang, Y. Jeong, B. Duncan, J. A. Hardy, V. M. Rotello, Bioconjugate Chem. 26 (2015) 960.

[11] M.-H. Park, S. S. Agasti, B. Creran, C. Kim, V. M. Rotello. Adv. Mat. 23 (2011) 2839.

[12] M.-H. Park, S. T. Kim, S. Rana, D. Solfiell, Y. Jeong, B. Duncan, B. Yan, B. Aksoy, V. M. Rotello. Nanoscale 5 (2013) 7808.

[13] C.J. Murphy, C.J. Orendorff, Adv. Mater. 17 (2005) 2173.

[14] W. Choi, J.-Y. Kim, C. Kang, C. C. Byeon, Y. H. Kim, G. Tae, ACS Nano 5 (2011)1995.

[15] E.B. Dickerson, E.C. Dreaden, X. Huang, I.H. El-Sayed, H. Chu, S. Pushpanketh, J.F. McDonald, M.A. El-Sayed, Cancer Lett. 269 (2008) 57.

[16] B. Nikoobakht, M.A. El-Sayed, Chem. Mater. 15 (2003) 1957.

[17] F. Scaletti, C. S. Kim, L. Messori, V. M. Rotello, MethodsX 1 (2014) 118.

[18] M.-H. Park, S. S. Agasti, B. Creran, C. Kim, V. M. Rotello, Adv. Mater. 23 (2011) 2839.

[19] C. Kinnear, H. Dietsch, M. J. D. Clift, C. Endes, B. Rothen-Rutishauser, A. Petri-Fink, Angew. Chem. Int. Ed. 52 (2013) 1934.

[20] M. A. Garcia, J. Phys D: App. Phys. 44 (2011) 283001.

[21] B. Yan, Z.-J. Zhu, O. R. Miranda, A. Chompoosor, V. M. Rotello, Anal. Bioanal. Chem. 396 (2010) 1025.

[22] J. C. Irvine, R. H. Ritchie, J. L. Favaloro, K. L. Andrews, R. E. Widdop, B. K. Kemp-Harper, Trends Pharmacol. Sci. 29 (2008) 601.

[23] A. T. Wright, M. J. Griffin, Z. L. Zhong, S. C. McCleskey, E. V. Anslyn, J. T. McDevitt, Angew. Chem. 117 (2005) 6533.

[24] A. Buryak, K. Severin, J. Am. Chem. Soc. 127 (2005) 3700.

[25] M. A. Garcia, J. Phys D: App. Phys. 44 (2011) 283001.

[26] E. Prodan, C. Radloff, N. J. Halas, P. Nordlander, Science 302 (2003) 419.

[27] M.-H. Park, Y. Ofir, B. Samanta, V. M. Rotello, Adv. Mater. 21 (2009) 2323.

[28] C. Kinnear, H. Dietsch, M. J. D. Clift, C. Endes, B. Rothen Rutishauser, and A. Petri-Fink, Angew. Chem. Int. Ed. 52 (2013) 1934-1938.

[29] C. S. Kim, R. Mout, Y. Zhao, Y.-C. Yeh, R. Tang, Y. Jeong, B. Duncan, J. A. Hardy, V. M. Rotello, Bioconjug. Chem. 26 (2015) 950-954.

[30] D. I. Roncaglia, J. Carballido-Landeira, P. Munuzuri, Phys. Chem. Chem. Phys. 13 (2011) 7426.

Summary

Engineering Gold Nanorods for Cancer Treatment: Biological Profile, Protein Interactions and Drug Delivery.

Summary – Engineering Gold Nanorods for Cancer Treatment: Biological Profile, Protein Interactions and Drug Delivery.

In the present PhD thesis, several issues connected to the synthesis and purification of GNRs, as well as to their use have been addressed, with special attention for biomedical applications such as protein sensing, the photothermal treatment of cancer, and the realization of nanocapsules for the delivery of anticancer drugs.

In **Chapter 1** a method to synthesize GNRs with a size smaller than those obtained with the seeded-growth method is illustrated. This novel method consists of an in-situ oxidation of GNRs directly during the synthesis through pretreatment of the glass bottle used for the synthesis with *aqua regia*. During the pretreatment the surface of the glass container is saturated with NOCl generated from *aqua regia*. Thereafter, the NOCl release from the glass surface promote the oxidation and shortening of GNRs. It is also demonstrated that the release-mediated oxidation of GNRs can be interrupted simply removing the solution from the treated glass container, allowing a good control of the AR and the LSPR of GNRs. Moreover, contrary to other methods, the present synthesis can be scaled up and considerable amount of GNRs can be synthesized. In a future work this system could be engineered for the production of GNRs in continuos through the use of a reservoir of GNRs and pumping nanorods in a treated glass tube. Therefore, the control of GNRs flow into the glass tube could provide GNRs with different ARs in a large scale.

Chapter 2 accurately described a modified method for the purification of small GNRs from reaction by-products (i.e. spherical and cubic nanoparticles or aggregates). Contrary to other methods, the presented one does not require the addition of surfactant or salts and large amount of GNRs can be easily separated from by-products with a high yield simply by a two-step centrfugation.

Chapter 3 concluded that PEGylated GNRs constitute a stable platform for biomedical applications. Their shape governs the frequency of their plasmonic resonances, while their size can be engineered to optimize the interface with an optical excitation and a biological environment for specific uses. The relationship between particle size and some biological profiles has been assessed in this chapter, showing that modest PEG-GNRs cytotoxicity appears only at high concentrations and after long incubation time, with little variations respect to particles size. However some differences may arise from the larger specific surface area of smaller particles, which have been associated with some contamination originating from the particle synthesis. Acute effects, such as membrane permeabilization and haemolysis, were not observed for any particle size. Future efforts should focus on the removal of contaminants from PEG-GNRs without destabilizing the PEG coating. The cellular uptake of PEG-GNRs is low and displays some modulation with particle size: larger particles may be convenient for those contexts that require unspecific uptake, such as for loading of cellular vehicles, while average particles may be ideal to inhibit unspecific uptake and pursue slower blood clearance or specificity by the addition of ligands. All this evidence, together with the absence of interactions with some representative proteins, suggested that PEG-GNRs are compatible with blood injection. In essence, particle size does not overturn the safety and blood compatibility of PEGylated GNRs in their range of greatest biomedical interest, but may still provide alternatives for a fine modulation of functional biological profiles.

In **Chapter 4**, the effect of the insertion of charged groups in PEGylated GNRs on proteins interaction is reported, by monitoring the LSPR of GNRs, which is highly sensitive to changes in the refractive index. A comprehensive view of the reported results demonstrated quite unambiguously that the interactions between differently functionalized GNRs and a few representative proteins are mainly determined by the electrostatic properties of the interacting moieties and, in addition, by the presence of electrolytes in solution. These interactions were analyzed in the case of three proteins: hCC, HEWL, and BSA. The interactions between the three proteins and the two kinds of functionalized GNRs appeared exemplary and clearly supported the Coulombic nature of the interaction. The case of the BSA/GNR-PEG-NH_2 complexes is the most relevant one, which can be schematically depicted as protein adsorption on functionalized GNRs followed by partial unfolding. Moreover, the strong influence of electrolytes on the interaction between proteins and functionalized GNRs offers strong evidence for the importance of the role of electrostatics in these interactions.

In conclusion, this chapter provides demonstrations that the type of functionalization can direct quite selectively proteins binding to GNRs, leading to different interaction patters and providing useful hints for protein sensing applications. Future work will be focused on the use of this method for sensing on a solid substrate through immobilization of functionalized GNRs on a surface.

Finally, **Chapter 5** reported the integration of the controlled release properties of the GNP-NCs systems with the NIR capabilities of GNRs, which could provide drug delivery systems with highly spatiotemporal therapeutic action. Therefore, the strategy to develope GNP-NCs has been adapted to produce GNR-stabilized NCs with a size suitable to take advantage of the EPR effect. GNR-NCs have also been crosslinked with G4 PAMAM dendrimer to provide NCs that are stable in physiological conditions. Moreover, crosslinked GNR-NCs have been designed to be safe platforms for delivery and to promote the PTX release upon laser activation. In fact, nanocapsules did not show potential nonspecific NCs cytotoxicity on HeLa cells, while PTX-loaded crosslinked nanocapsules showed a different cytotoxicity profile compared to PTX-loaded GNR-NCs, suggesting that crosslinking may inhibit PTX release. Further studies will be performed to characterize the potential PTX photorelease in solution and the in vitro effectiveness of the photorelease against HeLa cells. These GNR-stabilized nanocapsules could provide highly localized release of anticancer therapeutics, laying the basis for future pre-clinical animal studies that could lead to an important new therapeutic strategy for tumors.

Acknowledgments

Acknowledgments

Thank you all.